Multiple-Mode Resonator Analysis and Its Applications to Microwave Waveguide Components

by Jingyu Lin

Thesis submitted in fulfilment of the requirements for the degree of Doctor of Philosophy

under the supervision of
Principal Supervisor: Dr Yang Yang
Co-Supervisor: Dr Forest Zhu

University of Technology Sydney
Faculty of Engineering and Information Technology

December 2022

CERTIFICATE OF ORIGINAL AUTHORSHIP

I, Jingyu Lin, declare that this thesis is submitted in fulfilment of the requirements award of the Doctoral Degree, in the School of Electrical and Data Engineering, Faculty of Engineering and Information Technology at the University of Technology Sydney.

This thesis is wholly my own work unless otherwise referenced or acknowledged. In addition, I certify that all information sources and literature used are indicated in the thesis.

I certify that the work in this thesis has not previously been submitted for a degree nor has it been submitted as part of the requirements for a degree at any other academic institution except as fully acknowledged within the text.

This research is supported by the Australian Government Research Training Program.

Production Note:

Signature: Signature removed prior to publication.

Date: December 12, 2022

Acknowledgement

Time flies so quickly. I was a visiting student when I first came to UTS, and now I'm about to graduate with a PhD. Everything is as good as ever, I learned a lot, met a lot of great people, gained a lot of knowledge, and I really appreciate the time I spent here.

First of all, I would like to give my heartfelt thanks to my principal supervisor Dr. Yang Yang, whose advice and encouragement gave me a better understanding of my research topic. It is a great honor and joy to study under his guidance and supervision. Furthermore, I am honored to benefit from his personality and hard work, which I will treasure my whole life.

I would also like to express my gratitude to my co-supervisor Dr. Forest Zhu. His views on on-chip circuits have inspired me a lot in my millimeter-wave and terahertz research. I am also very grateful to Dr. He Zhu and Dr. Ting Zhang for their insights into my waveguide research. I also deeply appreciate all the other mentors and teachers for their direct and indirect assistance.

I would like to thank Prof. Sai-Wai Wong from Shenzhen University, who led me into the world of academic research. His attitude towards academic research left a deep impression on me, which will prove to be beneficial to my academic career.

Lastly, my thanks are extended to my beloved parents for their unfailing love and unwavering support. I also owe my sincere gratitude to my friends and my fellow classmates who helped me solve problems. My heart swells with gratitude to everyone who has helped me.

Published and Under Review Papers Related to This Thesis

[a1] **J.-Y. Lin**, Y. Yang, S.-W. Wong, R.-S. Chen, Y. Li, L. Zhang, Y. He, and L. Zhu, "Cavity Filtering Magic-T and Its Integrations Into Balanced-to-Unbalanced Power Divider and Duplexing Power Divider," ***IEEE Transactions on Microwave Theory and Techniques***, vol. 67, no. 12, pp. 4995-5004, Dec. 2019. **[Chapter 2]**

[a2] S.-W. Wong, **J.-Y. Lin**, Y. Yang, Z.-C. Guo, L. Zhu and Q.-X. Chu, "Waveguide Components Based on Multiple-Mode Resonators: Advances in Microwave Multiple-Mode Waveguide Components, Including Multiplexers, Three-State Diplexers, Crossovers, and Balanced/Unbalanced Elements," ***IEEE Microwave Magazine***, vol. 22, no. 2, pp. 33-45, Feb. 2021. **[Chapter 1 and 2]**

[a3] **J.-Y. Lin**, Y. Yang, S.-W. Wong and Y. Li, "High-Order Modes Analysis and Its Applications to Dual-Band Dual-Polarized Filtering Cavity Slot Arrays," ***IEEE Transactions on Microwave Theory and Techniques***, vol. 69, no. 6, pp. 3084-3092, June 2021. **[Chapter 3]**

[a4] **J.-Y. Lin**, S.-W. Wong and Y. Yang, "Filtering In-Band Full-Duplex Slot Antenna Based on TM120 and TM210 Dual-Mode Resonators," ***2021 IEEE MTT-S International Microwave Filter Workshop (IMFW)***, 2021. **[Chapter 4]**

[a5] **J.-Y. Lin**, Y. Yang, S.-W. Wong, and R.-S. Chen, “In-Band Full-Duplex Filtering Antenna Arrays Using High-Order Mode Cavity Resonators,” ***IEEE Transactions on Microwave Theory and Techniques***. **[Chapter 4]**

[a6] **J.-Y. Lin**, Y. Yang and S.-W. Wong, "Four-Way Filtering Crossover Based on Quadruple-Mode Cavity Resonator," ***2021 IEEE MTT-S International Microwave Symposium (IMS)***, 2021. **[Chapter 5]**

[a7] **J.-Y. Lin**, Y. Yang, S.-W. Wong, X. Li, L. Wang, and E. Dutkiewicz, “Two-Way

Waveguide Diplexer and Its Application to Diplexing In-Band Full-Duplex Antenna," ***IEEE Transactions on Microwave Theory and Techniques***. **[Chapter 5]**

[a8] **J.-Y. Lin**, Y. Yang, T. Zhang, S.-W. Wong and J. Du, "Inline Waveguide Bandpass Filter Using Bandstop Resonator Pairs," submitted to ***2023IEEE MTT-S International Microwave Symposium (IMS)***. **[Chapter 6]**

Abstract

Composite signals can be represented as a combination of multiple sinusoidal signals with varying frequencies, phases, and amplitudes. In general, these critical features can be manipulated by microwave components for different applications. As the indispensable part of most microwave components, microwave resonators play a significant role in functional circuit designs. Single resonance (single mode) circuit in one order or higher orders have dominated industry's usage of microwave circuits and systems. For high-power applications such as base stations, satellite communication, and aerospace communication, conventional SMR waveguide components have the advantage of achieving high performance and meeting required precision performance specifications. However, their bulky circuit volume and high fabrication cost hinder their implementation in many space-constrained scenarios. There is a need to tackle these challenges by means of a novel approach. MMRs, with more than one resonant mode in a single resonator, have been investigated by several research groups over the last decade. Compared to SMR, besides the merits of circuit miniaturization, low-loss, and low-cost, MMR has an inherent advantage of diverse topologies with better out-of-band signal attenuation, due to the generation of additional transmission zeroes (TZs). In addition, MMR provides more design freedom and flexibility in function integration, which might not be possible using single mode resonators. The main contents are as follows:

1. Cavity filtering magic-T and its integrations into balanced-to-unbalanced (B2U) power divider (PD) and diplexing power divider.
2. Single-band and dual-band filtering antenna arrays (FAAs) based on high-order mode resonators.
3. In-band full-duplex (IBFD) filtering antenna arrays based on high-order mode resonators for narrowband and wideband applications.
4. Two-way waveguide diplexer and its application to diplexing IBFD antenna using quadruple-mode resonators.
5. Inline waveguide bandpass filter using bandstop resonator pairs.

Keywords: Waveguide filter, multiple-mode resonator, transmission zero, slot antenna, in-band full-duplex, filtering antenna array, magic-T, balun, high-order mode, multi-mode resonator, millimeter-wave, terahertz.

CONTENTS

Chapter 1 Introduction

1.1 Research Background

Waveguide components have been widely explored for several decades due to their inherent advantages of low insertion loss, high unloaded quality factor (Q_u), and high power handling capacity. Historically, cavity-based narrowband filters and multiplexers have been explored and designed for base stations or satellite applications. Compared with the planar low Q_u resonators lumped elements, microstrip and relative high Q_u coaxial resonators, dielectric resonators, the waveguide takes up the largest Q_u and lowest insertion loss as shown in Fig. 1.1.

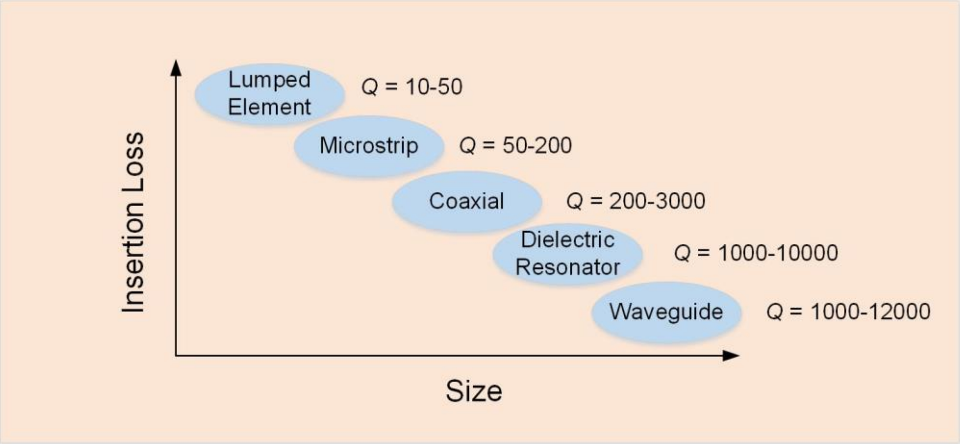

Fig. 1.1. Comparison of Q_u values among different resonators.

There are multiple mode resonators (MMRs) in a single waveguide, including fundamental modes and high-order modes. They possess the characteristics of modal orthogonality among degenerate modes, out-of-phase performance for each mode, and in-phase with the same amplitude for high-order modes. MMR has an inherent advantage of diverse topologies with better out-of-band signal attenuation, due to the generation of additional transmission zeroes (TZs). In addition, MMR provides more design freedom and flexibility in function integration.

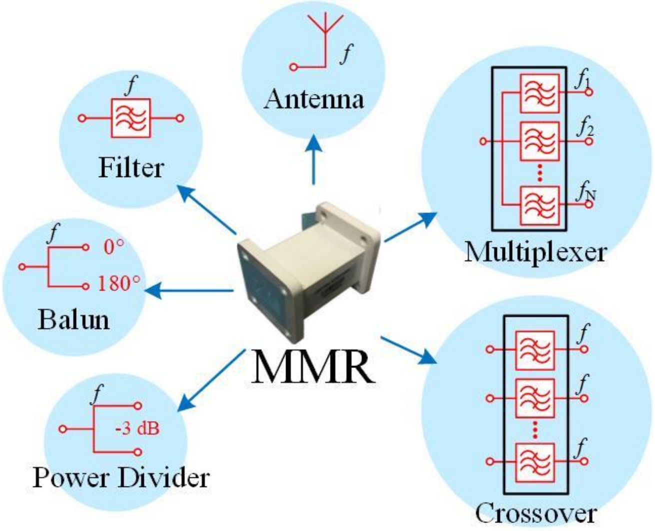

Fig. 1.2. Categories of microwave passive components.

MMR can be used in many microwave component designs [1] as shown in Fig. 1.2. A microwave filter can be achieved by using MMR with improved bandwidth and out-of-band signal suppression. Further expanding this concept, out-of-phase and in-phase performance can be achieved in a three-port network for implementations of baluns and power dividers, respectively, while maintaining the merits of in-band and out-of-band performance. These three components are fundamental ones that focus on the manipulation of a single signal with one operational frequency, *f*. In the case of several signals resonating at different frequencies, multiplexing is a 1-to-N system that separates desired signals from corresponding channels, where the outputs are isolated from each other. Conversely, an N-to-N system can be considered as a combination of multi-channel filters for the reason that the same/different signals from N inputs transmit to their respective outputs. The antenna can be regarded as a one-port system while the electromagnetic waves on the other side are radiated. This thesis aims to investigate the characteristics and potential uses of multiple-mode resonators, and to study the mechanism of highly integrated and multi-functional circuits. The state-of-the-art research will be conducted as follows.

1.2 Literature Review

1.2.1 Waveguide MMR-Based Filters

1.2.1.1 Narrow-Band Filters

Filters are primarily used in microwave components, which can be generally categorized as: narrow-band filters, wide-band filters, and multiple-band filters. Due to the high Q_u of cavity resonators, cavity-based narrow-band filters have long been investigated. In this section, we introduce narrowband filters based on different MMRs differentiated by the number of intrinsic operating modes: 1) dual-mode resonators, 2) triple-mode resonators, and 3) quadruple-mode resonators.

Typically, there are two types of modes used in dual-mode resonators: 1) TM_{120}/TM_{210} harmonic modes [2]-[5], 2) TE_{011}/TE_{101} fundamental modes [6]-[8].

First we discuss TM_{120}/TM_{210} modes. Fig. 1.3(a) presents a 6th-order filter topology based on three TM_{120}/TM_{210} doublets connected by non-resonating nodes (NRNs), while a photograph of the proposed filter is shown in Fig. 1.3(a). As explained in [2], each of this type of doublet can generate two transmission zeros (TZs) at maximum. Fig. 1.3(b) illustrates that the filter passband is centered at 10 GHz with a fractional bandwidth of 1.5% and measured insertion loss of 0.6 dB. A maximum of six TZs are generated and located beside the passband to increase the filter's high selectivity.

In [3], instead of using doublet topology, this pair of TM_{120}/TM_{210} modes are arranged by a direct-coupling topology to form an 8th-order filter with eight TZs symmetrically located at the lower and upper stopbands. In [4], a dielectric resonator (DR) is installed within the cavity to further decrease the structure volume; thus an 8th-order symmetric filter composed of four DRs is designed at 1.95 GHz with bandwidth of 67 MHz and measured insertion loss of 0.5 dB.

Here we discuss the use of TE_{011}/TE_{101} modes. In [6], tuning screws are inserted the cavity resonator to excite the proposed dual modes simultaneously. While in [8],

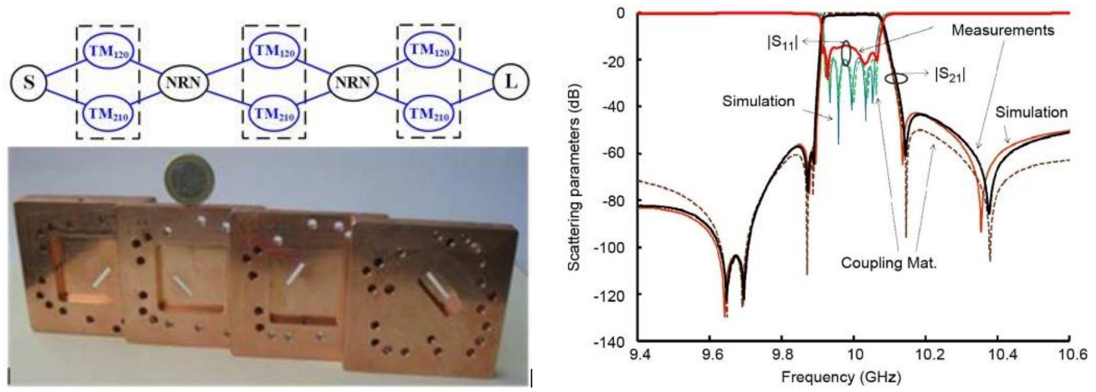

(a) (b)

Fig. 1.3. TM dual-mode 6th-order filter with: (a) doublet topology connected by NRN and photograph using three cavity resonators. (b) Comparison between simulated and measured results [2].

without any additional elements installed in the cavity, a pair of cross-rotated slots are placed at the surface center of the cavity resonator, to excite the TE_{011}/TE_{101} doublet with the generation of one TZ. This TZ can be placed at the lower or upper stopband depending on the rotated angle of the slots.

Another type of structural topology, namely a TE_{011}/TE_{101}/TM_{110} triplet, is depicted in the inset of Fig. 1.4(a). It can be seen that three fundamental modes are located in parallel and coupled with source and load, respectively. The narrowband filter designs based on triple-mode resonators can be found in [7]-[15].

According to this topology, a geometrical configuration of the designed triple-mode filter is proposed in Fig. 1.4(a) and explained in [8]-[9]. Three fundamental modes in this cavity resonator can be excited simultaneously by virtue of a pair of rotated and offset slots. Fig. 1.4(b) depicts the implementation of a third-order frequency response with one TZ on the left and the other one on the right-hand side of the passband. This filter resonates at 2.99 GHz with the fractional bandwidth of 1% and measured insertion loss of 0.5 dB. The out-of-band attenuation at both sides of the desired passband gets sharp skirt and achieves an attenuation level that is better than 30 dB.

Another approach to realizing good narrowband is to install a dielectric resonator

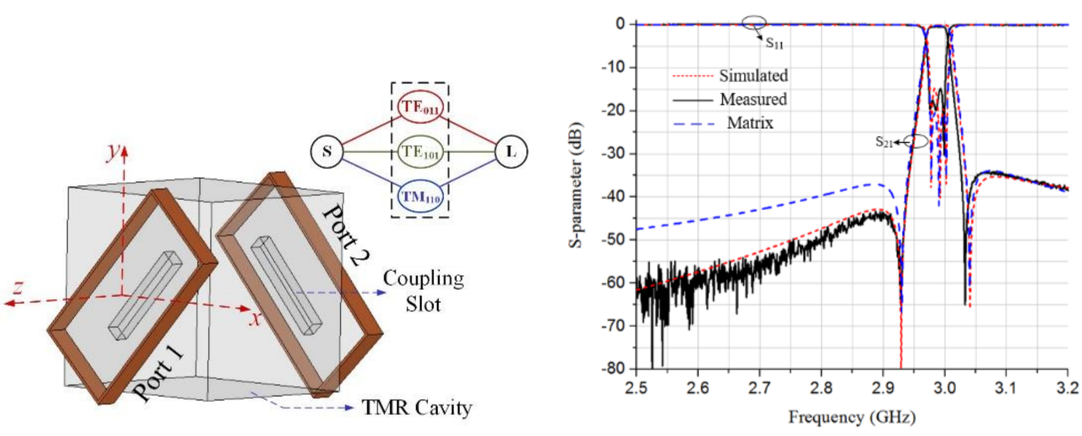

(a) (b)

Fig. 1.4. Triple-mode filter with: (a) Geometrical configuration using one triple-mode resonator. (c) Comparison between simulated and measured results [9].

(DR) in the metal cavity [10]. The proposed filter resonates at a center frequency of 2.53 GHz with a fractional bandwidth of 2.7% and a measured insertion loss of 0.4 dB.

Furthermore, in [14], this triplet topology is extended and enriched by adding four more resonators, to achieve a 7th-order narrow-band filter. Based on a slab-slab-cube-slab-slab structure, the silver-plated ceramic cavity filter achieves 1 dB of band-edge insertion loss with fractional bandwidth of 4% and more than 50 dB of attenuation.

Several researchers have investigated in detail quadruple-mode resonators [16]-[19]. In [16], as presented in the inset of Fig. 1.5(a), a quadruplet is shown that combines two doublets: a TE_{011}/TE_{101} doublet and a TM_{120}/TE_{210} doublet. Therefore, two TZs are generated and controlled independently. The geometrical configuration is depicted in Fig. 1.5(a); a pair of cross-rotated slots are placed at the left-hand and right-hand side of the cavity resonator. By properly arranging the resonant frequencies of four modes within a frequency range, a 4th-order response forms up with one TZ at the lower stopband and one TZ at the upper stopband, as shown in Fig. 1.5(b).

In [17], the proposed quadruple-mode resonator is made up of four inner metal posts within a single cavity, which improves the unloaded Q values. Furthermore, four TZs are generated due to multiple cross-coupling and source-to-load direct coupling.

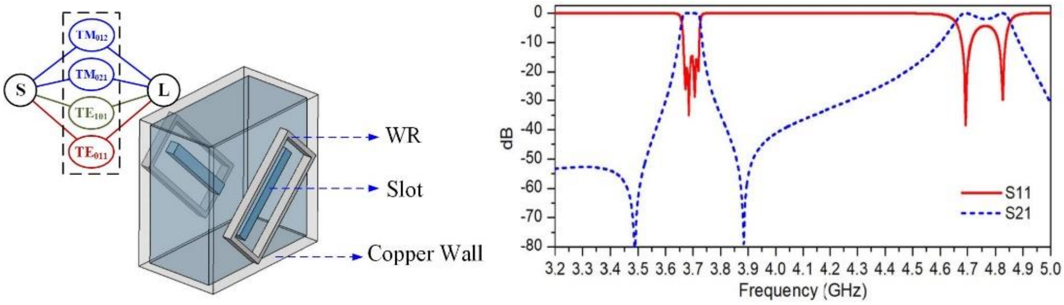

(a) (b)

Fig. 1.5. Quadruple-mode filter with: (a) Geometrical configuration using one quadruple-mode resonator, (b) simulated results [16].

Based on this summary of different types of MMRs, it can be seen that use of more modes in a single cavity has the obvious advantages of better miniaturization. However, design sensitivity is also increased since more parameters are required to control the relevant internal and external couplings.

1.2.1.2 Wide-Band Filters

Decreasing the external quality factor Q_e of a cavity resonator is the key to designing a wideband cavity filter with a fractional bandwidth that is more than 20%, which is still a challenging research topic. A novel wideband bandpass filter using simple perturbation in a single metal cavity is presented in Fig. 1.6(a) and explained in [20]. A perturbation metal cylinder is fixed at the bottom of the intra-cavity with off-centered position. The extracted Q_e of three resonant modes in the cavity are 5.13, 11.60, and 26.88, respectively, which satisfy the requirements of wideband filter designs. Fig. 1.6(b) depicts the simulated and measured results showing that this kind of filter resonates at a center frequency of 3.2 GHz with a fractional bandwidth of 30% and measured insertion loss of 0.5 dB. The group delay within the passband varies within 0.6 ns, demonstrating good linearity.

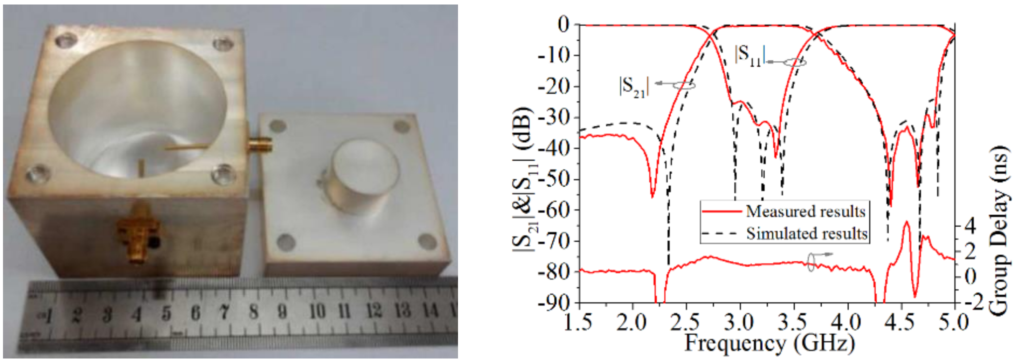

(a) (b)

Fig. 1.6. (a) Photograph of the wideband filter using one metal perturbation. (b) Comparison between simulated and measured results [20].

Furthermore, one and two more perturbation metal rods [21] are installed at the bottom of the intra-cavity. Therefore, besides three fundamental modes, one and two more modes are excited and resonated at the central frequencies, so that the bandwidth of the filter can be further enlarged.

We next focus on the relationships between fundamental modes and their harmonic modes. In [22], center conductors of the two coaxial feed lines are perpendicular to the bottom sidewall of the cavity. They are extended into the cavity as coupling probes for exciting three TM resonant modes, namely, TM_{110}, TM_{210}, and TM_{310}. Compared with wideband filters using three fundamental modes, the proposed filter achieves wider bandwidth, showing the fractional bandwidth of 58% at the center frequency of 5.5 GHz with about 0.5 dB measured insertion loss.

1.2.1.3 Multiple-Band Filters

In the state-of-the-art, multiple-band waveguide filters based on MMRs can be classified into two categories: dual-band filters [24]-[27] and triple-band filters [9], [28]-[30].

Generally, two bands of the designed dual-band filter are separately and independently dominated by two resonant modes of the cavity resonators. Both modes are excited at the first order and separated at the last order, which can dramatically

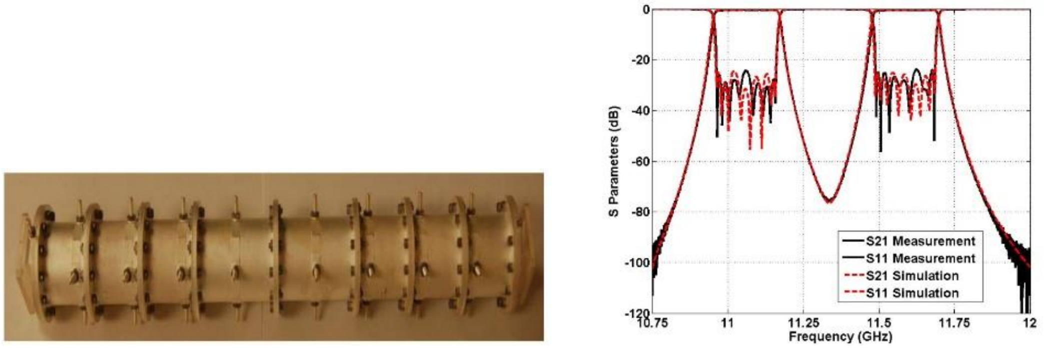

(a) (b)

Fig. 1.7. (a) Photograph of the fabricated dual-band 8th-order filter. (b) Comparison between simulated and measured results [27].

decrease the circuit volume. In [27], the structure of the eighth-order dual-band filter comprises six TE_{112} modes and two TE_{113} modes. Elliptical cavities are designed to meet the requirement of Q_u and the spurious-free window. The filter was manufactured from invar alloy with silver plating and is depicted in Fig. 1.7(a). The ratio of the horizontal and vertical axis length of the elliptical cavity is around 1.15. An average value of Q_u of 18000 and a spurious-free window from 10 to 12.5 GHz is achieved. The measured return loss is better than 24 dB, and the insertion loss is 0.38 dB, as is shown in Fig. 1.7(b).

In [24], two fundamental modes, TE_{011} and TE_{101}, are used to independently control each band of a dual-band filter. In [26], to achieve widely separated passbands, one fundamental mode and its first-order harmonic mode are used; the frequency ratio in this design can reach 1.5.

Three fundamental modes, TE_{011}, TE_{101}, and TM_{110}, are adopted to independently control each of the three bands of a triple-band filter. In [30], an elliptical-cavity triple-band filter with 3rd-order response is designed with an in-line configuration shown in Fig. 1.8(a). Three sub-bands are set at the lower band: 3.6–3.9 GHz, middle band: 3.9–4.1 GHz, and higher band: 4.1–4.4 GHz, respectively. The measured return loss is better than 20 dB, and the rejection between adjacent channels is more than 50 dB. The measured insertion loss is 0.22–0.25 dB.

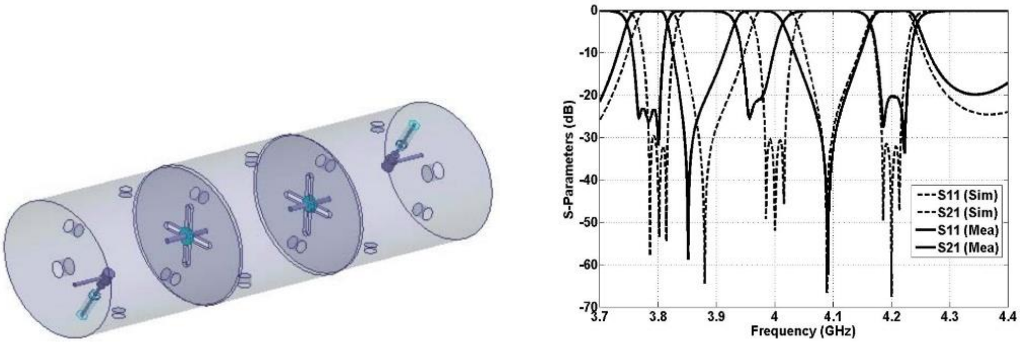

(a) (b)

Fig. 1.8. (a) Geometrical configuration of the triple-band 3rd-order filter. (b) Comparison between simulated and measured results [30].

In [29], a 4th-order C-band triple-band filter is manufactured at the center frequencies of 3.6, 3.8, and 4.0 GHz, respectively, where the absolute bandwidths are all 20 MHz. The measured insertion losses, ranging from 0.38 to 0.46 dB, reflect a loaded *Q* in the 7800 to 8500 range.

1.2.2 Waveguide MMR-Based Multiplexers

MMR inspired multiplexers can be categorized into four types: 1) diplexer, 2) triplexer, 3) multiplexer, and 4) three-state diplexer.

1.2.2.1 Diplexers

According to conventional diplexer design, the first step is to implement two bandpass filters (BPFs), one at the lower band and the other at the upper band. Therefore, BPFs play a key role in determining the performance of a diplexer using traditional design methods. Herein, we present a variety of diplexers [31]-[34] based on MMR BPFs.

Fig. 1.9(a) presents the internal view of a manufactured diplexer which is explained in [31]. The diplexer has been confirmed as operating in two prescribed bands with the central frequencies of 2.55 and 2.66 GHz, and each passband has an absolute

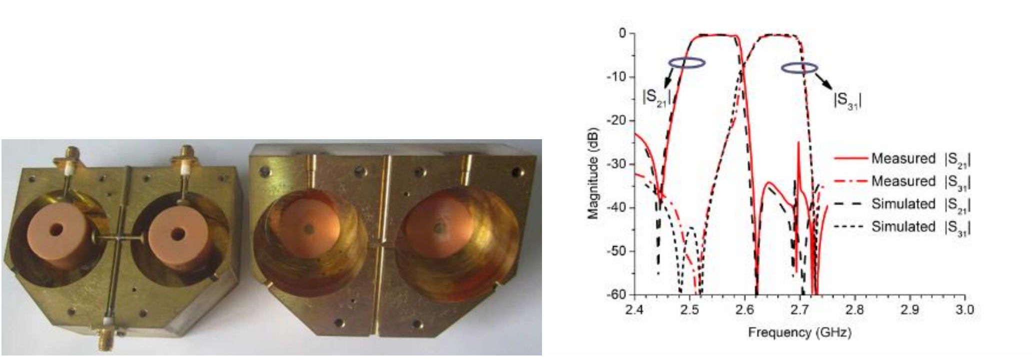

(a) (b)

Fig. 1.9. (a) Photograph of the narrow-band DR-based diplexer. (b) Comparison between simulated and measured results [31].

bandwidth of about 80 MHz. Three TZs are located at the lower and upper stopbands to achieve a sharp roll-off rate. The measured minimum insertion losses are 0.63 and 1.10 dB in the two passbands, respectively. The output isolation ($|S_{32}|$) is also measured, which is better than 18 dB from 2.4 to 2.7 GHz.

1.2.2.2 Triplexers

In this section, a triplexer is investigated and designed using the triple-mode approach. The presented topology is depicted in the inset of Fig. 1.10(a), and three fundamental modes in a TMR are simultaneously excited at port 1. Due to modal orthogonality, they can be propagated into their respective loads, which act as the outputs of the proposed triplexer. In addition, each channel dominated by these modes of the triplexer will be isolated from each other. Based on this, a geometrical configuration with 2nd-order filtering response is presented in Fig. 1.10(a) and fully explained in [35]. Fig. 1.10(b) illustrates the simulated and measured results of the proposed triplexer. Three passbands operate at the central frequencies of 2.87, 3.06, and 3.23 GHz, with 3-dB bandwidths of 15 MHz, 11 MHz, and 9.5 MHz, respectively. The measured insertion losses in these three passbands are equal to 0.6 dB, 1.0 dB, and 1.0 dB, respectively, while the isolation among these three bands is better than 20

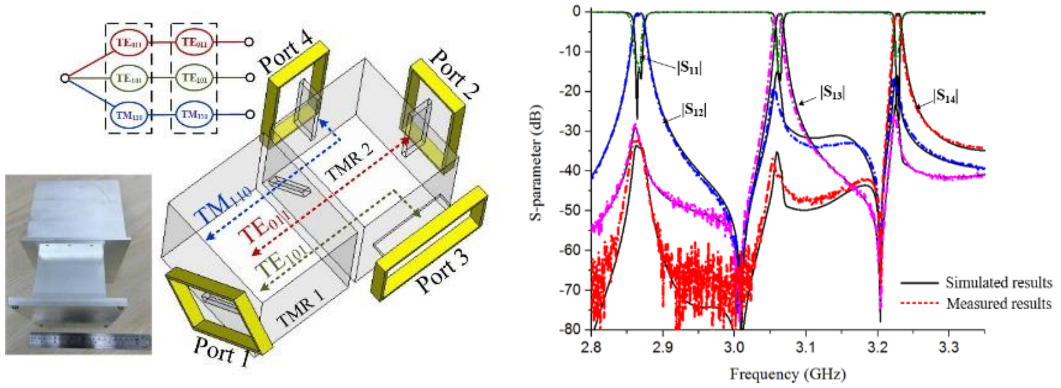

(a) (b)

Fig. 1.10. Triplexer based on triple-mode resonators with: (a) geometrical configuration with 2nd-order response, (b) comparison between simulated and measured results [35].

dB.

Furthermore, as presented in [35], the port-to-port isolation of a triplexer can be further improved by adding more resonators. A geometrical configuration of a triplexer with one TMR and three SMRs is proposed to implement the 2nd-order response triplexer, and three fundamental modes are separated in the first order. The presented triplexer design approach has the advantage of requiring fewer resonators and omitting the occupation of channel division junctions.

1.2.2.3 Multiplexers

Research by the authors of [36]-[38] shows that a multiplexer can be composed of MMRs and a manifold matching junction, as shown in Fig. 1.11(a). Due to the high selectivity and sharp out-of-band rejection of the filter components, they can be placed close to each other to prevent waste of frequency resources. A broadband waveguide contiguous output multiplexer (OMUX) is presented in [37]; two utilized dual-mode resonators are coupled inline to form a 4th-order filter with two TZs. The proposed filters also possess at least 30% more spurious-free range in both the Ku-band and the C-band, which ensures enough frequency space for multiplexer design. A

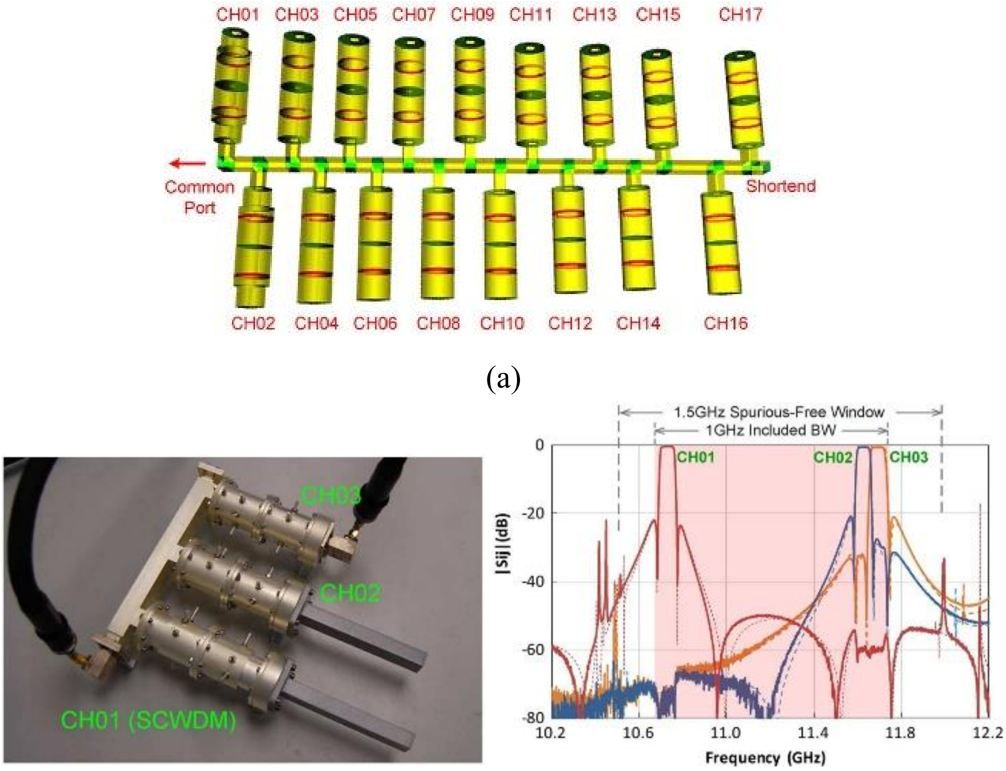

(a)

(b)

(c)

Fig. 1.11. (a) Illustrated topology of 17-channel multiplexer. (b) Photograph of fabricated 3-channel multiplexer based on dual-mode resonators, (c) Comparison between results [37].

manufactured 3-channel multiplexer is shown in Fig. 1.11(b); measured results show excellent agreement with the theoretical EM designs, as plotted in Fig. 1.11(c).

In [38], a dual-mode super Q resonator is utilized to implement the filter and multiplexer design. A 20-GHz two-channel ($Q > 25000$) vertical multiplexer with 32-MHz channel bandwidth is fabricated and tested.

1.2.2.4 Three-State Diplexers

A new concept and approach for the integration of a three-state cavity diplexer is presented in [39]. The functions of a three-state diplexer can be summarized as:

State I: Excitation of port 1 corresponds to the generation of channels f_1 and f_2.

State II: Excitation of port 2 corresponds to the generation of channels f_1 and f_3.

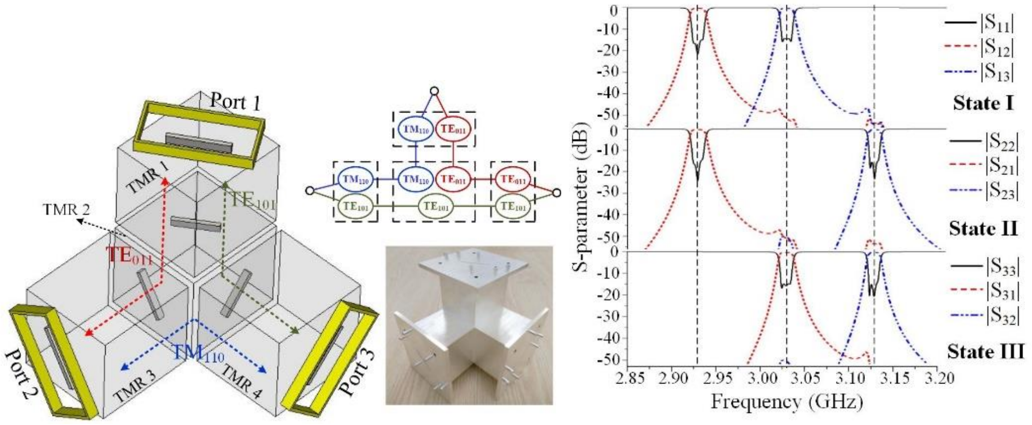

(a) (b)

Fig. 1.12. Three-state diplexer based on triple-mode resonators with: (a) geometrical configuration with 3rd-order response, (b) Separated S-parameter responses [39].

State III: Excitation of port 3 corresponds to the generation of channels f_2 and f_3.

Fig. 1.12(a) shows the geometrical configuration of a three-state diplexer with a 3rd-order response which consists of four identical TMRs. For all three states, all the excited modes propagate through the TMR 2 cavity into the corresponding output ports. Three fundamental modes can be propagated through three of four TMRs simultaneously to form a miniaturized 3rd-order three-state diplexer structure. Fig. 1.12(b) shows the separated simulated three-state S-parameters of the three diplexers in the three-state diplexer. All three passbands are designed with absolute bandwidths of 20 MHz, and isolation between the three channels can be implemented under 27 dB.

In order to achieve higher isolation among the channels of the three-state diplexer presented in [39], a geometrical configuration with 3rd-order response comprising six TMR cavities is proposed. Unlike the TMR 2 in Fig. 1.12(b) as a shared TMR for three fundamental modes, in the proposed structure, each of the three modes has its own path to be propagated. Compared with the former case using four TMRs, the latter has a better isolation among all the channels, but increases the resonator amounts and circuit volume.

1.2.3 Crossovers and Balun Circuits

1.2.3.1 Crossovers

It is crucial to prevent interaction among multiple channel integrations in an N-to-N system. Modal orthogonality among multiple modes can address this issue.

In [40], two types of three-way crossovers are presented for different applications. Depicted in Fig. 1.13(a), a geometrical configuration of a wide-band crossover with 5th-order response is presented. It is noteworthy that two slots between ports and cavities, and one slot between cavity and cavity, are considered as three resonant windows. Hence, along with two cavity resonators, the 5th-order filtering response can be achieved with five resonators. The S-parameter curves of the three-way wide-band crossover are demonstrated in Fig. 1.13(b). Three fundamental modes resonate at the same frequencies, and the bandwidth is enhanced to 24%, from 2.66 to 3.38 GHz. A perfect performance of isolation with more than 50 dB is reached.

A narrow-band three-way crossover is also presented in [40]. Using a similar structure but different physical dimensions, this kind of crossover possesses a fractional bandwidth of 1.4% at 2.91 GHz central frequency, and isolation among the three-way crossover can reach 60 dB. Furthermore, this wideband crossover unit can be extended to a 2×2 three-way crossover array.

Refs. [41]-[43] present two-way crossover components. In [41] and [42], a dual-channel dielectric-resonator (DR) crossover is implemented using two pairs of HEH_{11} and HEE_{11} harmonic modes. The proposed crossover resonates at 3.525 GHz with an absolute bandwidth of 19 MHz (0.54%) and insertion loss of 0.32 dB. Furthermore, the integration with a Doherty power amplifier (DPA) into 5G massive MIMO system applications is also designed.

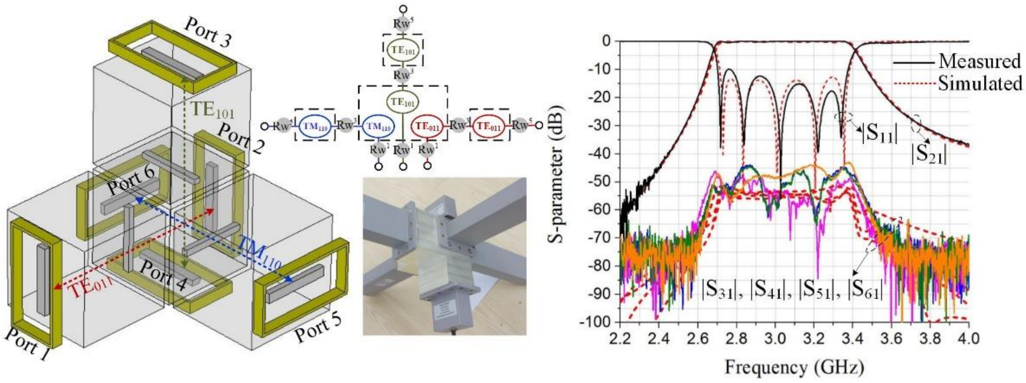

(a) (b)

Fig. 1.13. Three-way crossover based on triple-mode resonators with: (a) geometrical configuration with 5th-order response, (b) comparison between simulated and measured results [40].

1.2.3.2 Balun and Balanced Circuits

A series of cavity-based balun and balanced circuits are designed by means of out-of-phase performance of the resonant modes in [44]-[48].

Refs. [44]-[47] present balun and balanced filter designs that are achieved by properly mounting a DR in the metal cavity. In [47], a balanced filter is designed using a dual-mode cross-shaped DR, which is dominated by a pair of $TE_{11\delta}$ orthogonal modes. The proposed balanced filter resonates at 1.78 GHz with a fractional bandwidth (FBW) of 1.3% and insertion loss of 0.8 dB. Similarly, the proposed balun resonates at 1.78 GHz with FBW of 1.3%. The amplitude imbalance and phase imbalance are within 0.25 dB and 180 ± 1.2º across the passband, respectively.

In [48], a total of four types of balun and balanced diplexers are presented and explained in detail; they utilize the out-of-phase performance of each of three fundamental modes. It is noted that, to achieve balun function simultaneously in both channels of the diplexer, these two modes excited by the balanced input ports should be reversed at the same time. As is depicted in Fig. 1.14(a), a pair of coupling slots form a cross with offsetting along the *y*-axis to excite the out-of-phase TE_{011} and TM_{110} modes, simultaneously. The TM_{110} mode propagates into port 2 while the TE_{011}

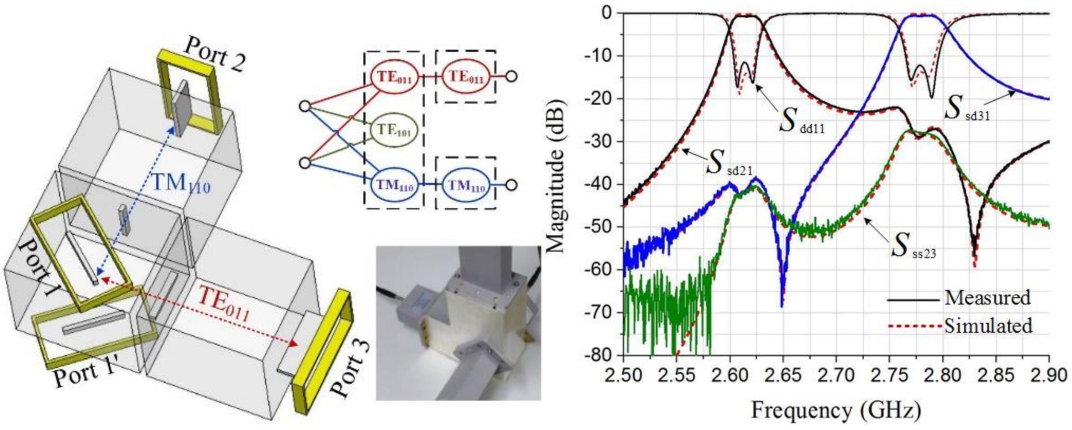

(a) (b)

Fig. 1.14. Balun diplexer based on triple-mode resonators with: (a) geometrical configuration with a 2nd-order topology, (b) mixed-mode S-parameter responses [48].

mode propagates into port 3.

Fig. 1.14(b) depicts the mixed-mode S-parameters of the balun diplexer. It can be seen for the differential-mode response that the TE_{011} mode resonates at 2.61 GHz with a 3-dB bandwidth of 30 MHz, while the TM_{110} mode resonates at 2.78 GHz with a 3-dB bandwidth of 43 MHz. The isolation between port 2 and port 3 is 25 dB from 2.5 to 2.9 GHz.

1.3 Conclusion

In summary, a series of waveguide components based on MMRs are presented and categorized. Compared with the planar structure using PCB technology, waveguide device has its merit in 3-D topology, which has one more direction and can control more resonating modes. Due to the frequency resonances and inherent characteristics of multiple modes in a single cavity, several novel circuits are presented with the advantage of miniaturized circuit volume and low in-band insertion losses. Good matching between simulated and measured results verifies the accuracy of the proposed design methodology. The relationship between different chapters is shown in Fig. 1.2, which contains a variety of different microwave components for various application scenarios.

The thesis is organized as follows:

Chapter 2: Cavity filtering magic-T and its integrations into balanced-to-unbalanced power divider and diplexing power divider. The proposed filtering magic-T is based on three fundamental modes, namely TE_{011}, TE_{101}, and TM_{110}, in a single triple-mode resonator (TMR). In banlanced-to-unbalanced power divider, balanced functions are integrated at input ports. Three fundamental modes provide the odd- and even-symmetric field distributions so that in-phase and out-of-phase responses at output ports can be achieved. In diplexing power divider, isolated ports are applied for magic-Ts to achieve all ports impedance matched and high isolation between channels.

Chapter 3: Single-band and dual-band filtering antenna arrays (FAAs) based on high-order mode resonators. It is found that each unit of filtering antenna array in the proposed high-order mode resonator is in-phase with the same amplitude, which helps to enhance the antenna gain and reduce the side-lobe level. Meanwhile, the filtering function is integrated into the design for frequency selectivity and harmonic mode suppression. A single-band 3rd-order 4×5 filtering antenna array using a TM_{450} mode resonator and a dual-band dual-polarized 3rd-order 4×3 filtering antenna array using TM_{430} and TM_{340} mode resonators are designed, fabricated and tested.

Chapter 4: In-band full-duplex (IBFD) filtering antenna arrays based on high-order mode resonators. The pairs of degenerate high-order modes in a single cavity resonator, TM_{1n0}, and TM_{n10} (n is even), are suitable for IBFD filtering antenna array designs due to their advantages: 1) In-phase and same amplitude for each magnetic loop, which helps to enhance the gain and reduce the sidelobe level; and 2) The modal orthogonality, which guarantees the isolation and cross-polarization level between two channels. A 2nd-order IBFD filtering antenna array with 6×5 elements, using a pair of degenerate modes TM_{610} and TM_{160}, is designed with 1% overlapped 10-dB bandwidth and 18.4 dBi realized gain. Second, a 5th-order IBFD filtering antenna array using TM_{410} and TM_{140} modes is implemented with an overlapped 10-dB bandwidth of 15.6% and a realized gain of 12.5 dBi. The measured isolation between the two channels is better than 40.4 dB.

Chapter 5: Two-way waveguide diplexer and its application to diplexing IBFD antenna. Four waveguide modes, namely TE_{011}, TE_{101}, TM_{210} and TM_{120}, are primarily used. These four modes are modal orthogonal to each other in a single quadruple-mode resonator. Each of the quadruple modes can be independently manipulated with low mutual interference with other modes. Based on the proposed two-way diplexer concept, a diplexing IBFD antenna with a turnstile junction is designed by replacing the inputs with a cross-coupled radiating slot. It integrates the filtering, diplexing, orthomode transducing, and radiating functions into a single element.

Chapter 6: Inline waveguide bandpass filter using bandstop resonator pairs. The synthesis and design of microwave filter is an established art. However, when frequency goes higher, it requires different theory to synthesize and design the filter. This chapter presents the synthesis and design of a well-performed THz filter using proposed multi-mode bandstop resonator, to verify the potential use of MMR in terahertz region. The resonators are implemented by E-plane stubs and resonated at the lower and upper stopbands of the designed BPF, respectively, to provide sharp roll-off and out-of-band rejection. Both stopbands can be controlled independently and cascaded in parallel from source to load without mutual interference. A 5th-order BPF with 11% fractional bandwidth at 250 GHz and five TZs at the lower stopband, five TZs at the upper stopband are constructed, fabricated, and measured.

References

[1] S.-W. Wong, Jing-Yu Lin, Y. Yang, Z.-C. Guo, and L. Zhu, “Microwave waveguide components based on multiple-mode resonators,” *IEEE Microwave Magazine*, 2021.

[2] C. Tomassoni, S. Bastioli and R. Sorrentino, "Generalized TM dual-mode cavity filters," *IEEE Trans. Microw. Theory Techn.*, vol. 59, no. 12, pp. 3338-3346, Dec. 2011.

[3] S. Bastioli, C. Tomassoni and R. Sorrentino, "A new class of waveguide dual-mode filters using TM and nonresonating modes," *IEEE Trans. Microw. Theory*

Techn., vol. 58, no. 12, pp. 3909-3917, Dec. 2010.

[4] H. Hu and K. Wu, "A TM_{11} dual-mode dielectric resonator filter with planar coupling configuration," *IEEE Trans. Microw. Theory Techn.*, vol. 61, no. 1, pp. 131-138, Jan. 2013.

[5] K. Wu, "An optimal circular-waveguide dual-mode filter without tuning screws," *IEEE Trans. Microw. Theory Techn.*, vol. 47, no. 3, pp. 271-276, Mar. 1999.

[6] S. Amari, "Application of representation theory to dual-mode microwave bandpass filters," *IEEE Trans. Microw. Theory Techn.*, vol. 57, no. 2, pp. 430-441, Feb. 2009.

[7] S. Amari and U. Rosenberg, "New in-line dual- and triple-mode cavity filters with nonresonating nodes," *IEEE Trans. Microw. Theory Techn.*, vol. 53, no. 4, pp. 1272-1279, Apr. 2005.

[8] Z.C. Guo, S.W. Wong, J.Y. Lin, L. Zhu, Q.-X. Chu, Q. Zhang, and Y. Yang, "Triple-mode cavity bandpass filter on doublet with controllable transmission zeros," *IEEE Access*, vol. 5, pp. 6969-6977, 2017.

[9] S.W. Wong, Z.C. Guo, J.Y. Lin, L. Zhu and Q. Zhang, "Triple-mode and triple-band cavity bandpass filter on triplet topology with controllable transmission zeros," *IEEE Access*, vol. 6, pp. 29452-29459, 2018.

[10] S.W. Wong, S.F. Feng, Z.C. Zhang, B.L. Zheng, L. Zhu and Q.X. Chu, "A compact triple-mode dielectric resonator in cylindrical cavity filter," *Microw. and Optical Techn.*, vol. 58, no. 7, pp. 1645-1647, Jul. 2016.

[11] J.Y. Lin, M. Li, S.W. Wong, Y. Yang and X. Zhu, "A cavity triple-mode filter with excitation of L-shape model," *2018 Australian Microwave Symposium (AMS)*, Brisbane, QLD, 2018, pp. 17-18.

[12] Z. Guo, S.W. Wong, J. Lin, L. Zhu and Q.X. Chu, "Triple-mode cavity bandpass filter under excitation via U-shaped slots," *Electron. Lett.*, vol. 53, no. 24, pp. 1580-1582, 23 11 2017.

[13] D. R. Hendry and A. M. Abbosh, "Analysis of compact triple-mode ceramic cavity filters using parallel-coupled resonators approach," *IEEE Trans. Microw. Theory Techn.*, vol. 64, no. 8, pp. 2529-2537, Aug. 2016.

[14] D. R. Hendry and A. M. Abbosh, "Triple-mode ceramic cavity filters with wide spurious-free performance," *IEEE Trans. Microw. Theory Techn.*, vol. 65, no. 10, pp. 3780-3788, Oct. 2017.

[15] C. Kelleci and A. Atalar, "An analytical approach to the design of multiple mode rectangular cavity waveguide filters," *IEEE Trans. Microw. Theory Techn.*, vol. 65,

no. 8, pp. 2857-2865, Aug. 2017.

[16] G. Basavarajappa and R. R. Mansour, "A high-Q quadruple-mode rectangular waveguide resonator," *IEEE Microw. Wireless Compon. Lett.*, vol. 29, no. 5, pp. 324-326, May 2019.

[17] X. Wang, G. Jang, B. Lee and N. Park, "Compact quad-mode bandpass filter using modified coaxial cavity resonator with improved Q- factor," *IEEE Trans. Microw. Theory Techn.*, vol. 63, no. 3, pp. 965-975, Mar. 2015.

[18] M. Memarian and R. R. Mansour, "Quad-mode and dual-mode dielectric resonator filters," *IEEE Trans. Microw. Theory Techn.*, vol. 57, no. 12, pp. 3418-3426, Dec. 2009.

[19] L. Qian and Q. Chu, "A novel quadruple-mode cavity resonator filter with wide spurious-free window," *2018 IEEE MTT-S International Wireless Symposium (IWS)*, Chengdu, 2018.

[20] S.W. Wong, S.F. Feng, L. Zhu and Q. Chu, "Triple- and quadruple-mode wideband bandpass filter using simple perturbation in single metal cavity," *IEEE Trans. Microw. Theory Techn.*, vol. 63, no. 10, pp. 3416-3424, Oct. 2015.

[21] S.W. Wong, S.F. Feng, F. Deng, L. Zhu and Q. Chu, "A quintuple-mode wideband bandpass filter on single metallic cavity with perturbation cylinders," *IEEE Microw. Wireless Compon. Lett.*, vol. 26, no. 12, pp. 975-977, Dec. 2016.

[22] S.F. Feng, S.W. Wong, L. Zhu and Q.X. Chu, "A triple-mode wideband bandpass filter using single rectangular waveguide cavity," *IEEE Microw. Wireless Compon. Lett.*, vol. 27, no. 2, pp. 117-119, Feb. 2017.

[23] B.L. Zheng, S.W. Wong, S.F. Feng, L. Zhu and Y. Yang, "Multi-mode bandpass cavity filters and duplexer with slot mixed-coupling structure," *IEEE Access*, vol. 6, pp. 16353-16362, 2018.

[24] S. Amari and M. Bekheit, "A new class of dual-mode dual-band waveguide filters," *IEEE Trans. Microw. Theory Techn.*, vol. 56, no. 8, pp. 19338-1944, Aug. 2008.

[25]U. Naeem, S. Bila, M. Thevenot, T. Monediere and S. Verdeyme, "A Dual-band bandpass filter with widely separated passbands," *IEEE Trans. Microw. Theory Techn.*, vol. 62, no. 3, pp. 450-456, Mar. 2014.

[26] U. Naeem, A. Perigaud and S. Bila, "Dual-mode dual-band bandpass cavity filters with widely separated passbands," *IEEE Trans. Microw. Theory Techn.*, vol. 65, no. 8, pp. 2681-2686, Aug. 2017.

[27] L. Zhu, R. R. Mansour and M. Yu, "Compact waveguide dual-band filters and diplexers," *IEEE Trans. Microw. Theory Techn.*, vol. 65, no. 5, pp. 1525-1533, May 2017.

[28] Z.C. Guo, S.W. Wong and L. Zhu, "Triple-passband cavity filters with high selectivity under operation of triple modes," *IEEE Trans. Compon., Packag. Manuf. Technol.*, 2019.

[29] L. Zhu, R.R. Mansour, and M. Yu, "Compact triple-band bandpass filters using rectangular waveguide resonators," *2016 IEEE MTT-S International Microwave Symposium (IMS)*, San Francisco, CA, 2016, pp. 1-3.

[30] L. Zhu, R. R. Mansour and M. Yu, "Triple-band cavity bandpass filters," *IEEE Trans. Microw. Theory Techn.*, vol. 66, no. 9, pp. 4057-4069, Sept. 2018.

[31] S.W. Wong, Z.C. Zhang, S.F. Feng, F.C. Chen, L. Zhu, and Q.X. Chu, "Triple-mode dielectric resonator diplexer for base-station applications," *IEEE Trans. Microw. Theory Techn.*, vol. 63, no. 12, pp. 3947-3953, Dec. 2015.

[32] Z.C. Zhang, Q.X. Chu, and S.W. Wong, S.-F. Feng, L. Zhu, Q.-T. Huang, and F.-C. Chen, "Triple-mode dielectric-loaded cylindrical cavity diplexer using novel packaging technique for LTE base-station applications," *IEEE Trans. Compon., Packag. Manuf. Technol.*, vol. 6, no. 3, pp. 383-389, Mar. 2016.

[33] D. R. Hendry and A. M. Abbosh, "Compact high-isolation base-station duplexer using triple-mode ceramic cavities," *IEEE Trans. Ind. Electron.*, vol. 65, no. 10, pp. 8092-8100, Oct. 2018.

[34] J.Y. Lin, S.W. Wong and L. Zhu, "High-isolation diplexer on triple-mode cavity filters," *2017 IEEE MTT-S International Microwave Symposium (IMS)*, Honolulu, HI, 2017, pp. 1196-1199.

[35] J.Y. Lin, S.W. Wong, L. Zhu and Q.X. Chu, "Design of miniaturized triplexers via sharing a single triple-mode cavity resonator," *IEEE Trans. Microw. Theory Techn.*, vol. 65, no. 10, pp. 3877-3884, Oct. 2017.

[36] H. Hu and K. Wu, "A deterministic EM design technique for general waveguide dual-mode bandpass filters," *IEEE Trans. Microw. Theory Techn.*, vol. 61, no. 2, pp.

800-807, Feb. 2013.

[37] H. Hu, K. Wu and R. J. Cameron, "Stepped circular waveguide dual-mode filters for broadband contiguous multiplexers," *IEEE Trans. Microw. Theory Techn.*, vol. 61, no. 1, pp. 139-145, Jan. 2013.

[38] B. Yassini and M. Yu, "Ka-band dual-mode super *Q* filters and multiplexers," *IEEE Trans. Microw. Theory Techn.*, vol. 63, no. 10, pp. 3391-3397, Oct. 2015.

[39] J.Y. Lin, S.W. Wong, Y.M. Wu, L. Zhu, Y. Yang and Y. He, "A new concept and approach for integration of three-state cavity diplexer based on TMRs," *IEEE Trans. Microw. Theory Techn.*, vol. 66, no. 12, pp. 5272-5279, Dec. 2018.

[40] J.Y. Lin, S.W. Wong, Y.M. Wu, Y. Yang, L. Zhu and Y. He, "Three-way multiple-mode cavity filtering crossover for narrowband and broadband applications," *IEEE Trans. Microw. Theory Techn.*, vol. 67, no. 3, pp. 896-905, Mar. 2019.

[41] J. Xu and X. Y. Zhang, "Dual-channel dielectric resonator filter and its application to doherty power amplifier for 5G massive MIMO system," *IEEE Trans. Microw. Theory Techn.*, vol. 66, no. 7, pp. 3297-3305, Jul. 2018.

[42] J. Xu, X. Y. Zhang and Q. Xue, "Dual-channel filter based on dielectric resonator for 5G massive MIMO system," *2018 IEEE MTT-S International Wireless Symposium (IWS)*, Chengdu, 2018, pp. 1-3.

[43] J. Xu, H. Li, X. Y. Zhang, Y. Yang, Q. Xue and E. Dutkiewicz, "Compact dual-channel balanced filter and balun filter based on quad-mode dielectric resonator," *IEEE Trans. Microw. Theory Techn.*, vol. 67, no. 2, pp. 494-504, Feb. 2019.

[44] J.-X. Chen, Y. Zhan, W. Qin, Z.-H. Bao, and Q. Xue, “Novel narrow-band balanced bandpass filter using rectangular dielectric resonator,” *IEEE Microw. Wireless Compon. Lett.*, vol. 25, no. 5, pp. 289-291, May 2015.

[45] J.-X. Chen, Y. Zhan, W. Qin, Z.-H. Bao, and Q. Xue, “Analysis and design of balanced dielectric resonator bandpass filter,” *IEEE Trans. Microw. Theory Techn.*, vol. 64, no.5, pp. 1476-1483, May 2016.

[46] J.-X. Chen, Y. Zhan, W. Qin, and Z.-H. Bao, “Design of high-performance filtering balun based on TE01δ-mode dielectric resonator,” *IEEE Trans. Ind.*

Electron, vol. 64, no. 1, pp. 451-458, Jan. 2017.

[47] J.-X. Chen, J. Li, Y. Zhan, W. Qin, J. Shi, and Z.-H. Bao, “Design of balanced and balun filters using dual-mode cross-shaped dielectric resonators,” *IEEE Trans. Microw. Theory Techn.*, vol. 65, no.4, pp. 1226-1234, Apr. 2017.

[48] S.-W. Wong, J.-Y. Lin, Y. Yang, H. Zhu, R.-S. Chen, L. Zhu, and Y. He, “Cavity balanced and unbalanced diplexer based on triple-mode resonator,” *IEEE Trans. Ind. Electron*., vol. 67, no. 6, pp. 4969-4979, Jun. 2019.

Chapter 2 Cavity Filtering Magic-T and Its Integrations Into Balanced-to-Unbalanced Power Divider and Diplexing Power Divider

2.1 Introduction

Power combiners/dividers provide the function of combining/splitting the signals from/to multiple devices with the required power level. It needs to process the property of low insertion-loss, high isolation, low magnitude and phase imbalance. Many different kinds of technologies and design methods are introduced to construct power dividers (PDs) with good characteristics. As a commonly employed approach, microstrip structures designed on planar circuit boards (PCBs) are widely used for power divider designs [1]-[5]. In addition, dielectric resonator [6], integrated passive device (IPD) process [7], substrate integrated waveguide [8], rectangular waveguide [9], as well as low temperature co-fired ceramic technology [10], have been comprehensively applied to design power dividers in the last decade. However, signal isolations between the output ports are still an obvious design challenge among these works. Usually, lumped elements or lossy resistors are adapted to construct an isolation network of a power divider. For example, reference [11] presents an isolation network composed of several combined *RLC* and *LC* networks, while reference [12] introduces an air-bridge resistor and two slot-lines with resistors to improve the isolation performance of the power divider.

In general, other than applying lumped elements or resistors among output ports, solutions to obtain a power divider with good port-isolation are still limited. Especially in cavity circuits, isolation resistors are often difficult to integrate on a metal cavity. Magic-T, one type of four-port impedance-matched network, can provide power combining/splitting also with in-phase and out-of-phase signals. Due to the existence of the isolation port, the output ports of the Magic-T can be isolated automatically, which inspires us to create a novel method that can realize high-isolation power divider without the need for a resistor. It has been widely implemented in balanced mixers, amplifiers, diplexers, and antenna systems.

Conventional waveguide-type magic-T has been widely investigated in [13]-[18]. They all focus on broadband impedance matching as a transmission junction, by means of the following methods: 1) off-centered metallic posts [14], 2) stepped conducting cone [15], 3) four coplanar arms inspired waveguide-to-microstrip transition [16], and 4) ridge waveguide coupling structure [17]. For the purpose of reducing interconnection loss, manufacturing cost, as well as circuit miniaturization, integration of multiple functions in a single structure has been further investigated and developed. For example, filtering magic-T has been achieved in [19] and [20]. In [19], two orthogonal modes, namely TE_{201} and TE_{102} modes, are adopted to design a kind of 3^{rd}-order filtering magic-T operating at 24 GHz with 6% bandwidth. In [20], vertical and horizontal TM_{110} modes in a circular SIW cavity are adopted to achieve 2^{nd}-order bandpass response operating at 9 GHz with 70 MHz bandwidth. However, aforementioned multiple functions can only accommodate two integrated functions. Integration of three or more functions has not been reported, according to the open literature, to the best of the author's knowledge.

In this chapter, cavity filtering magic-T integrated with multiple functions is investigated by using triple-mode resonators (TMRs). Two applications of filtering power divider in integrations with balanced and duplexing functions are also presented. The first application is balanced-to-unbalanced (B2U) power divider. This power divider connects a pair of balanced inputs and two single-ended outputs. Thus, it has an attractive feature of high immunity to common mode environmental noise and electromagnetic interaction. It can be divided into two categories: out-of-phase power divider [21]-[25] and in-phase power divider [26]-[29]. All of them are designed using printed-circuit-board (PCB) technology with high-performance, but the isolation and common-mode (CM) suppression are quite limited. In [30], for the first time, a method of achieving in-phase and out-of-phase power divider functions at outputs, simultaneously in one structure, is proposed.

The second application is duplexing power divider. Duplexer is a device that can transfer different frequency-bands into different channels. Integrating power dividers and diplexers together can obtain a device owning both duplexing capability and power division capability. [31] proposes duplexers with integrated power division capabilities that do not require isolation resistors. However, both of them cannot generate isolation between output ports of power divider under the same frequency channel of the duplexer. Reference [32] presented three novel duplexing power dividers based on microstrip line to achieve the function of duplexing power division, but the layouts of these duplexing power dividers are complex and isolation between different channels are not relevant high. To the best of the author's knowledge, duplexing power divider with high-isolation realized by magic-T has not yet been reported before in literature.

For both of the presented power divider designs, multiple functions, including filtering, duplexing/balancing, power division, are integrated into one cavity structure simultaneously, which further miniaturizes the circuit volume and decreases the insertion loss and fabricated cost. Furthermore, all ports in the designs are impedance matched and the isolation between outputs is high without any installation of isolation resistors

2.2 Waveguide Filtering Magic-T Design

Fig. 2.1(a) depicts the topology of a magic-T based on triple-mode resonators (TMRs). Port 4 acts as a difference port which is coupled with electromagnetic (EM) waves of TE_{101} mode. EM waves propagate evenly into two outputs port 1 and port 2 with 180 degree phase difference. Conversely, port 3 acts as a sum port which is coupled with EM waves of TM_{110} modes. EM waves propagate evenly into port 1 and port 2 with 0 degree phase difference. According to this topology, the geometrical structure of a cavity filtering magic-T with 2nd-order response is presented in Fig. 2.1(b). It consists of three TMRs, the slot coupled with waveguide port 4 is placed on the *yoz* plane and perpendicular to *y*-axis, hence this excites the electric-field $\overrightarrow{E_y}$ (marked as solid line) in accordance with that of TE_{101} mode [33], [34]. Due to the modal orthogonality of three fundamental modes [35], the long-side orientation of slot 2 is perpendicular to the *y*-axis so that only TE_{101} mode can propagate through this slot while other fundamental modes are prohibited.

Therefore, EM waves of TE_{101} mode are coupled with port 4 and propagate into TMR 3, then pass through slot 2 into TMR 1. Herein, due to the offsetting of port 1, port 2 and their respective slots, TE_{101} mode is evenly transmitted into these ports. In terms of phase performance, as depicted in Fig. 2.1(b), electric-field orientations of slots at port 1 and port 2 are opposite, which means that out-of-phase performance can be achieved when TE_{101} mode propagates. Similarly, the orientation of the slot coupled with port 3 is perpendicular to the *z*-axis, hence exciting the electric-field $\overrightarrow{E_z}$ (marked as dashed line) in accordance with that of TM_{110} mode. The long-side orientation of slot 1 is perpendicular to the *z*-axis so that TM_{110} mode can propagate through it. Finally, the

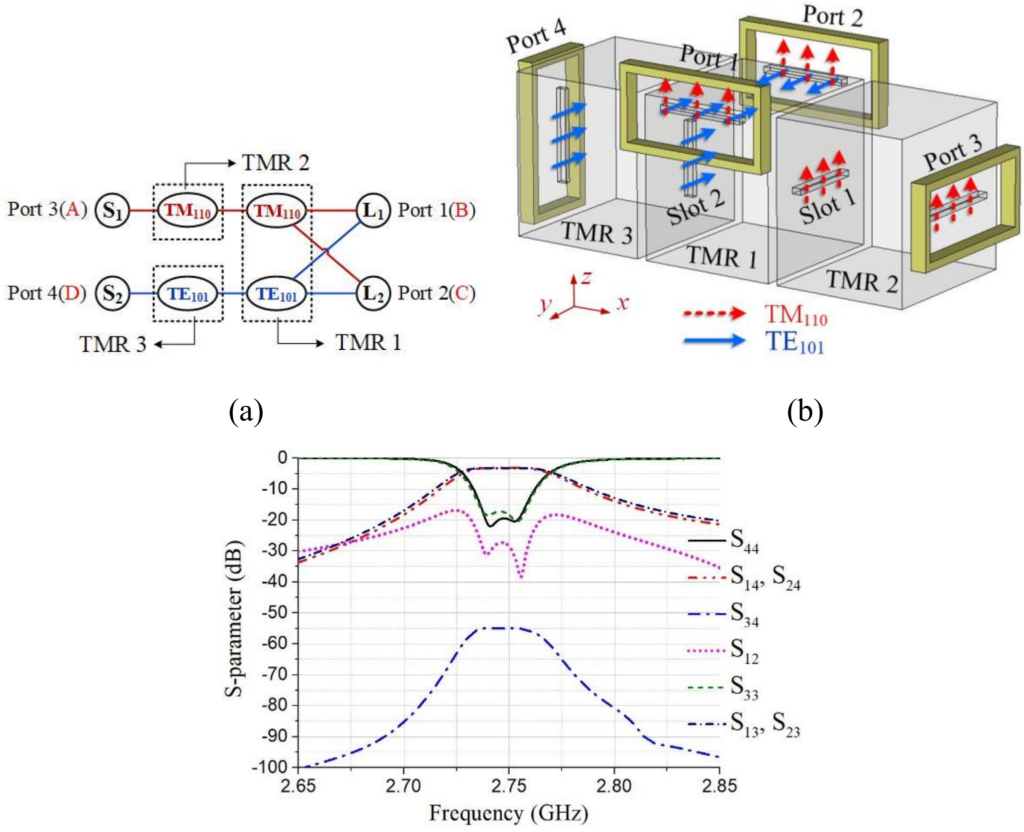

(a) (b)

(c)

Fig. 2.1. Cavity magic-T with: (a) topology, (b) 2nd-order geometrical structure, (c) simulated S-parameter curves.

EM waves of TM_{110} mode are transmitted into port 1 and port 2 evenly, and in-phase performance at two output ports can be achieved when TM_{110} mode propagates.

Fig. 2.1(c) illustrates S-parameters of the proposed 2nd-order cavity magic-T. Differential response $|S_{44}|$ is dominated by TE_{101} mode. It has the same resonant frequency with common response $|S_{33}|$ dominated by TM_{110} mode, both of which resonate at 2.75 GHz with 3-dB bandwidth of 40 MHz. Isolations between two response ports are better than 50 dB denoted as $|S_{34}|$, while isolation between two output ports denoted as $|S_{12}|$ can reach 20 dB in the resonant frequency range.

2.3 The Theory and Design of Balanced-to-Unbalanced Power Divider

Balanced-to-unbalanced (B2U) magic-T, which includes B2U in-phase power divider and B2U out-of-phase power divider, is demonstrated. According to the schematics shown in Fig. 2.2, it is regarded as the integration of two baluns and one single-ended

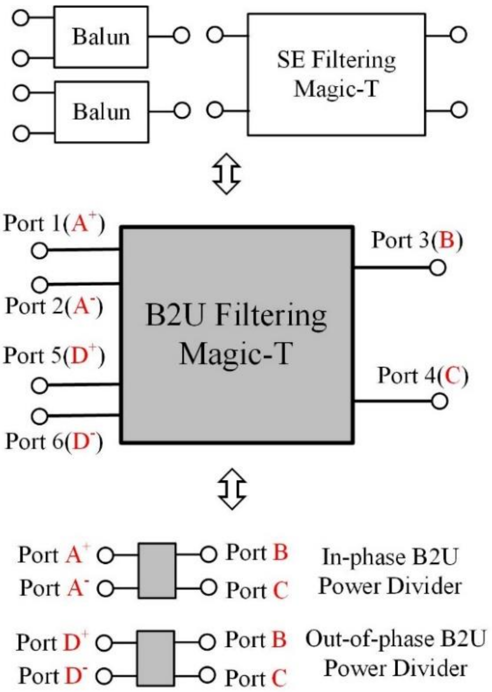

Fig. 2.2. The schematic diagram of B2U magic-T.

(SE) filtering magic-T component. Subsequently, it includes six ports categorized as two groups: four input ports (port 1, port 2 and port 5, port 6), and two output ports (port 3 and port 4). In addition, port 1 and port 2 are a pair of balanced ports A, port 5 and port 6 are a pair of balanced ports D, while port 3 and port 4 are single-ended output ports B and C, respectively. Due to the inherent property of magic-T, as analyzed in Section II, port B and port C are isolated. Based on this, two achieved functions are summarized as：

1) In-phase B2U power divider with balanced input ports A, SE output ports B and C, and isolated ports D.

2) Out-of-phase B2U power divider with balanced inputs D, SE output ports B and C, and isolated ports D.

In this B2U magic-T, the relevant mixed-mode scattering matrix (S_{mm}) of the

$$S_{mm}=\begin{bmatrix} S_{ddAA} & S_{cdAA} & S_{sdBA} & S_{sdCA} & S_{ddDA} & S_{cdDA} \\ S_{dcAA} & S_{ccAA} & S_{scBA} & S_{scCA} & S_{dcDA} & S_{ccDA} \\ S_{dsAB} & S_{csAB} & S_{ssBB} & S_{ssCB} & S_{dsDB} & S_{csDB} \\ S_{dsAC} & S_{csAC} & S_{ssBC} & S_{ssCC} & S_{dsDC} & S_{csDC} \\ S_{ddAD} & S_{cdAD} & S_{sdBD} & S_{sdCD} & S_{ddDD} & S_{cdDD} \\ S_{dcAD} & S_{ccAD} & S_{scBD} & S_{scCD} & S_{dcDD} & S_{ccDD} \end{bmatrix} \qquad (2\text{-}1)$$

differential model can be expressed as shown in equation (2-1), where s is the single-end response, d is the differential-mode excitation and c is the common-mode excitation. The first and second letter of the subscript represents the response and stimulus modes, while the last two letters of the subscript represent the response and stimulus ports, respectively. For instance, S_{csDB} denotes the S-parameter with single-end response excited at Port B and common-mode excitation at Port D.

To achieve impedance matching of the proposed B2U magic-T, the relative conditions are plotted as:

$$S_{ddAA} = S_{ssBB} = S_{ssCC} = S_{ddDD} = 0 \tag{2-2a}$$

The equal power division with in-phase and out-of-phase response can be generated when the following conditions are met:

$$S_{dsAB} = S_{dsAC} = 1/\sqrt{2} \tag{2-2b}$$

$$S_{dsDB} = -S_{dsDC} = 1/\sqrt{2} \tag{2-2c}$$

The input and output isolation should follow the condition below:

$$S_{ddAD} = S_{ccAD} = S_{ssBC} = 0 \tag{2-2d}$$

The common-mode (CM) suppression should be considered when the following conditions are met:

$$S_{ccAA} = 1 \text{, } S_{dcAA} = S_{csAB} = S_{csAC} = 0 \tag{2-2e}$$

$$S_{ccDD} = 1 \text{, } S_{dcDD} = S_{csDB} = S_{csDC} = 0 \tag{2-2f}$$

$$S_{cdAD} = S_{dcAD} = 0 \tag{2-2g}$$

To achieve the standard matrix [S_{std}] derived from the mixed-mode matrix [S_{mm}], the translation between standard S-matrix and the mixed-mode scattering matrix are defined as:

$$S_{ddNN} = \left(S_{N^+N^+} - S_{N^+N^-} - S_{N^-N^+} + S_{N^-N^-} \right) \Big/ 2 \tag{2-3a}$$

$$S_{ccNN} = \left(S_{N^+N^+} + S_{N^+N^-} + S_{N^-N^+} + S_{N^-N^-} \right) \Big/ 2 \tag{2-3b}$$

$$S_{cdNN} = \left(S_{N^+N^+} - S_{N^+N^-} + S_{N^-N^+} - S_{N^-N^-} \right) \Big/ 2 \tag{2-3c}$$

$$S_{dcNN} = \left(S_{N^+N^+} + S_{N^+N^-} - S_{N^-N^+} - S_{N^-N^-} \right) \Big/ 2 \tag{2-3d}$$

$$S_{sdMN} = \left(S_{MN^+} - S_{MN^-} \right) \Big/ \sqrt{2} \tag{2-3e}$$

$$S_{dsNM} = \left(S_{N^+M} - S_{N^-M} \right) \Big/ \sqrt{2} \tag{2-3f}$$

$$S_{scMN} = \left(S_{MN^+} + S_{MN^-} \right) \Big/ \sqrt{2} \tag{2-3g}$$

$$S_{csNM} = \left(S_{N^+M} + S_{N^-M} \right) \Big/ \sqrt{2} \tag{2-3h}$$

$$S_{ssMM} = S_{MM} \tag{2-3i}$$

Where $N = A$, D and $M = B$, C, plus sign and minus sign represent positive and negative of balanced ports, respectively. Combining (2) and (3) into the standard matrix, which can be finally simplified as:

$$S_{std} = \begin{bmatrix} S_{A^+A^+} & S_{A^-A^+} & S_{BA^+} & S_{CA^+} & S_{D^+A^+} & S_{D^-A^+} \\ S_{A^+A^-} & S_{A^-A^-} & S_{BA^-} & S_{CA^-} & S_{D^+A^-} & S_{D^-A^-} \\ S_{A^+B} & S_{A^-B} & S_{BB} & S_{CB} & S_{D^+B} & S_{D^-B} \\ S_{A^+C} & S_{A^-C} & S_{BC} & S_{CC} & S_{D^+C} & S_{D^-C} \\ S_{A^+D^+} & S_{A^-D^+} & S_{BD^+} & S_{CA^+} & S_{D^+D^+} & S_{D^-D^+} \\ S_{A^+D^-} & S_{A^-D^-} & S_{BD^-} & S_{CD^-} & S_{D^+D^-} & S_{D^-D^-} \end{bmatrix}$$

$$= \frac{1}{2} \begin{bmatrix} 1 & 1 & 1 & 1 & 0 & 0 \\ 1 & 1 & -1 & -1 & 0 & 0 \\ 1 & -1 & 0 & 0 & 1 & -1 \\ 1 & -1 & 0 & 0 & -1 & 1 \\ 0 & 0 & 1 & -1 & 1 & 1 \\ 0 & 0 & -1 & 1 & 1 & 1 \end{bmatrix} \tag{2-4}$$

The [S_{std}] matrix is the standard matrix derived from the mixed-mode scattering matrix [S_{mm}] and it meets the property of B2U magic-T.

Three fundamental modes, TE_{011}, TE_{101}, and TM_{110}, in a single TMR cavity, are

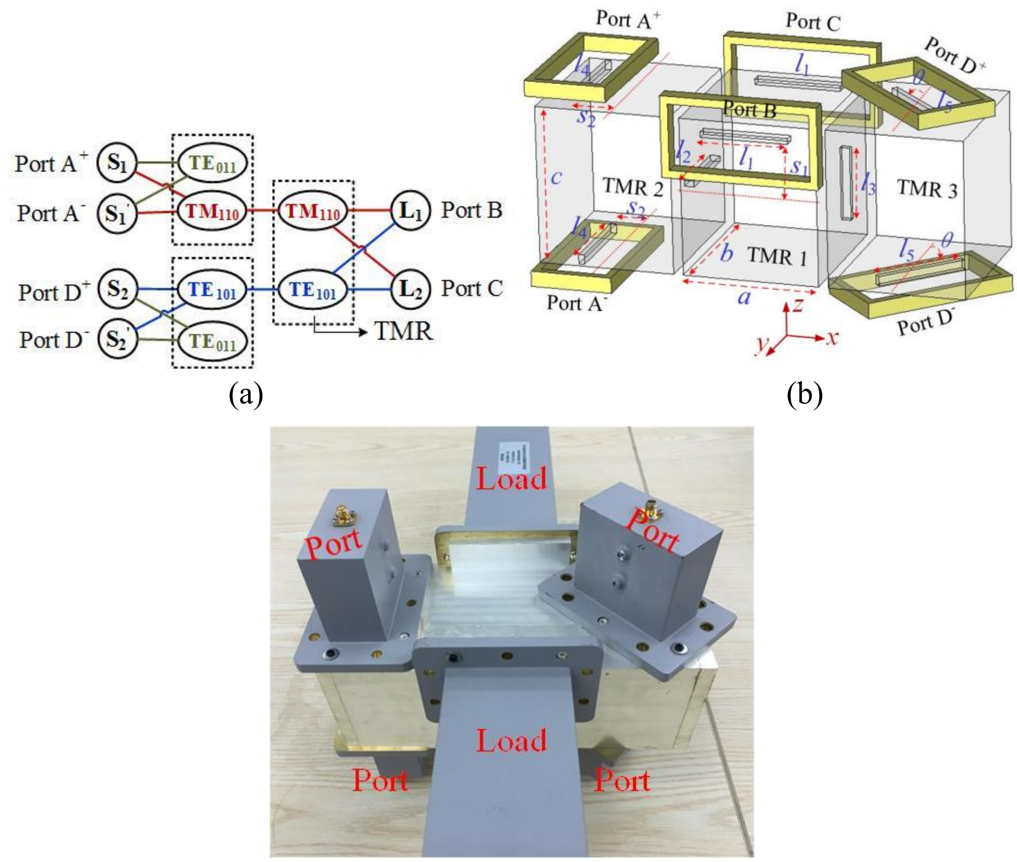

(a) (b)

(c)

Fig. 2.3. Cavity B2U 2nd-order magic-T with: (a) topology, (b) geometrical structure, (c) photograph of the fabricated structure with assembled waveguide ports.

adopted to implement this schematic diagram as illustrated in Fig. 2.3(a). Still, port B and port C act as two single-ended output ports. However, single-ended input ports A and D in Fig. 1(a), are converted into balanced ports A$^+$, A$^-$ and D$^+$, D$^-$. Fig. 2.3(b) presents the geometrical structure of the cavity B2U 2nd-order magic-T according to this topology. Port B and port C are shifted s_1 upward from the surface center of TMR 1 to absorb EM waves of TM$_{110}$ and TE$_{101}$ modes.

To achieve balanced functions, out-of-phase mode needs to be excited at two pairs of input ports, respectively. In [36], two methods to achieve out-of-phase mode performance are presented by means of “rotation” and “offsetting”, respectively. For the balanced input ports A, by adopting “offsetting” method, they are shifted s_2 from the surface center versus *xoy* plane of the TMR 2 cavity, with long-side orientation of the slot perpendicular to the *x*-axis. Therefore, two fundamental modes - TE$_{011}$ and TM$_{110}$ - are excited. Out-of-phase mode TM$_{110}$ is adopted to propagate through the slot with a length of l_2 while in-phase mode TE$_{011}$ is prohibited. Similarly, by adopting

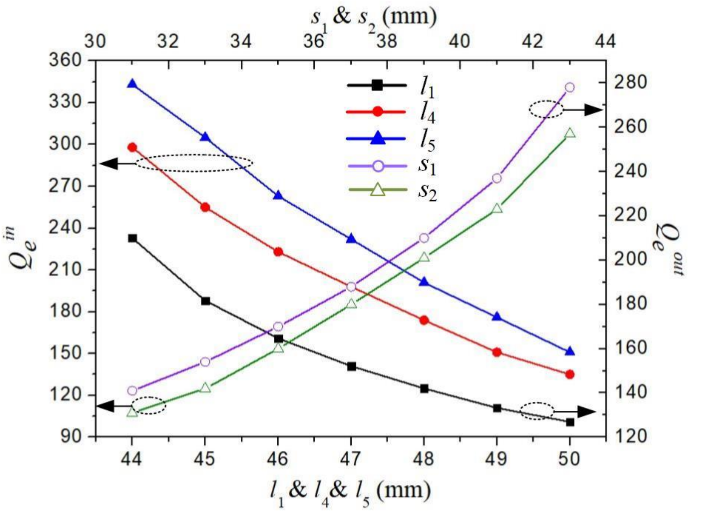

Fig. 2.4. Variation of Q_e^{in} and Q_e^{out} versus varied parameters: l_1, l_4, l_5, s_1 and s_2.

"rotation" method, balanced input ports D^+, D^- are rotated with the angle of θ on the surface center versus *xoy* plane of TMR 3 cavity to excite TE_{011} and TE_{101} modes. The out-of-phase mode TE_{101} propagates through the slot with a length of l_3 while in-phase mode TE_{011} is prohibited.

In the proposed B2U magic-T structure, both channels are dominated by TE_{101} and TM_{110} modes resonating at the same frequency, following the filter synthesis theory. Considering the specifications of the fractional bandwidth of the channel are set as 1.5% at 2.75 GHz, the formulas of external quality factors Q_e and coupling coefficients K are depicted as:

$$Q_e = \frac{g_0 g_1}{FBW} \tag{2-5a}$$

$$K_{12} = \frac{FBW}{\sqrt{g_1 g_2}} \tag{2-5b}$$

where g_0, g_1 and g_2 are the low-pass prototype element values of filter synthesis which can be set as $g_0=1$, $g_1=g_2=1.4142$. After substituting the chosen values, the calculated external quality factor and coupling coefficient are $Q_e=94.3$ and $K_{12}=0.01$, respectively.

In [34], the physical models to extract Q_e and K so as to match the theoretical values are presented. The variations of input external quality values Q_e^{in} and output external quality values Q_e^{out} versus varied parameters: l_1, l_4, l_5, s_1 and s_2, are plotted in Fig. 2.4. By properly setting the suitable values, the prescribed Q_e^{in} and Q_e^{out} can be implemented to satisfy the required filtering response of each channel.

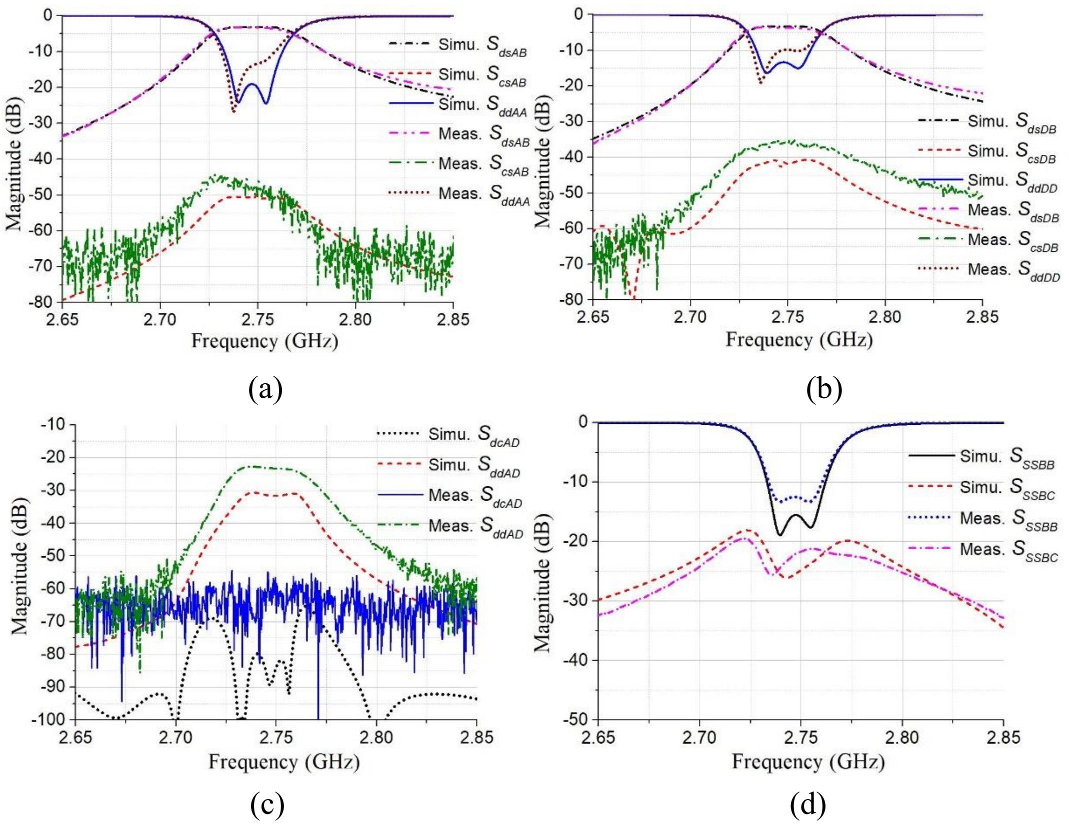

(a) (b)

(c) (d)

Fig. 2.5. Simulated and measured S-parameters of the 2nd-order B2U cavity magic-T. (a) S_{dsAB} & S_{csAB} & S_{ddAA}. (b) S_{dsDB} & S_{csDB} & S_{ddDD}. (c) S_{dcAD} & S_{ddAD}. (d) S_{ssBB} & S_{ssBC}.

A photograph of the fabricated magic-T is presented in Fig. 2.3(c). Silver-plated aluminum is the material for fabricating the proposed full-metal cavity filtering Magic-T using computer numerical control (CNC) technology. WR284-type rectangular waveguides are used to feed the ports. The simulated and measured results are plotted in Fig. 2.5. It is noted in Figs. 2.5(a)-(b) that two differential-mode channels, denoted as S_{ddAA} and S_{ddDD}, have the same resonant frequencies. They both resonate at 2.74 GHz with a 3-dB bandwidth of 40 MHz and measured insertion loss of 3.17 dB, while the common-mode suppression can reach 35 dB. Depicted in Fig. 2.5(c), the differential-mode isolation between two inputs can reach 20 dB and common-mode isolation is better than 55 dB. It is also clear that, according to Fig. 2.5(d), the isolation between two single-ended outputs can reach 20 dB. The physical dimensions of the proposed structure are summarized in Table 2.1. The width and thickness of all coupling slots are 3 mm and 5 mm, respectively.

TABLE 2.1

PHYSICAL DIMENSIONS OF THE B2U CAVITY MAGIC-T

a = 70 mm	b = 80 mm	c = 81 mm	S_1 = 37 mm
θ = 43 °	l_1= 45 mm	l_2= 39.8 mm	S_2 = 19 mm

$l_3 = 39.2$ mm	$l_4 = 47.6$ mm	$l_5 = 48.4$ mm	

2.4 The Theory and Design of Diplexing Power Divider

As reported in Section II, the proposed magic-T component can also be used to design a duplexing power divider. As illustrated in Fig. 2.6, it integrates one duplexer and two power dividers, port 1 acts as input port, while output ports can be divided into two groups, i.e., group 1 (port 2, port 3) and group 2 (port 5, port 6), which work in different channels of duplexing power divider. To achieve isolation between output ports of the duplexing power divider, instead of installing lossy resistors, extra isolated ports are added to construct two magic-Ts in a duplexing power divider. Consequently, isolation between output ports of a same frequency channel can be realized in the duplexer automatically. As explained in Fig. 2.6, port 4 is installed as the isolated port in the downlink magic-T, while port 7 is installed in the uplink magic-T. Finally, a duplexing power divider with good isolation between two pairs of output ports is achieved, including the isolation between the outputs at the same frequency channel and at different frequency channels.

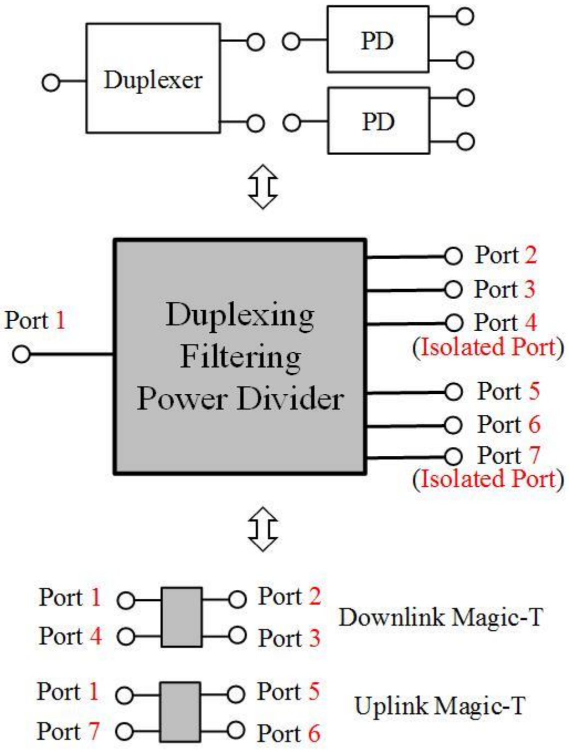

Fig. 2.6. The schematic diagram of duplexing power divider.

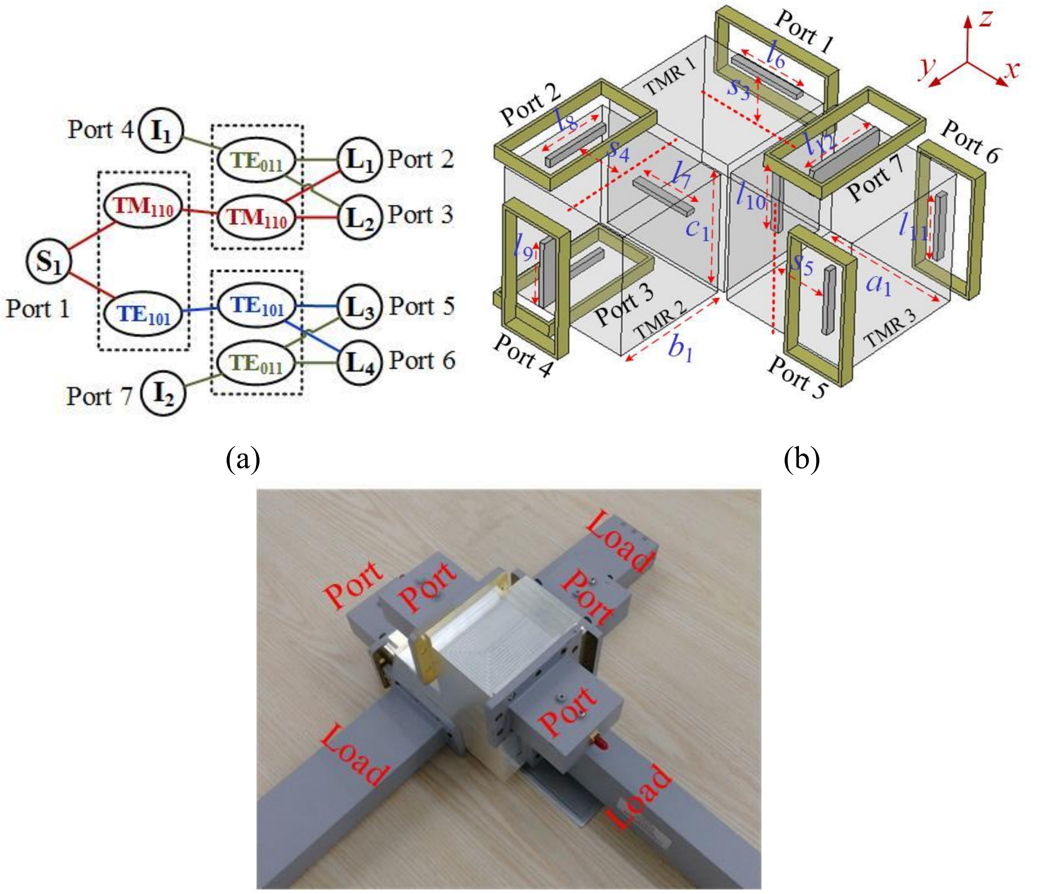

(a) (b)

(c)

Fig. 2.7. Cavity 2nd-order duplexing power divider with: (a) topology, (b) geometrical structure, (c) photograph of the fabricated structure.

As illustrated in Fig. 2.7, a duplexing power divider composed of three TMR cavities is designed and simulated. The proposed duplexing power divider contains seven ports including one input port (port 1) and four output ports, which are divided into group 1 (port 2 and port 3), group 2 (port 5 and port 6), and two isolated ports (port 4 and port 7), respectively. TE_{101} mode and TM_{110} mode of the TMR are excited by an offset slot at port 1 to compose the two channels of the proposed duplexing power divider. The offset slot, coupled with the EM waves from port 1, is set as s_3 away from the center position to excite the electric-field orientation $\overrightarrow{E_y}$ which is in accordance with the directions of TE_{101} mode. Offsetting of this slot is contributed to obtain the maximum magnetic energies of the TE_{101} mode. Simultaneously, since the long-side orientation of this slot coupled with port 1 is vertical to z-axis, which is in accordance with the orientation of TM_{110} mode with the electric-field $\overrightarrow{E_z}$. Accordingly, TM_{110} mode of the triple-mode resonator is excited. After being excited at TMR 1, the resonant energies

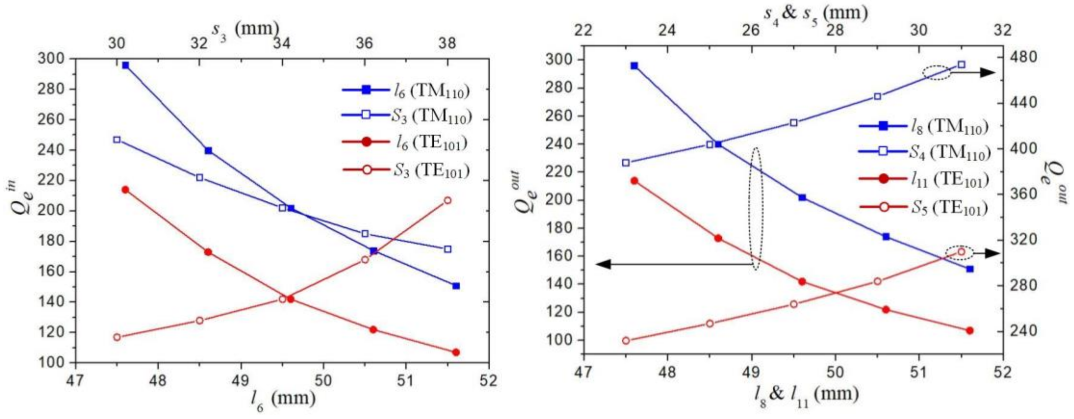

(a) (b)

Fig. 2.8. Value variation of Q_e^{in} and Q_e^{out} versus varied parameters: (a) l_6, s_3, (b) l_8, s_4 and l_{11}, s_5.

of TM$_{110}$ mode propagate into TMR 2 and transmit to port 2 and port 3 evenly due to their symmetrical structures. The EM waves of the TE$_{101}$ mode propagate into TMR 3 evenly at two symmetrical ports, port 5 and port 6, respectively. Therefore, the function of a duplexing power divider is implemented. To achieve isolations between two pairs of output ports, port 4 and the slot with a length of l_9 are installed on the surface center versus *xoz* plane of TMR 2 cavity and perpendicular to *x*-axis. Thus, TE$_{011}$ mode is excited. Therefore, ports 1-4 compose a single-ended (SE) magic-T, where port 2 and port 3 are isolated. Similarly, port 7 and the slot with a length of l_{12} are installed on the surface center versus *xoy* plane of the TMR 3 cavity which is perpendicular to *x*-axis. Thus, TE$_{011}$ mode is excited. Port 1, port 5, port 6 and port 7 compose a SE magic-T, where port 5 and port 6 are isolated.

To further develop the design theory, the related equations 5(a)-(b) are used to calculate external quality factor and coupling coefficient versus frequency response, of the proposed duplexing power divider. For the fractional bandwidth (FBW) specification of two channels set at 0.7% and 1%, the external quality factors and coupling coefficients of the first and the second channels can be deduced as 202, 0.0049, 141.4, 0.007, respectively.

The physical model in [34] is used to extract Q_e and K of each channel of the proposed duplexing power divider. The parameters l_6 and s_3, shown in Fig. 2.8(b), are used to control and balance the input external quality values of two channels dominated by TM$_{110}$ (Q_e^{I}) and TE$_{101}$ (Q_e^{II}), respectively. For output external quality values, l_8 and

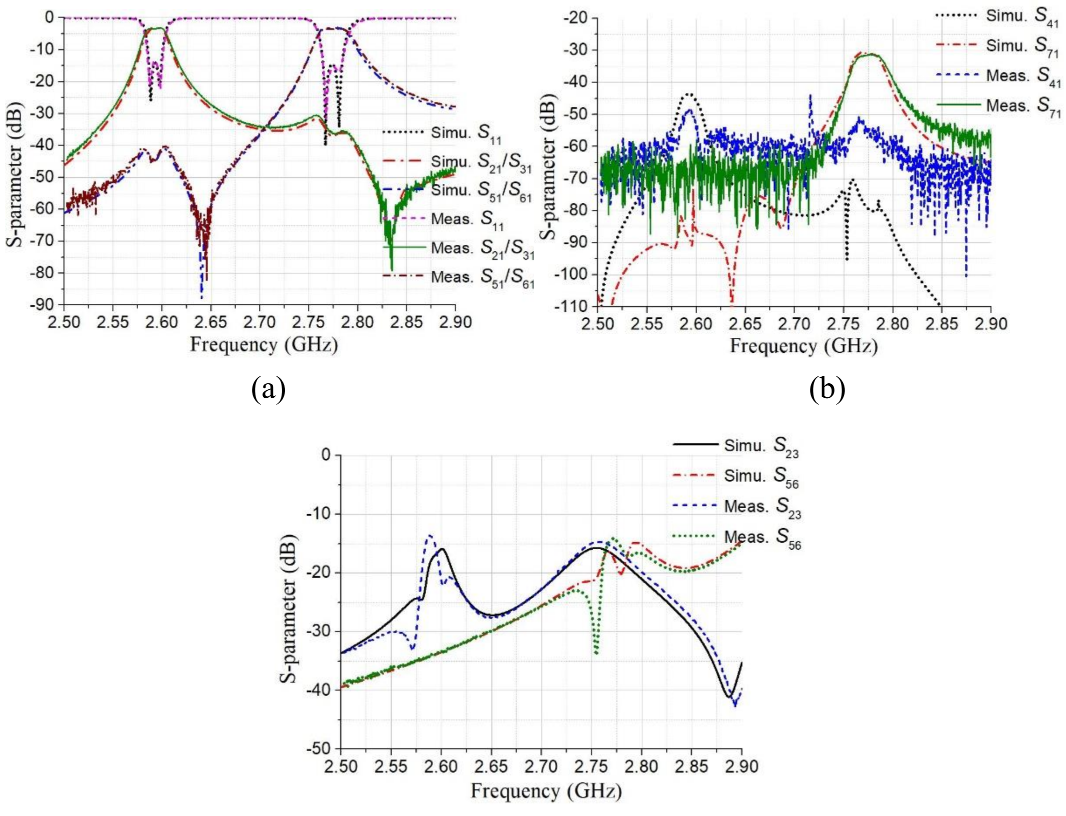

(a) (b)

(c)

Fig. 2.9. Simulated and measured S-parameters of the proposed 2nd-order duplexing power divider. (a) $|S_{11}|$, $|S_{21}|/|S_{31}|$, $|S_{51}|/|S_{61}|$, (b) $|S_{41}|$, $|S_{71}|$ and (c) $|S_{23}|$, $|S_{56}|$.

s_4 are used to control that of lower channel dominated by TM_{110} mode, while l_{11} and s_5 are used to control that of upper channel dominated by TE_{101} mode. To meet the filtering response for each channel, the values in Fig. 8 should be properly considered.

Fig. 2.7(c) presents photograph of the fabricated duplexing power divider. Silver-plated aluminum is the material for fabricating the proposed full-metal cavity duplexing power divider using CNC technology. WR284-type rectangular waveguides are used to feed the ports. Figs. 2.9(a)-(c) illustrate the simulated and measured S-parameter responses of the proposed duplexing power divider. As can be seen from Fig. 2.9(a), TM_{110} mode resonates at 2.58 GHz with a 3-dB bandwidth of 20 MHz and a measured insertion loss of 3.2 dB. While TE_{101} mode resonates at 2.76 GHz with a 3-dB bandwidth of 32 MHz and a measured insertion loss of 3.3 dB. In Fig. 2.9(b), the isolation between input port 1 and two isolated ports, namely port 4 and port 7, are better than 45 dB and 30 dB, respectively, as shown by $|S_{41}|$ and $|S_{71}|$. In Fig. 2.9(c), the isolation between port 2 and port 3 can reach 14 dB, while the isolation between port 5 and port 6 can reach 14 dB, within the whole 2.5 GHz to 2.9 GHz frequency range.

Table 2.2 shows the physical dimensions of the proposed duplexing power divider. Width of each coupling slots are chosen as 3 mm.

TABLE 2.2
PHYSICAL DIMENSIONS OF THE DUPLEXING POWER DIVIDER

a_1 = 80 mm	b_1 = 70 mm	c_1 = 80 mm	S_3 = 34 mm
S_4 = 25 mm	S_5 = 29 mm	l_6= 49.6 mm	l_7= 36.6 mm
l_8= 45.6 mm	l_9= 51.4 mm	l_{10}= 37.6 mm	l_{11}= 45.6 mm
l_{12}= 54 mm			

Table 2.3 presents a comparison between the proposed power divider and other reported structures. Waveguide-based broadband magic-Ts have been implemented in [15]-[17], but neither filtering nor duplexing capacity has been integrated. It is noted that PD with duplexing capacity based on PCB process and lossy resistors are adopted to achieve isolation between outputs [31]-[32]. Due to the integration of a dual-band filter for high selectivity, the duplexing PD in [32] suffers serious insertion loss at two different operational channels, respectively. Our proposed duplexing power divider has the advantages in lower frequency ratio, better filtering capability, narrower FBW, lower measured insertion loss and higher power handling due to full-metal circuit.

TABLE 2.3
COMPARISON BETWEEN THE PROPOSED POWER DIVIDER AND OTHER REPORTED ONES.

	Implemented Material	Filtering Capability	Duplexing Capability	Central Frequency (GHz)	Achieved Bandwidths (%)	Isolation Between Outputs
[15]	Metal Cavity	No	No	9.3	20	-
[16]	Metal Cavity	No	No	30.8	21	-
[17]	Metal Cavity	No	No	8.6	18	-
[19]	LTCC	Yes	No	24	6	-
[31]	PCB	No	Yes	1.0/2.5	N.A.	N.A.
[32]	PCB	Yes	Yes	1.8/2.4	4.4/2.7	20/20
This work	Metal Cavity	Yes	Yes	2.58/2.76	0.7/1	14/14

N.A. means not available.

2.5 Conclusion

In this chapter, a novel magic-T component is proposed for designing in-phase and out-of-phase power dividers, where all ports are impedance-matched with good port-isolations between outputs, without using any lossy resistors. It is worth noting that, for the first time, multiple functions are integrated into a multiple-mode resonator cavity structure, which further miniaturizes the circuit volume with an improved insertion loss and a reduced fabrication cost. For validation, two design examples are presented. The first design is a balanced-to-unbalanced filtering magic-T, it integrates baluns, filters and magic-T in one structure. The second design is a duplexing filtering power divider, it integrates duplexer, filters and power dividers in one structure. The two designs are fabricated and measured. The results of measurements and simulations are well matched, so our predicted design methodology is verified.

2.6 References

[1] C. Tang and J. Chen, "A design of 3-dB wideband microstrip power divider with an ultra-wide isolated frequency band," *IEEE Trans. Microw. Theory Techn.*, vol. 64, no. 6, pp. 1806-1811, Jun. 2016.

[2] G. Zhang, X. Wang, J. Hong and J. Yang, "A high-performance dual-mode filtering power divider with simple layout," *IEEE Microw. Wireless Compon. Lett.*, vol. 28, no. 2, pp. 120-122, Feb. 2018.

[3] T. Yu, "Design of length-saving multiway wilkinson power dividers," *IEEE Access*, vol. 6, pp. 14093-14105, 2018.

[4] B. Xia, L. Wu and J. Mao, "An absorptive balanced-to-balanced power divider," *IEEE Access*, vol. 6, pp. 14613-14619, 2018.

[5] H. L. Zhang, B. J. Hu and X. Y. Zhang, "Compact equal and unequal dual-frequency power dividers based on composite right-/left-handed transmission lines," *IEEE Trans. Ind. Electron.*, vol. 59, no. 9, pp. 3464-3472, Sept. 2012.

[6] W. Yu, W. Qin and J. Chen, "Theory and experiment of multiport filtering power divider with arbitrary division ratio based on dielectric resonator," *IEEE Trans. Microw. Theory Techn.*, vol. 66, no. 1, pp. 407-415, Jan. 2019.

[7] W. Fang, E. Chang and Y. Lin, "Bridged-T coil for miniature dual-band branch-line coupler and power divider designs," *IEEE Trans. Microw. Theory Techn.*, vol. 66, no. 2, pp. 889-901, Feb. 2018.

[8] A. Moulay and T. Djerafi, "Wilkinson power divider with fixed width substrate-

integrated waveguide line and a distributed isolation resistance," *IEEE Microw. Wireless Compon. Lett.*, vol. 28, no. 2, pp. 114-116, Feb. 2018.

[9] A. Buesa-Zubiria and J. Esteban, "Design of five-way bagley polygon power dividers in rectangular waveguide," *IEEE Trans. Microw. Theory Techn.*, vol. 66, no. 1, pp. 116-127, Jan. 2018.

[10] H. Chen, W. Che, X. Wang and W. Feng, "Size-reduced planar and nonplanar SIW gysel power divider based on low temperature co-fired ceramic technology," *IEEE Microw. Wireless Compon. Lett.*, vol. 27, no. 12, pp. 1065-1067, Dec. 2017.

[11] T. Yu, J. Tsai and Y. Chang, "A radial four-way power divider with the proposed isolation network," *IEEE Microw. Wireless Compon. Lett.*, vol. 28, no. 3, pp. 194-196, Mar. 2018.

[12] K. Song, Y. Mo, Q. Xue and Y. Fan, "Wideband four-way out-of-phase slotline power dividers," *IEEE Trans. Ind. Electron.*, vol. 61, no. 7, pp. 3598-3606, Jul. 2014.

[13] J. M. Rebollar, J. Esteban and J. E. Page, "Fullwave analysis of three and four-port rectangular waveguide junctions," *IEEE Trans. Microw. Theory Techn.*, vol. 42, no. 2, pp. 256-263, Feb. 1994.

[14] A. San Blas, F. Mira, V. E. Boria, B. Gimeno, M. Bressan and P. Arcioni, "On the fast and rigorous analysis of compensated waveguide junctions using off-centered partial-height metallic posts," *IEEE Trans. Microw. Theory Techn.*, vol. 55, no. 1, pp. 168-175, Jan. 2007.

[15] K. C. Hwang, "Design and optimization of a broadband waveguide magic-T using a stepped conducting cone," *IEEE Microw. Wireless Compon. Lett.*, vol. 19, no. 9, pp. 539-541, Sept. 2009.

[16] Q. Chu, Q. Wu and D. Mo, "A Ka -band E -plane waveguide magic-T with coplanar arms," *IEEE Trans. Microw. Theory Techn.*, vol. 62, no. 11, pp. 2673-2679, Nov. 2014.

[17] L. Guo *et al.*, "A waveguide magic-T with coplanar arms for high-power solid-state power combining," *IEEE Trans. Microw. Theory Techn.*, vol. 65, no. 8, pp. 2942-2952, Aug. 2017.

[18] C. A. Leal-Sevillano, J. A. Ruiz-Cruz, J. R. Montejo-Garai and J. M. Rebollar, "Compact broadband couplers based on the waveguide magic-T junction," *2013 European Microwave Conference*, Nuremberg, 2013, pp. 151-154.

[19] T. Shen, T. Huang, C. Chen and R. Wu, "A laminated waveguide magic-T with bandpass filter response in multilayer LTCC," *IEEE Trans. Microw. Theory Techn.*, vol.

59, no. 3, pp. 584-592, Mar. 2011.

[20] P. Li, H. Chu and R. S. Chen, "SIW magic-T with bandpass response," *Electronics Letters*, vol. 51, no. 14, pp. 1078-1080, 9 7 2015.

[21] X. Gao, W. Feng, W. Che and Q. Xue, "Wideband balanced-to-unbalanced filtering power dividers based on coupled lines," *IEEE Trans. Microw. Theory Techn.*, vol. 65, no. 1, pp. 86-95, Jan. 2017.

[22] K. Xu, J. Shi, L. Lin and J. Chen, "A balanced-to-unbalanced microstrip power divider with filtering function," *IEEE Trans. Microw. Theory Techn.*, vol. 63, no. 8, pp. 2561-2569, Aug. 2015.

[23] W. Zhang, Y. Wu, Y. Liu, F. M. Ghannouchi and A. Hasan, "A wideband balanced-to-unbalanced coupled-line power divider," *IEEE Microw. Wireless Compon. Lett.*, vol. 26, no. 6, pp. 410-412, Jun. 2016.

[24] W. Feng, M. Hong, M. Xun and W. Che, "A novel wideband balanced-to-unbalanced power divider using symmetrical transmission lines," *IEEE Microw. Wireless Compon. Lett.*, vol. 27, no. 4, pp. 338-340, Apr. 2017.

[25] J. Shi, J. Lu, K. Xu and J. Chen, "A coupled-line balanced-to-single-ended out-of-phase power divider with enhanced bandwidth," *IEEE Trans. Microw. Theory Techn.*, vol. 65, no. 2, pp. 459-466, Feb. 2017.

[26] L. Wu, Y. Guo, L. Qiu and J. Mao, "A new balanced-to-single-ended (BTSE) power divider," *2014 IEEE International Wireless Symposium (IWS 2014)*, X'ian, 2014, pp. 1-4.

[27] Y. Wu, Z. Zhuang, L. Jiao and Y. Liu, "A Novel balanced-to-unbalanced complex impedance-transforming in-phase power divider," *IEEE Access*, vol. 5, pp. 16205-16213, 2017.

[28] L. Jiao, Y. Wu, Z. Zhuang, Y. Liu and A. A. Kishk, "Planar balanced-to-unbalanced in-phase power divider with wideband filtering response and ultra-wideband common-mode rejection," *IEEE Trans. on Circuits and Systems I: Regular Papers*, vol. 65, no. 6, pp. 1875-1886, Jun. 2018.

[29] W. Zhang *et al.*, "Planar miniaturized balanced-to-single-ended power divider based on composite left- and right-handed transmission lines," *IEEE Microw. Wireless Compon. Lett.*, vol. 27, no. 3, pp. 242-244, Mar. 2017.

[30] J. Y. Lin, S. W. Wong, Y. Yang, L. Zhu, "Cavity balanced-to-unbalanced magic-T with filtering response," *2019 IEEE MTT-S International Microwave Symposium (IMS)*, Boston, 2019, pp. 1-3.

[31] A. S. Al-Zayed and M. A. Kourah, "The design of an integrated diplexer-power divider based on dual-band impedance transformers and a five-port power-divider," *2017 IEEE AFRICON*, Cape Town, 2017, pp. 630-632.

[32] P. Deng, W. Lo, B. Chen and C. Lin, "Designs of diplexing power dividers," *IEEE Access*, vol. 6, pp. 3872-3881, 2018.

[33] Z. Guo *et al.*, "Triple-mode cavity bandpass filter on doublet with controllable transmission zeros," *IEEE Access*, vol. 5, pp. 6969-6977, 2017.

[34] J.Y. Lin, S.W. Wong, L. Zhu and Q.X. Chu, "Design of miniaturized triplexers via sharing a single triple-mode cavity resonator," *IEEE Trans. Microw. Theory Techn.*, vol. 65, no. 10, pp. 3877-3884, Oct. 2017.

[35] J. Y. Lin, S. W. Wong, Y. M. Wu, Y. Yang, L. Zhu and Y. He, "Three-way multiple-mode cavity filtering crossover for narrowband and broadband applications," *IEEE Trans. Microw. Theory Techn.*, vol. 67, no. 3, pp. 896-905, Mar. 2019.

[36] S.-W. Wong, J.-Y. Lin, Y. Yang, H. Zhu, R.-S. Chen, L. Zhu, and Y. He, “Cavity balanced and unbalanced diplexer based on triple-mode resonator,” *IEEE Trans. Ind. Electron.*, vol. 67, no. 6, pp. 4969-4979, Jun. 2019.

Chapter 3 Single-Band and Dual-Band Filtering Antenna Arrays Based on High-Order Mode Resonators

3.1 Introduction

Antenna arrays with the properties of high gain, wide bandwidth, and low side-lobe level are highly demanded in today's wireless communication systems. Conventionally, an antenna array consists of a feeding network and radiation elements. Source signals go through the feed lines and power dividing network before arriving at the radiation elements [1]-[6]. When the number of radiation elements is large, the required feeding network will be complicated and challenging to achieve. Apart from this, a bulky feeding network often causes high insertion loss and introduces design complexity.

To tackle this challenge, the elimination of a feeding network by using high-order modes has attracted much attention [7]-[9]. A 3 × 3 slotted antenna array based on TE_{330} high-order mode is firstly presented in [7] with an impedance bandwidth of 26% and a maximum gain of 13.8 dBi at the millimeter-wave band. TE_{440} high-order mode is adopted in [8] to support 16 radiation slots by achieving a single-feed circularly polarized cavity antenna. In [9], the feeding network and high-order mode are combined to implement 20 × 24 and 40 × 48 antenna arrays using TE_{560} high-order mode. In these studies, well-functioning high radiation gain and low side-lobe levels are achieved. However, the unwanted high-order mode resonances may affect radiation performance, which needs to be suppressed to retain the purity of the desired resonance mode.

As a practical solution, the filtering function can be integrated into the antenna array to eliminate the unwanted high-order modes. A pair of high-order modes, TM_{230} and TM_{320}, are used to realize the high-Q cavity filter in [10]. As implemented in the printed circuit board (PCB) [11]-[13] and slotted waveguide techniques [14]-[16], filtering antenna arrays have the advantages of high selectivity, compact size, low-loss, and high gain. For conventional filtering antenna array designs [11]-[16], a feeding network formed by power dividers is essential, which usually consists of resonators. The last-stage resonator serves as not only a resonant element but also an antenna unit. This method helps to integrate the filtering function into the feeding network. However, it is challenging to apply this to a cavity array with a large number of radiation elements, for example the designs described in [15]-[16]. According to the open literature, filtering cavity array antennas with more than 16 elements is difficult to achieve.

In our previous studies, the fundamental modes of the multimode cavity resonators were investigated in designing filters [17]-[18], multiplexers [19]-[20], and functional microwave circuits [21]-[22]. Compared with high-order modes, the fundamental mode is a better candidate in designing compact microwave components. However, when designing an antenna array using the fundamental mode cavity resonators, the feeding and power dividing network are essential [15]-[16]. A high-order mode resonator is more suitable for cavity slot array design because the radiation elements of a single high-order mode cavity resonator can produce in-phase outputs with the same amplitude. For this reason the power splitting network is not required.

In this paper, a series of filtering cavity slot arrays are proposed based on high-order mode resonators. The cavity resonator, excited in a high-order mode, serves as a key component generating filtering response. Each loop of the magnetic field inside the cavity is opened by a slot, which acts the radiation element of the array. Therefore, a cavity slot array antenna can be realized by a single cavity resonator operating at the high-order mode. For example, a single cavity resonator, operating at TM_{450} mode, can form a 4 × 5 cavity-slot array. Furthermore, it emerges that the unloaded quality factor (Q_u) is higher when operating at high-order mode, which results in a smaller fractional bandwidth (FBW) and a higher radiation gain. A cavity slot array with a large number of elements can be easily realized, taking advantage of the high-order mode of a single cavity resonator.

Section 3.2 briefly discusses the high-order mode cavity resonators, including their characteristics and compares their performance. Based on the high-order mode theory, section 3.3 presents the design of a single-band filtering antenna array using TM_{450} mode. Furthermore, a dual-band dual-polarized filtering cavity slot array antenna using a pair of high-order modes TM_{340} and TM_{430} is presented in section 3.4.

3.2 Concept of Resonant Modes

Fig. 3.1(a) depicts the geometrical configuration of a standard rectangular cavity, whose length, width, and height are denoted as a, b and c, respectively. The resonant frequencies of the proposed rectangular waveguide modes can be expressed as:

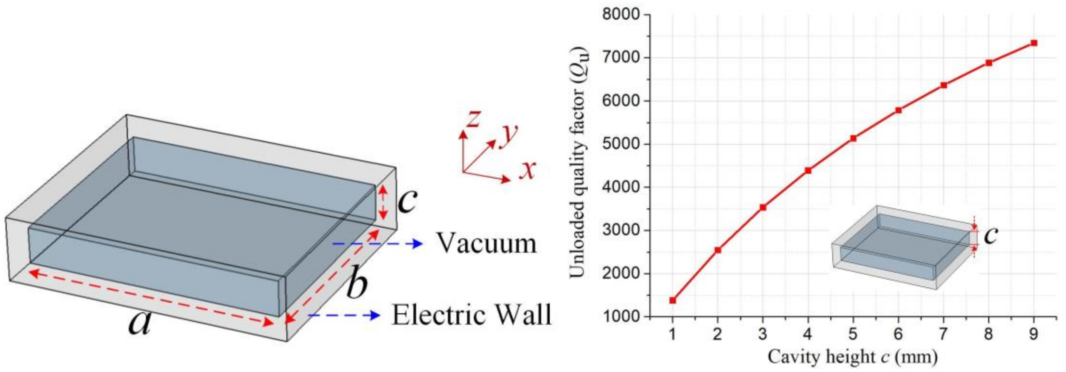

(a) (b)

Fig. 3.1. (a) Geometry of TM_{mn0}-type rectangular cavity resonator (c<< a and b). (b) Extracted Q_u value versus cavity height c based on 10 GHz TM_{110} resonator.

$$\omega_{m,n,l}{}^{2} = \frac{v^2}{\varepsilon_r u_r}\left[\left(\frac{m\pi}{a}\right)^2+\left(\frac{n\pi}{b}\right)^2+\left(\frac{l\pi}{c}\right)^2\right] \tag{3-1}$$

where $\omega_{m,n,l}$ stands for the resonant angular frequencies of the specific modes (m, n, and l = 0 or 1), while v stands for the speed of light in the vacuum. ε_r and u_r are the permittivity and permeability of the air in the cavity, respectively.

When height c of the proposed cavity is reduced to satisfy the condition: $c << a$ and b, it means that the frequencies of resonating modes controlled by c become higher. According to formula (1), only one kind of resonant mode remains unchanged, which is defined as TM_{mn0}-type modes. Regarding the TM_{mn0} modes, the length a and width b of the rectangular cavity serve to control the resonant frequency of the proposed modes, while the height c is a parameter which controls the value of Q_u of the cavity resonator [23]. The relationship between Q_u and height c, based on TM_{110} mode resonator at 10 GHz, is plotted in Fig. 3.1(b). When height c decreases, the achieved Q_u gradually wanes, resulting in a wider bandwidth.

For TM_{mn0} modes, TM_{110} is the fundamental one at the lowest resonant frequency. However, it only possesses one magnetic-field loop. High-order modes have more magnetic-field loops as shown in Fig. 3.2. Each of the magnetic-field loops is in-phase with the same amplitude, which plays a key role in designing antenna arrays.

To achieve the pure boresight radiation pattern with low side-lobe level, it is better for the feeding port to be placed at the geometry center of the cavity surface, while the

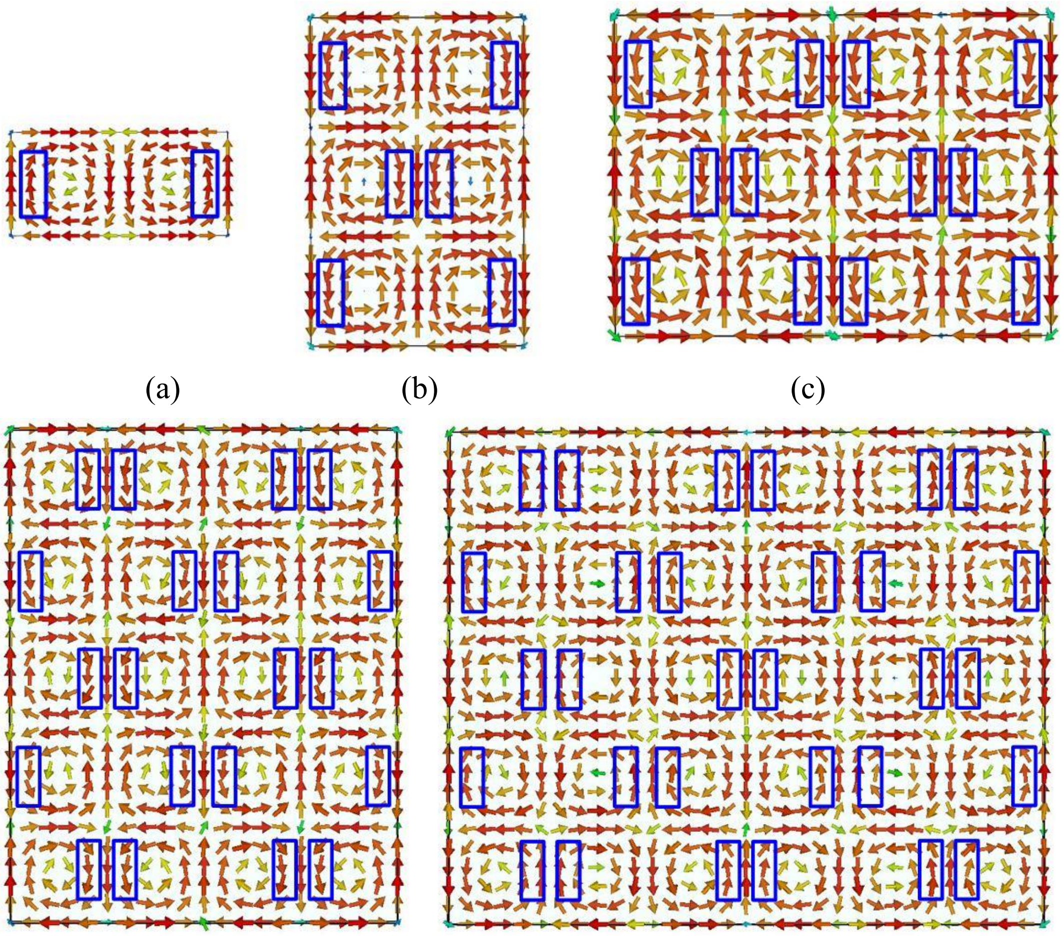

(a) (b) (c)

(d) (e)

Fig. 3.2. Magnetic field distributions of higher-order modes with slot etched (denoted as blue rectangle) in the TM$_{mn0}$-type resonator. (a) TM$_{210}$, (b) TM$_{230}$, (c) TM$_{430}$, (d) TM$_{450}$, (e) TM$_{650}$.

radiating elements on the radiation surface should be symmetrical. Furthermore, the numbers of columns m and rows n of proposed antenna arrays should be close to each other so that the x-axis side-lobe level is similar to that of the y-axis. However, when TM$_{mn0}$ ($m = n$ =2, 3, 4, ……) is considered, the radiating units on the radiation surface are asymmetrical to the x-axis and y-axis, which results in the offset radiation patterns [7]. Given this, a series of TM$_{mn0}$ ($m = n$-1, n = 2, 3, 4……) modes are adopted in the proposed filtering antenna arrays for discussions. Fig. 3.2 presents magnetic field distributions of some high-order modes with etched slots, for the scenarios of TM$_{210}$, TM$_{230}$, TM$_{430}$, TM$_{450}$, and TM$_{650}$ modes. It can be seen that each magnetic field loop requires one slot to excite the radiation for that unit. Therefore, a cavity resonator operating at TM$_{mn0}$ mode requires m × n slots to form the array.

To integrate the filtering and radiating functions, several crucial performance indices based on these adopted resonating modes are discussed in Table 3.1. When 10 GHz frequency is considered, the length a and width b of fundamental mode TM$_{110}$ resonator are 21 mm and 21 mm, respectively. The size of TM$_{mn0}$ mode cavity is $m \times n$ times the size of TM$_{110}$ mode. On the radiation side, the radiating slots have to be properly allocated at the positions, where the magnetic fields of the loops are in-phase with same-amplitude. Fig. 3.2 depicts the etched slot distributions corresponding to the magnetic field loops of the high-order modes.

TABLE 3.1
Specifications Among Different High-Order Modes at 10 GHz.
(5mm Cavity Height).

	Size (a×b mm^2)	Radiating Units	Q_u-value	Spurious-mode Ratio	Stopband Range	Gain (dBi)
TM$_{210}$	21 × 42	2	5548.9	- / TM$_{410}$ (1.6f_0)	- / 0.6f_0	10.1
TM$_{230}$	42 × 63	6	6202.9	TM$_{210}$ (0.75f_0) / TM$_{250}$ (1.39f_0)	0.25f_0 / 0.39f_0	13.9
TM$_{430}$	63 × 84	12	6405.1	TM$_{230}$ (0.8f_0) / TM$_{630}$ (1.29f_0)	0.2f_0 / 0.29f_0	16.7
TM$_{450}$	84 × 105	20	6605.3	TM$_{430}$ (0.83f_0) / TM$_{470}$ (1.23f_0)	0.17f_0 / 0.23f_0	19.5
TM$_{650}$	105 × 126	30	6692.7	TM$_{450}$ (0.86f_0) / TM$_{850}$ (1.19f_0)	0.14f_0 / 0.19f_0	20.4

f_0 means resonating frequency of proposed mode.

Table 3.1 shows the specifications of different high-order modes at 10 GHz. It is apparent that the more units the array has, the higher gain the array can achieve. In Table 3.1, TM$_{210}$ achieves the lowest gain of 10.3 dBi using 2 radiating units, while TM$_{650}$ achieves the highest gain of 20.4 dBi using 30 radiating units. Regarding filtering performance, when the resonant mode is getting higher, the value of Q_u is getting bigger. Since the cavity resonator is a type of high-Q resonator, it tends to show a narrow-band performance. The higher Q_u of resonating modes results in a narrower frequency bandwidth. The stopband range is also a crucial index to perform a filtering function. As summarized in Table I, when the mode is higher, the spurious mode ratio becomes

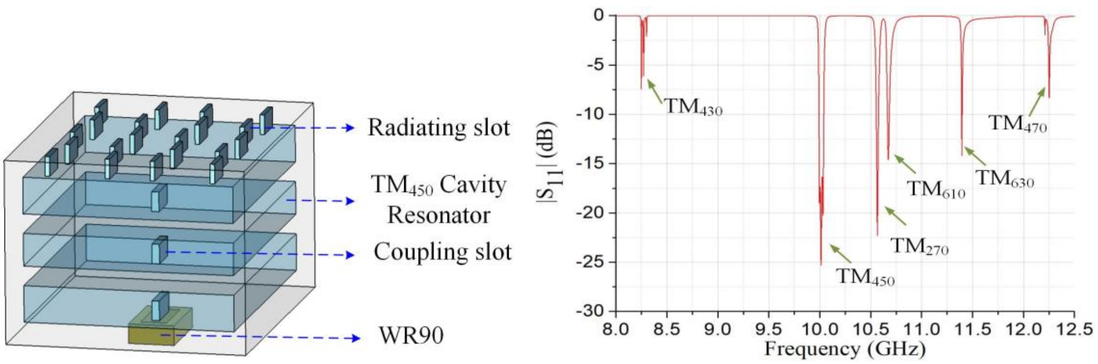

(a) (b)

Fig. 3.3. Initial design of 3rd-order filtering antenna array using TM_{450} mode cavity resonator: (a) Geometrical configuration, (b) Simulated S-parameters.

smaller, and the stopband range is getting narrower.

3.3 3rd-Order Filtering Antenna Array Using TM_{450} Mode

The initial geometrical configuration of a 3rd-order filtering antenna array is shown in Fig. 3.3(a). It is based on a TM_{450} mode cavity resonator with 4 × 5 radiating units. The electromagnetic (EM) waves are coupled from WR-90 to three consecutive TM_{450} mode resonators and radiate at the end of the slot arrays. For the specified resonant frequency of 10 GHz, the length a_1 and width b_1 of the TM_{450} mode cavity resonator are 84 mm and 105 mm, respectively.

The simulated S-parameter of the proposed structure is given in Fig. 3.3(b). It can be seen that the expected band resonates at 10 GHz with a bandwidth of 60 MHz. At the lower stopband, the closest spurious mode is TM_{430}, which is located at 8.25 GHz. However, the nearest spurious mode, at the upper band, is TM_{270}, which is located at 10.56 GHz. Then the next spurious modes are TM_{610}, TM_{630}, and TM_{470}, respectively. To eliminate the unwanted high-order modes around TM_{450}, an improved coupling method is devised to suppress a series of spurious modes to enlarge the stopband range.

The improved version of the geometrical structure is shown in Fig. 3.4. Compared with the previous version, as indicated in Fig. 3.3(a) where coupling slots are placed at the surface center of the cavity resonator, a pair of coupling slots with a distance of λ_0

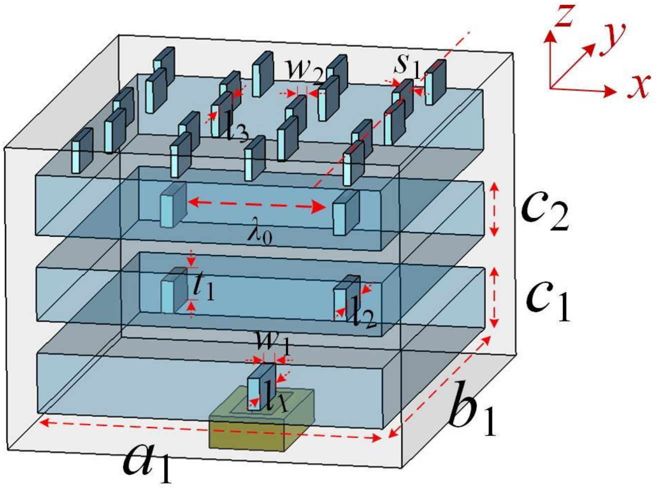

Fig. 3.4. Improved geometrical configuration of 3rd-order filtering antenna array using a TM_{450} mode cavity resonator.

are placed along the x-axis of the cavity resonator surface, as shown in Fig. 3.4.

Considering the specification of a center frequency of 10 GHz, FBW of 0.6%, and ripple level of 0.2 dB, the formulas of external quality factors Q_e and coupling coefficients K of 3rd-order Chebyshev response are depicted as:

$$Q_e = \frac{g_0 g_1}{FBW} \tag{3-2a}$$

$$K_{12} = K_{23} = \frac{FBW}{\sqrt{g_1 g_2}} \tag{3-2b}$$

where g_0, g_1, g_2, and g_3 are the low-pass prototype element values of filter synthesis, which can be set as $g_0 = g_4 = 1$, $g_1 = g_3 = 1.5963$, and $g_2 = 1.0967$ [24]. After substituting the chosen values, the calculated external quality factor and coupling coefficient are $Q_e = 266.05$, and $K_{12} = K_{23} = 0.04$, respectively.

The values of Q_e and K of the proposed design can be obtained from the filter extraction in EM simulation. In the improved geometrical configuration of Fig. 3.4, the slot with a length of l_1 and a width of w_1 are used to control Q_e from the feeding to the structure, while the slots with a length of l_3 and a width of w_2, and an offset of s_1 are used to control Q_e from vacuum to structure. The Q_e value can be obtained using

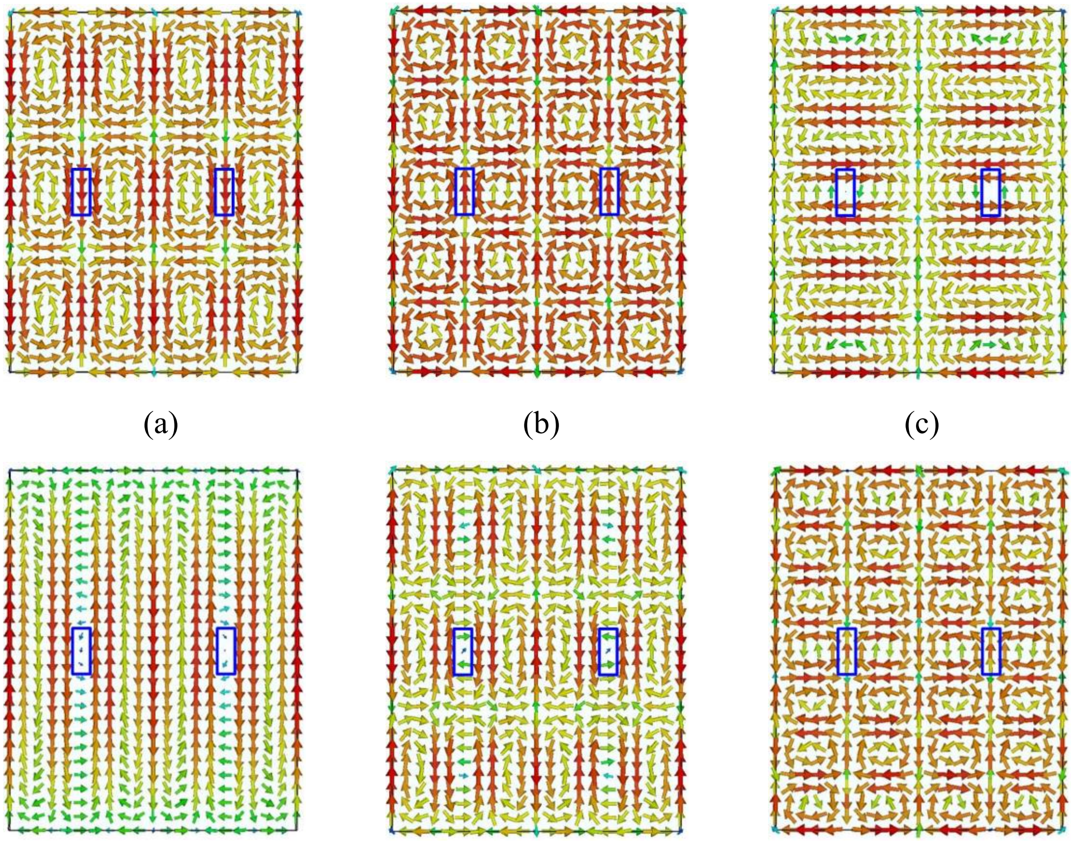
(a) (b) (c)

(d) (e) (f)

Fig. 3.5. H-field distributions of the resonant modes: (a) TM_{430}, (b) TM_{450}, (c) TM_{270}, (d) TM_{610}, (e) TM_{630}, (f) TM_{470}.

following calculation [25]:

$$Q_e = \frac{2\pi f_0 \tau_{s11}(f_0)}{4} \tag{3-3}$$

where $\tau_{s11}(f_0)$ represents the group delay at the resonance. Meanwhile, the coupling coefficient K between cavity resonators is controlled by a length of l_2. The K value can be obtained using the following equation [25]:

$$K = \frac{f_{p2}^2 - f_{p1}^2}{f_{p2}^2 + f_{p1}^2} \tag{3-4}$$

where f_0, f_{p1}, and f_{p2} represent the two resonant peaks. It is noted that the slotted array also serves the third resonator in the filter network. The input Q_e value from WR-90, Q_{ein}, should have the same value as the radiation Q_e value, namely Q_{erad}.

To suppress the unwanted spurious modes for an improved stopband range, it is essential to analyze the resonant modes' field distributions. Table 3.2 lists a series of resonant modes located from 8.3 GHz to 12.3 GHz. Since the waveguide port is adopted as the feeding structure in this design, several resonant modes are degraded and prohibited to pass through, which are labeled as ‘feed suppressed’ in Table 3.2.

TABLE 3.2
RESONANT MODES FROM 8.3 GHZ TO 12.3 GHZ

Modes	Frequency (GHz)	Suppression Method
TM_{160}	8.75	Feed suppressed
TM_{350}	8.93	Feed suppressed
TM_{510}	9.04	Feed suppressed
TM_{440}	9.14	Feed suppressed
TM_{260}	9.28	Feed suppressed
TM_{520}	9.37	Feed suppressed
TM_{530}	9.90	Feed suppressed
TM_{450}	10.10	N.A.
TM_{360}	10.11	Feed suppressed
TM_{170}	10.16	Feed suppressed
TM_{540}	10.60	Feed suppressed
TM_{270}	10.62	Coupling suppressed
TM_{610}	10.81	Coupling suppressed
TM_{620}	11.09	Feed suppressed
TM_{460}	11.16	Feed suppressed
TM_{370}	11.35	Feed suppressed
TM_{550}	11.44	Feed suppressed
TM_{630}	11.54	Coupling suppressed
TM_{180}	11.57	Feed suppressed
TM_{280}	11.98	Feed suppressed
TM_{640}	12.15	Feed suppressed

For other modes passing through waveguide feeding, the H-field distributions are shown in Fig. 3.5. TM_{450} mode is expected to remain while the others should be suppressed. If the coupling slot is placed at the surface-center of the cavity resonator, as presented in Fig. 3.3(a), all of these modes can pass through since H-field directions of these modes correspond to the long-side of the coupling slot. However, when a pair of slots with a distance of λ_0 are placed along the x-axis as depicted in blue circles in Fig. 3.5, it is evident that the H-field directions of TM_{270}, TM_{610}, and TM_{630} modes are

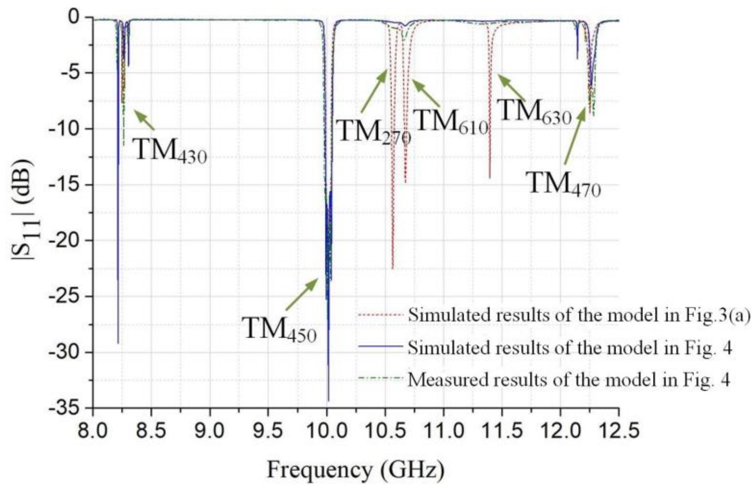

Fig. 3.6. Simulated S-parameters of the models in Fig. 3(a) and Fig. 4, and the measured results of the model in Fig. 4 (fabricated prototype shown in Fig. 7(a)).

opposite in the coupling slots, so that H-field energy density should be null. Consequently, these three modes would be prohibited from passing through. For TM_{430}, TM_{450}, and TM_{470} modes, they can still transmit through the structure using the proposed coupling method. At this point, TM_{270}, TM_{610}, and TM_{630} modes are suppressed by the coupling method and labeled as ‘coupling suppressed’ in Table 3.2.

Fig. 3.6 presents the S-parameter comparison among the initial version of the model in Fig. 3.3(a), the improved version of the model in Fig. 3.4, and the measured results of the prototype. It can be seen that, for the measured prototype, TM_{450} mode resonates at 10 GHz, while TM_{430} and TM_{470} modes resonate at 8.3 GHz and 12.3 GHz, respectively. However, TM_{270}, TM_{610}, and TM_{630} modes have been significantly suppressed using the model presented in Fig. 3.4.

Fig. 3.7(a) is a photograph of the fabricated filtering antenna array prototype using several brass layers assembled together. A standard WR-90 waveguide is used to feed the structure. The measured S_{11} and realized gain of the prototype are shown in Fig. 3.7(b), along with the corresponding simulation results. It has three reflection poles with a return loss level of 15 dB, indicating a 3rd-order filtering response. The prototype resonates at 10 GHz, and the 10-dB bandwidth ranges from 9.97 GHz to 10.03 GHz. The measured average gain within the passband can achieve 19.5 dBi, and the achieved radiation efficiency is 90% within the band. As shown in Figs. 3.7(c) and (d), the side-

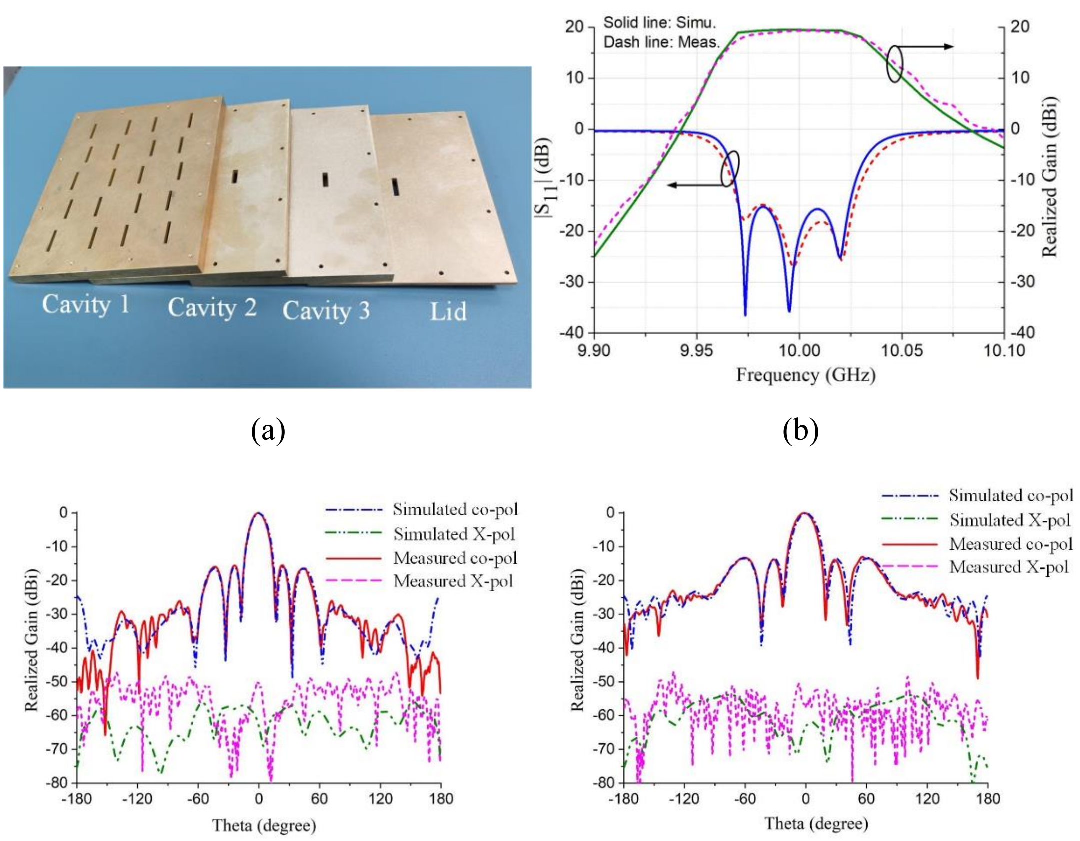

(a) (b)

(c) (d)

Fig. 3.7. 3rd-order filtering antenna array using TM_{450} mode with: (a) Photograph of manufactured prototype – model shown in Fig. 4, (b) Measured S-parameter and realized gain, (c) E-plane and (d) H-plane radiation patterns at 10 GHz.

lobe suppressions are -15.6 dB and -13.3 dB at E-plane and H-plane, respectively, while the cross-polarization levels are -53.4 dB and -56.3 dB at E-plane and H-plane, respectively. The measured 3 dB beamwidth is 15 degrees at E-plane and 18 degrees at H-plane. The measured radiation patterns agree well with the simulated ones. The physical dimensions of the proposed prototype are tabulated in Table 3.3.

TABLE 3.3
PHYSICAL DIMENSIONS OF THE FILTERING ANTENNA ARRAY USING TM_{450} CAVITY RESONATOR (all in mm)

$a_1 = 84$	$b_1 = 105$	$c_1 = 5$	$S_1 = 1.5$	$l_1 = 13.4$
$w_1 = 3$	$w_2 = 1.8$	$l_2 = 10.8$	$l_3 = 13.6$	$t_1 = 3$

3.4 3rd-Order Dual-Band Filtering Antenna Array Using TM$_{430}$ and TM$_{340}$ Modes

Based on the design methodology discussed above, a dual-band filtering cavity antenna array can be achieved using a pair of degenerated modes, i.e., TM$_{mn0}$ and TM$_{nm0}$ ($m \neq n$, and m, n = 1, 2, 3⋯⋯), which always remain in the high-order mode cavity resonators. In this section, a pair of degenerated high-order modes, TM$_{430}$ and TM$_{340}$, are adopted to design a dual-band dual-polarized filtering antenna array with 3 × 4 radiating units.

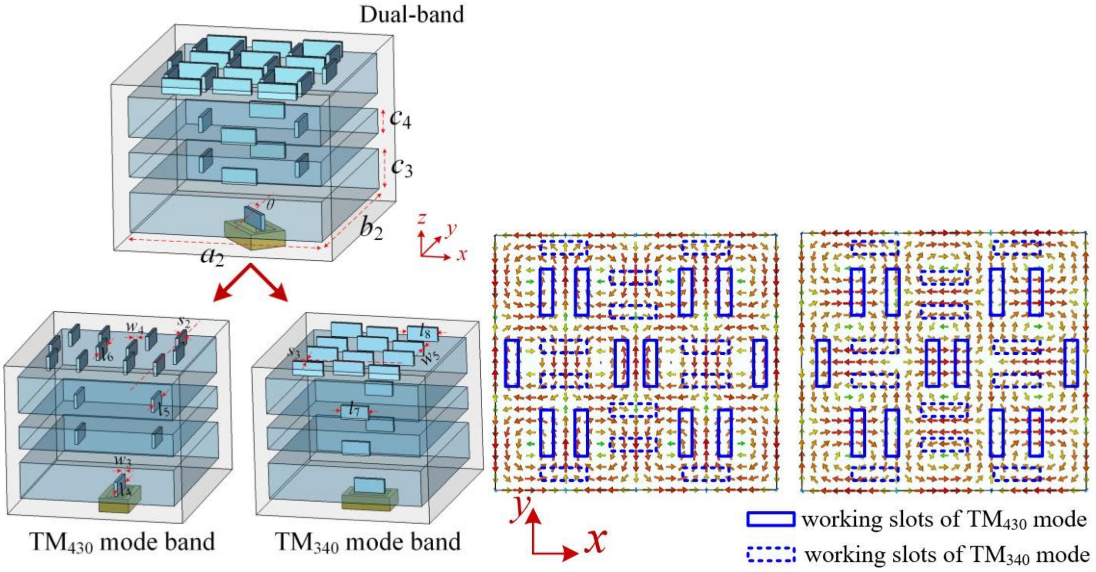

(a) (b)

Fig. 3.8. 3rd-order dual-band dual-polarized filtering antenna array using TM$_{430}$ and TM$_{340}$ mode cavity resonators with: (a) Geometrical configuration, (b) H-field and radiating slot distributions.

Fig. 3.8 presents the geometrical configuration of the proposed 3rd-order array prototype. It comprises three dual-mode cavity resonators, each being shared by TM$_{430}$ and TM$_{340}$ modes. The WR-90 waveguide is rotated at an angle of θ to excite these two modes. In order to understand this better, the proposed dual-band structure can be divided into two individual parts geometrically: TM$_{430}$ mode band part and TM$_{340}$ mode band part, as shown in Fig. 3.8(a). Each of these two bands is dominated by relevant mode and not affected by the other. Therefore, when rotated angle $\theta = 0°$, as depicted in the right-hand side bottom of Fig. 3.8(a), only the coupling slots and radiating slots with their long-side direction parallel to *x*-axis work, it forms a TM$_{340}$ mode single-

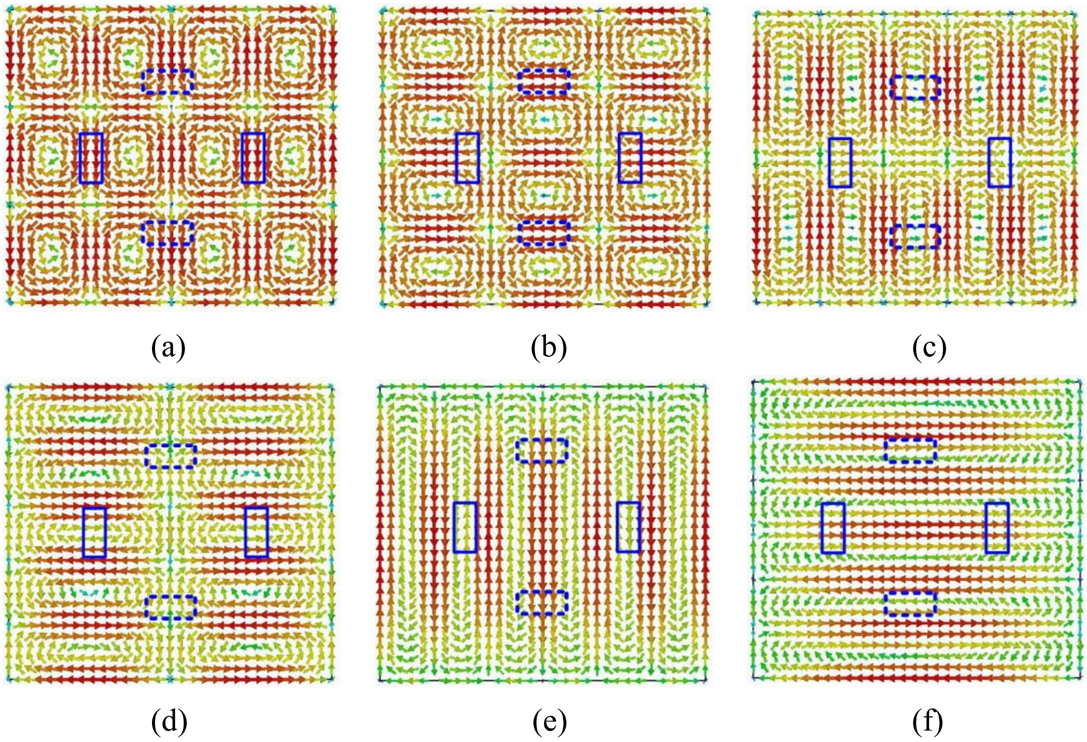
(a) (b) (c)

(d) (e) (f)

Fig. 3.9. H-field distributions of modes with: (a) TM_{430}, (b) TM_{340}, (c) TM_{520}, (d) TM_{250}, (e) TM_{610}, (f) TM_{160}. (slots with solid line for TM_{430}, slots with dotted line for TM_{340}.)

band filtering array performance. Similarly, when rotated angle $\theta = 90°$, as depicted in the left-hand side bottom of Fig. 3.8(a), TM_{430} mode single-band filtering array performance forms up. Therefore, the rotated angle θ becomes a key parameter to allocate Q_e of the proposed two bands.

In the dual-band prototype design, it is crucial to ensure that the parameters working on one band have little effect on the other so that both bands in the design can be individually controlled. For this reason, radiating slots of each band should be allocated at the maximum H-field energy density of the proposed mode and minimum H-field energy density of the other mode. As H-field distributions of two modes presented in Fig. 3.8(b), the slots with their long-side direction parallel to the y-axis are the working slots of TM_{430} mode, which are denoted as the solid blue line. These 4 × 3 radiating slots should be allocated at the null H-field energy density of TM_{340} mode. As shown in the right-hand side of Fig. 3.8(b), there are three null H-field density rows in TM_{340} field distribution, which corresponds to the number of rows in the 4 × 3 array. Similarly, the working slots of TM_{340} mode, denoted as a dotted line, are placed at the null H-field density of TM_{430} mode distribution. In this way, two bands of the proposed prototype can be independently controlled at radiation layers with individual Q_{erad}, respectively.

Considering the specification of a center frequency of 9.87 GHz and 10.13 GHz, FBW of 0.6% and 0.8%, and ripple level of 0.2 dB, respectively, according to the related equations 2(a)-(b), the external quality factors Q_e and coupling coefficients K of 3rd-order Chebyshev response in the first and the second channels can be deduced as Q_e^{I}=266.05, K_{12}^{I}=K_{23}^{I}=0.04, and Q_e^{II}=199.54, K_{12}^{II}=K_{23}^{II}=0.06, respectively.

Similar to the analysis above, to suppress the unwanted spurious modes for an enlarged stopband range, it is essential to analyze the field distributions of resonant modes. Table 3.4 lists a series of resonant modes from 8 GHz to 13.1 GHz. WR-90 is adopted as the feeding structure and to suppress several harmonic modes, which are labeled as 'feed suppressed' in Table 3.4.

TABLE 3.4

RESONANT MODES FROM 8 GHZ TO 13.1 GHZ

Modes	Frequency (GHz)	Suppression Method
TM_{330}	8.58	Feed suppressed
TM_{420}	8.77	Feed suppressed
TM_{240}	9.31	Feed suppressed
TM_{510}	9.83	Feed suppressed
TM_{430}	9.97	N.A.
TM_{340}	10.25	N.A.
TM_{520}	10.50	Coupling suppressed
TM_{150}	10.77	Feed suppressed
TM_{250}	11.27	Coupling suppressed
TM_{440}	11.44	Feed suppressed
TM_{530}	11.52	Feed suppressed
TM_{610}	11.72	Coupling suppressed
TM_{350}	12.06	Feed suppressed
TM_{620}	12.28	Feed suppressed
TM_{160}	12.86	Coupling suppressed

For other modes passing through WR-90, the coupling method is employed again in this design. Two pairs of coupling slots are placed along the x-axis and y-axis, respectively, as depicted in the blue circles appearing in Fig. 3.9. Thus, the H-field directions of two pairs of harmonic modes - TM_{250} and TM_{520}, TM_{610} and TM_{160} - are opposite in the coupling slots so that H-field energy density should be null. Based on this, these modes are filtered out. The nearest spurious modes are TM_{230}/TM_{320} modes at the lower stopband and TM_{630}/TM_{360} modes at the upper stopband.

Fig. 3.10(a) is a photograph of the manufactured filtering antenna array prototype using several brass layers assembled together. The measured S_{11} and realized gains of the prototype are shown in Fig. 3.10(b), along with the corresponding simulation. It has three reflection poles with a return loss level of 15 dB in each channel of dual-band

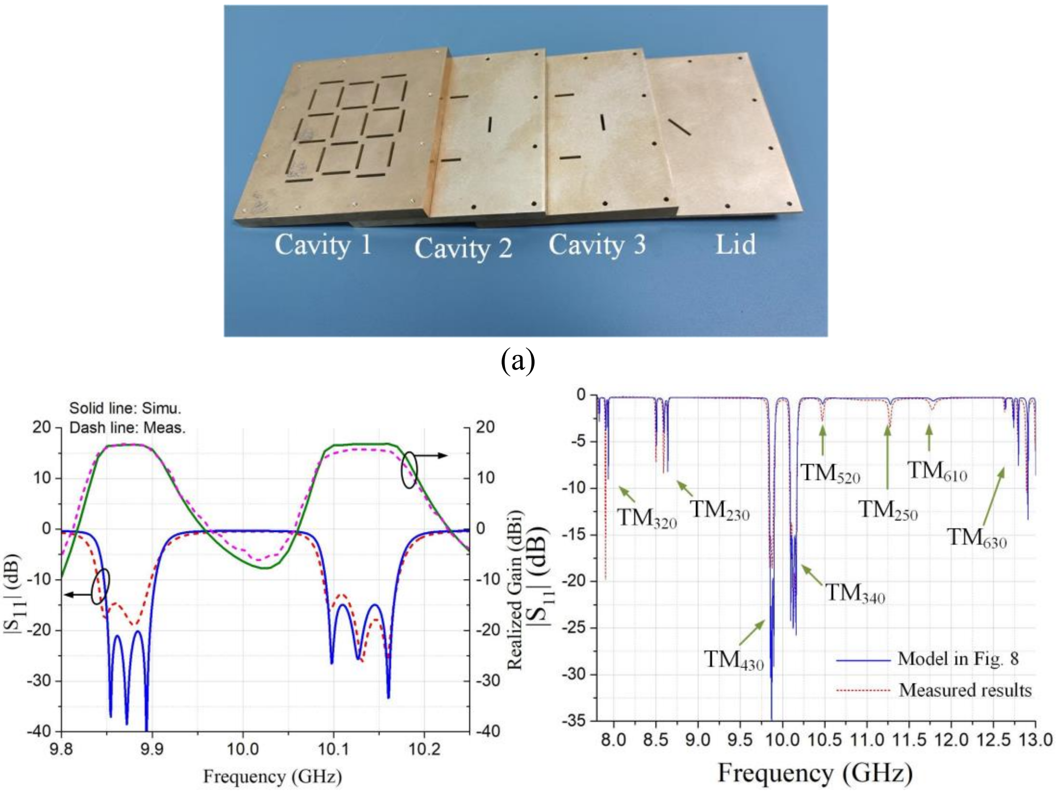

(b) (c)

Fig. 10. 3rd-order dual-band dual-polarized filtering antenna array with: (a) Photograph of manufactured prototype, (b) Simulated and measured S-parameter results and realized gain, (c) S-parameter results in a wide range.

prototype, indicating a 3rd-order filtering response. The prototype resonates at 9.87 GHz, 10.13 GHz, and the 10-dB bandwidth ranges from 9.84 GHz to 9.9 GHz, and 10.09 GHz to 10.17 GHz, respectively. The measured average gain in the first and second channels can achieve, respectively, 16.7 dBi and 15.8 dBi. The achieved radiation efficiency is 90% in the lower band and 85% in the upper band. As shown in Figs. 3.11(a) and (b), the side-lobe suppressions in the first channel are -14.1 dB and -16.4 dB at both E-plane and H-plane, respectively, while the cross-polarization levels are -53.6 dB and -48.4 dB at E-plane and H-plane, respectively. The measured 3 dB beamwidth is 29 degrees at E-plane and 20 degrees at H-plane. As shown in Figs. 3.11(c) and (d), the side-lobe suppressions in the second channel are -14.4 dB and -26.7 dB at both E-plane and H-plane, respectively, while the cross-polarization levels are -36.9 dB and -36.6 dB at E-plane and H-plane, respectively. The measured 3 dB beamwidth is 29 degrees at E-plane and 23 degrees at H-plane. The measured radiation patterns are in good agreement with the simulated ones.

The physical dimensions of the proposed prototype are documented in Table 3.5.

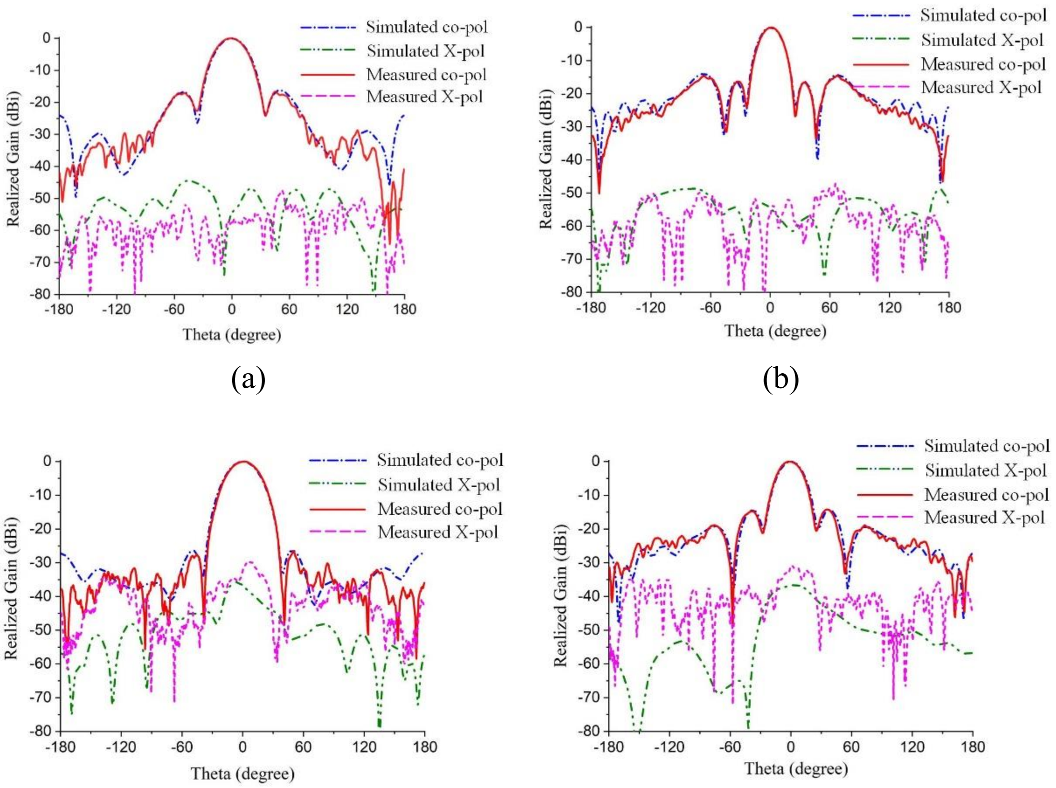

(a) (b)

(c) (d)

Fig. 3.11. (a) E-plane and (b) H-plane pattern results at 9.87 GHz frequency. (c) E-plane and (d) H-plane pattern results at 10.13 GHz frequency.

TABLE 3.5
PHYSICAL DIMENSIONS OF THE FILTERING ANTENNA ARRAY USING TM430 AND TM340 CAVITY RESONATOR (UNIT: mm)

$a_2 = 70.8$	$b_2 = 78$	$c_3 = 5$	$S_2 = 1$
$S_3 = 1.35$	$\theta = 41$	$w_3 = 1.5$	$w_4 = 1.5$
$w_5 = 1.5$	$l_4 = 14.1$	$l_5 = 10.1$	$l_6 = 14$
$l_7 = 10.2$	$l_8 = 14.2$		

3.5 Conclusion

In this chapter, a series of filtering cavity slot array antennas are proposed to take advantage of high-order mode cavity resonators. The characteristics and performance of high-order modes, inside a single cavity, are summarized and presented. The greater the thickness, the higher the achieved Q_u value of TM mode resonator. For validation, two design examples are presented. The first design is a single-band filtering cavity slot array using a TM450 mode resonator with a realized gain of 19.5 dBi. The second design is a dual-band dual-polarized filtering cavity slot array using a TM430 and TM340 mode resonator with realized respective gains of 16.7 dBi and 15.8 dBi. The two designs are fabricated and measured. The results of measurements and simulations are well matched, which helps to verify our predicted design methodology. Compared with the waveguide array using the fundamental mode, the advantages of the proposed array adopting the high-order mode are reduced design complexity, ease in implementing a large number of array elements, and can easily achieve high-order dual-band dual-polarized performance.

3.6 References

[1] E. Levine, G. Malamud, S. Shtrikman, and D. Treves, “A study of microstrip array antennas with the feed network,” *IEEE Trans. Antennas Propag.*, vol. 37, no. 4, pp. 426–434, Apr. 1989.

[2] S. S. Oh, J. W. Lee, M. S. Song, and Y. S. Kim, “Two-layer slottedwaveguide antenna array with broad reflection/gain bandwidth at millimetre-wave frequencies,” *IEE Proc.-Microw. Antennas Propag.*, vol. 51, no. 5, pp. 393–398, Oct. 2004.

[3] S. Park, Y. Tsunemitsu, J. Hirokawa, and M. Ando, “Center feed single layer slotted waveguide array,” *IEEE Trans. Antennas Propag.*, vol. 54, no. 5, pp. 1474–1480, May 2006.

[4] Y. Miura, J. Hirokawa, M. Ando, Y. Shibuya and G. Yoshida, "Double-layer full-corporate-feed hollow-waveguide slot array antenna in the 60-GHz band," *IEEE Trans. Antennas Propag.*, vol. 59, no. 8, pp. 2844-2851, Aug. 2011.

[5] J. Xu, Z. N. Chen, X. Qing and W. Hong, "140-GHz TE20-mode dielectric-loaded SIW slot antenna array in LTCC," *IEEE Trans. Antennas Propag.*, vol. 61, no. 4, pp. 1784-1793, Apr. 2013.

[6] D. Kim, J. Hirokawa, M. Ando, J. Takeuchi and A. Hirata, "64 × 64-element and 32 × 32-element slot array antennas using double-layer hollow-waveguide corporate-feed in the 120 GHz band," *IEEE Trans. Antennas Propag.*, vol. 62, no. 3, pp. 1507-1512, Mar. 2014.

[7] W. Han, F. Yang, J. Ouyang and P. Yang, "Low-cost wideband and high-gain slotted cavity antenna using high-order modes for millimeter-wave application," *IEEE Trans. Antennas Propag.*, vol. 63, no. 11, pp. 4624-4631, Nov. 2015.

[8] W. Han, F. Yang, R. Long, L. Zhou and F. Yan, "Single-fed low-profile high-gain circularly polarized slotted cavity antenna using a high-order mode," *IEEE Antennas and Wireless Propag. Lett.*, vol. 15, pp. 110-113, 2016.

[9] Q. Yuan, Z. Hao, K. Fan and G. Q. Luo, "A compact *W*-band substrate-integrated cavity array antenna using high-order resonating modes," *IEEE Trans. Antennas Propag.*, vol. 66, no. 12, pp. 7400-7405, Dec. 2018.

[10] C. Lin and S. Chung, "A Filtering microstrip antenna array," *IEEE Trans. Microw. Theory Techn.*, vol. 59, no. 11, pp. 2856-2863, Nov. 2011.

[11] S. Bastioli, R. V. Snyder and C. Tomassoni, "Over-moded transverse magnetic cavity filters for narrowband millimeter-wave applications," *IEEE Microw. and Wireless Comp. Lett.*, vol. 29, no. 5, pp. 321-323, May 2019.

[12] H. Chu, J.-X. Chen, S. Luo, and Y.-X. Guo, “A millimeter-wave filtering monopulse antenna array based on substrate integrated waveguide technology,” *IEEE Trans. Antennas Propag.*, vol. 64, no. 1, pp. 316–321, Jan. 2016.

[13] C. Mao et al., "An integrated filtering antenna array with high selectivity and harmonics suppression," *IEEE Trans.Microw. Theory Techn.*, vol. 64, no. 6, pp. 1798-1805, Jun. 2016.

[14] X. Xu, M. Zhang, J. Hirokawa and M. Ando, "E-band plate-laminated waveguide filters and their integration into a corporate-feed slot array antenna with diffusion bonding technology," *IEEE Trans. Microw. Theory Techn.*, vol. 64, no. 11, pp. 3592-3603, Nov. 2016.

[15] R. H. Mahmud and M. J. Lancaster, "High-gain and wide-bandwidth filtering planar antenna array-based solely on resonators," *IEEE Trans. Antennas Propag.*, vol. 65, no. 5, pp. 2367-2375, May 2017.

[16] F. Chen, J. Chen, Q. Chu and M. J. Lancaster, "X-band waveguide filtering antenna array with nonuniform feed structure," *IEEE Trans. Microw. Theory Techn.*, vol. 65, no. 12, pp. 4843-4850, Dec. 2017.

[17] S. Wong, S. Feng, L. Zhu and Q. Chu, "Triple- and quadruple-mode wideband bandpass filter using simple perturbation in single metal cavity," *IEEE Trans. Microw. Theory Techn.*, vol. 63, no. 10, pp. 3416-3424, Oct. 2015.

[18] Z. C. Guo, S.W. Wong, J.Y. Lin, L. Zhu, Q.-X. Chu, Q. Zhang, and Y. Yang, "Triple-mode cavity bandpass filter on doublet with controllable transmission zeros," *IEEE Access*, vol. 5, pp. 6969-6977, 2017.

[19] J. Y. Lin, S.W. Wong, L. Zhu and Q.X. Chu, "Design of miniaturized triplexers via sharing a single triple-mode cavity resonator," *IEEE Trans. Microw. Theory Techn.*, vol. 65, no. 10,

pp. 3877-3884, Oct. 2017.

[20] J. Y. Lin, S. Wong, Y. Wu, L. Zhu, Y. Yang and Y. He, "A new concept and approach for integration of three-state cavity diplexer based on triple-mode resonators," *IEEE Trans. Microw. Theory Techn.*, vol. 66, no. 12, pp. 5272-5279, Dec. 2018.

[21] J. Y. Lin, S.W. Wong, Y.M. Wu, Y. Yang, L. Zhu and Y. He, "Three-way multiple-mode cavity filtering crossover for narrowband and broadband applications," *IEEE Trans. Microw. Theory Techn.*, vol. 67, no. 3, pp. 896-905, Mar. 2019.

[22] J. Y. Lin, Y. Yang, S.-W. Wong, R.-S. Chen, Y. Li, L. Zhang, Y. He and L. Zhu, "Cavity filtering magic-T and its integrations into balanced-to-unbalanced power divider and duplexing power divider," *IEEE Trans. Microw. Theory Techn.*, vol. 67, no. 12, pp. 4995-5004, Dec. 2019.

[23] S. Bastioli, C. Tomassoni and R. Sorrentino, "A new class of waveguide dual-mode filters using TM and nonresonating modes," *IEEE Trans. Microw. Theory Techn.*, vol. 58, no. 12, pp. 3909-3917, Dec. 2010.

[24] G. L. Matthaei, L. E. O. Young, and E. M. T. Jones, *Microwave Filters, and Coupling Structures*. NJ, USA: Artech House, 1985.

[25] J.-S. Hong and M. J. Lancaster, Microstrip Filters for RF/Microwave Applications. New York: Wiley, 2001.

Chapter 4 In-Band Full-Duplex Filtering Antenna Arrays Based on High-Order Mode Resonators

4.1 Introduction

In-band full-duplex (IBFD) transceiver systems, capable of simultaneously transmitting or receiving dual-polarized signals, can improve the spectral efficiency to resolve the congested frequency spectrum of the wireless communication systems. A suitable choice for these systems includes a dual-polarized antenna, along with an orthomode transducer (OMT) [1]-[7]. The latter provides the required combination or separation of the orthogonally polarized signals. The most common OMT structure consists of the four branch ports and one common port with a square [1], [2], or circular cross-section [3], [4]. Besides linear polarization, the circular polarization duplexing concept was first introduced in [5] and developed in the terahertz [6], and sub-millimeter-wave [7] bands.

To further improve the gain and sidelobe level of the radiating performance, a single antenna element tends to be replaced by the antenna arrays in the IBFD systems [8]-[14]. They can be classified into different categories: microstrip patches [8]-[10], substrate-integrated waveguides (SIW) [11], and waveguide cavities [12]-[14]. Limited radiating elements in the reported designs [8]-[12] suffer a low gain and wide 3-dB beamwidth, which can be further improved. [13] and [14] presented the 16 × 16 high-performance waveguide slot arrays with a realized gain of 32.3 and 31.4 dBi, respectively. The overlapping bandwidth and isolation between two channels are 5%, 17.1%, and 52 dB, 40 dB, respectively. However, the large number of radiating elements requires a bulky and complicated power splitting network, which causes high insertion loss and means that design will be a complex process.

To tackle this issue, the elimination of the power splitting network by adopting high-order mode resonators has been investigated [15]-[18]. In [15], a 3 × 3 slotted antenna array based on TE_{330} high-order mode was designed with an impedance bandwidth of 26% and a maximum gain of 13.8 dBi at the millimeter-wave band. In [16], a TE_{810} mode is adopted to achieve an 8 × 8 slot array with an FBW of 10.17% and a realized peak gain of 24.5 dB. Recently, a 3rd-order single-band filtering antenna array (FAA) using TM_{450} mode and a 3^{rd}-order dual-band dual-polarized filtering antenna array using TM_{430} and TM_{340} modes were demonstrated with the featured capability of unwanted high-order modes suppression [18], which shows advantages of reduced design complexity and ease-of-implementation comparing with the filtering antenna arrays using fundamental modes [19], [20]. However, to the best of the author's knowledge, there is no related literature in the IBFD systems.

Previous work [18] demonstrated that a single high-order mode cavity resonator could produce in-phase outputs with the same amplitudes simultaneously so that the power splitting network is not required. Furthermore, recent advances in multiple-mode resonators (MMRs) [21] demonstrate that the modal orthogonality among multiple modes can provide high isolation among channels [22]-[25]. Therefore, high-order MMRs are ideal for IBFD filtering antenna arrays in microwave transceiver systems, as presented in [26]. This paper is the extended version of [26], which discussed the TM_{120} and TM_{210} modes for narrowband applications. This paper is the extended version of [26], which covers a comprehensive investigation of design concepts and theoretical analysis. Additionally, the proposed method is extended to both narrowband and wideband application scenarios by introducing higher-order modes (TM_{140}/TM_{410} and TM_{160}/TM_{610}). A higher realized gain and better isolation level are achieved, taking advantage of higher-order modes.

In this paper, we propose a novel IBFD filtering antenna arrays based on high-order MMRs. The advantages of the proposed IBFD filtering antenna arrays can be summarized as follows: Firstly, single-element radio frequency (RF) frontend with multifunctions, includes integrated bandpass filters (BPFs), OMT, power splitting network, and cavity slot arrays, which can avoid the interconnection loss with reduced dimensions. Secondly, reduced design complexity is realized. Two orthogonal channels share the same cavity resonator without interaction. Furthermore, the cavity resonator is also adopted to integrate array elements for radiation, where the power splitters for both channels are not required. Thirdly, perfect full-duplex bandwidth overlapping is possible. Due to the identical characteristics for a pair of degenerate modes, both channels have identical frequency responses and radiation patterns. With this in mind the fully overlapped bandwidth can be achieved for the efficient use of spectrum resources. Fourthly, high gain and high selectivity with in-band flatness can be achieved.

4.2 Orthogonal Modes and Their Applications

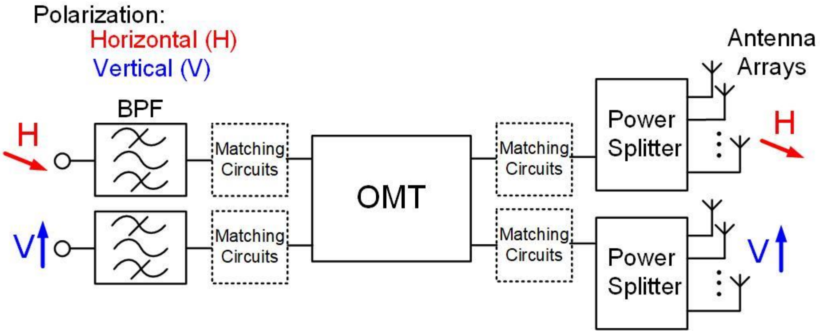

(a)

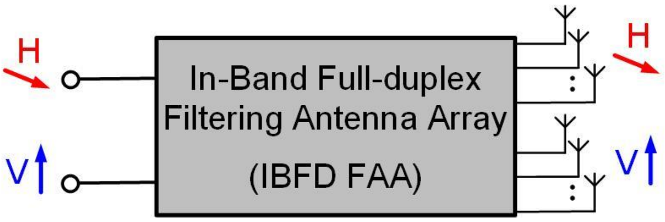

(b)

Fig. 4.1. Schematic of (a) Conventional radio frequency frontend of a communication system, including cascaded BPFs, an OMT, power splitters, and antenna arrays, and (b) The proposed single-element filtering IBFD array.

Fig. 4.1(a) shows the schematic of a conventional RF frontend filtering IBFD array system. It consists of two bandpass filters (BPFs), an OMT, two power splitters, and two antenna arrays cascaded by matching circuits. Horizontal port (H-port) and vertical port (V-port) signals are transmitted separately in the proposed system without mutual interference. A very compact structure integrating all of them into one microwave circuit, namely IBFD filtering antenna array, is shown in Fig. 4.1(b). The proposed IBFD antenna does not require interconnection and matching circuits, leading to a miniaturized system with reduced insertion loss.

In [18], the TM_{mn0} modes cavity resonators were comprehensively discussed. The TM_{mn0} MMRs satisfy the condition: $c \ll a$ and b (a, b, and c represent the length, width, and height of a rectangular cavity resonator, respectively). For a single resonator, the length a and width b serve to control the resonant frequency of the proposed modes, while the height c is a parameter to adjust unloaded quality factor Q_u of the cavity resonator [27].

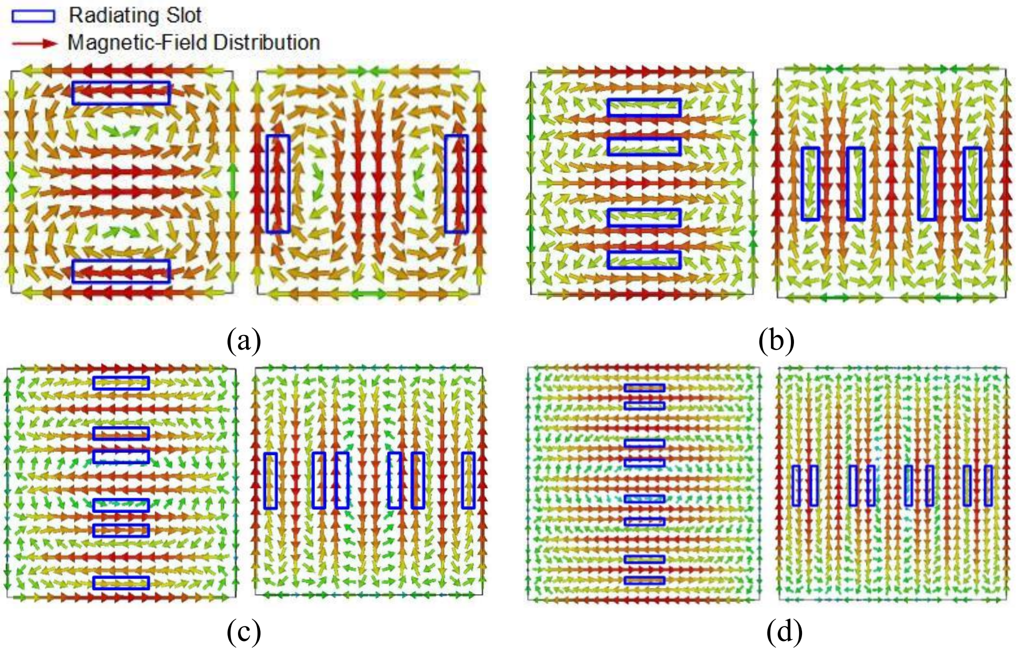

Fig. 4.2. Magnetic field distributions of each pair of degenerate modes with slots etched in the TM_{1n0} and TM_{n10} resonators. (a) TM_{120} & TM_{210}, (b) TM_{140} & TM_{410}, (c) TM_{160} & TM_{610}, (d) TM_{180} & TM_{810}.

Based on this concept, a series of TM_{mn0} ($m = n-1$, $n = 2, 3, 4\cdots\cdots$) modes were adopted in [18] for single-band and dual-band dual-polarized filtering antenna array designs. However, the adopted degenerate modes are not suitable for the IBFD array designs. They are not purely modal orthogonal to each other, so this cannot guarantee good isolation between the two channels.

To tackle this challenge, a series of degenerate modes, TM_{1n0} and TM_{n10} (n is even), are explored to achieve the high gain, reduce the sidelobe level, and enhance the isolation and cross-polarization level between channels. The first four pairs of proposed degenerate modes TM_{1n0} and TM_{n10} ($n = 2, 4, 6, 8$) with radiating slots etched are depicted in Fig. 4.2. It is observed that the radiating slots on the radiation surface are symmetrical, which guarantees the pure boresight radiation pattern. In addition, for each pair of degenerate modes, the etched radiating slots for one mode have a minimal effect on the other, which can realize the independent radiating elements control for each channel. According to [18], the more units the array has, the higher gain the array can achieve. The Q_u value increases when adopting a higher-order mode regarding filtering performance.

4.3 Narrow-Band IBFD Filtering Antenna Array Using TM_{160} And TM_{610} Modes

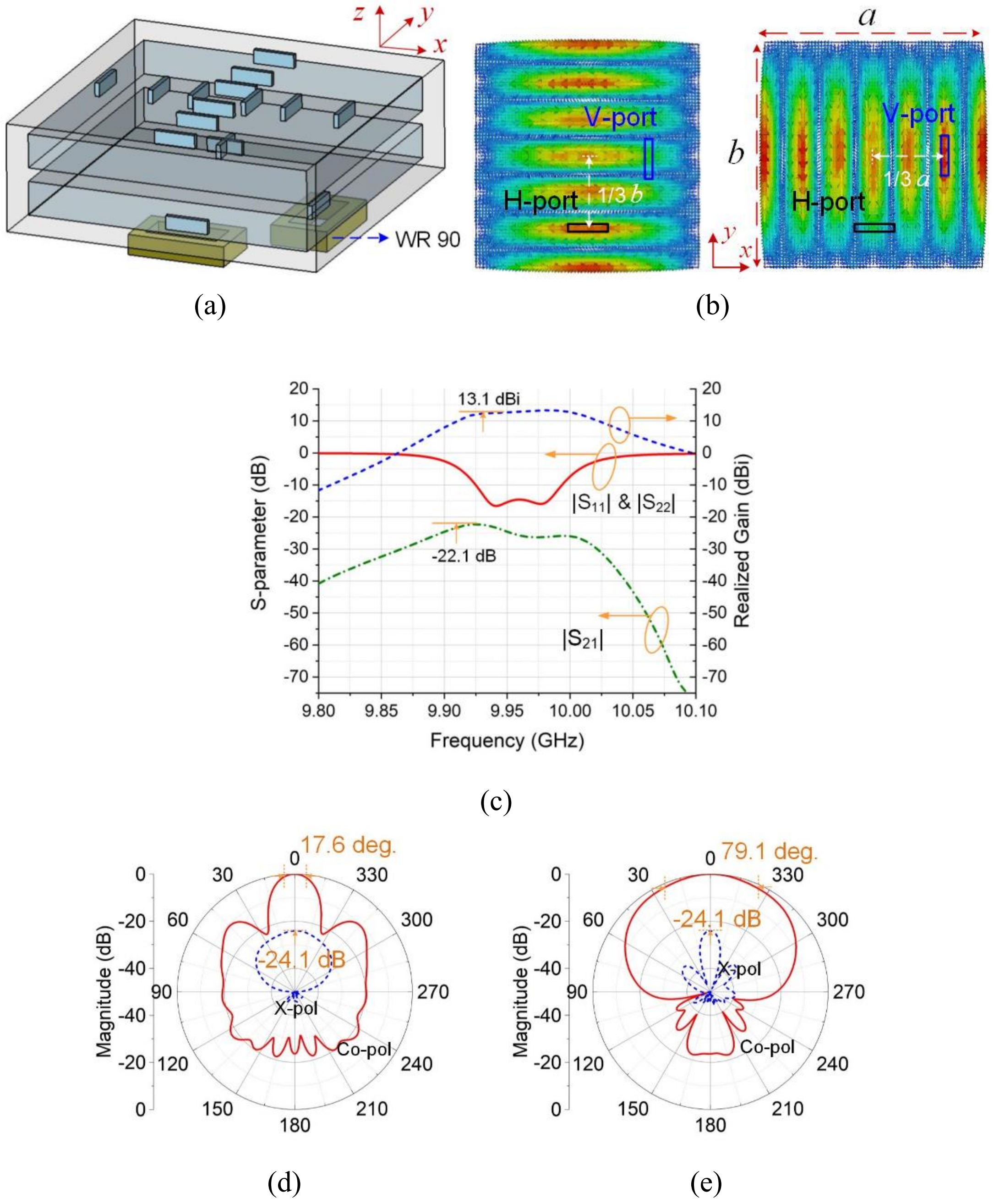

(a) (b)

(c)

(d) (e)

Fig. 4.3. 2^{nd}-order filtering full-duplex slot array using TM_{160} & TM_{610} modes cavity resonator: (a) Initial geometrical configuration, (b) Magnetic-field distributions with WR-90 location, (c) S-parameters and realized gains, (d)-(e) E- and H-plane normalized radiation patterns at 9.97 GHz.

In [26], a 2^{nd}-order IBFD slot antenna is presented with a bandwidth of 3.3% and a realized gain of 10.3 dBi. The isolation between two channels is 15 dB. To further enhance the realized gain and improve the isolation level between channels, the IBFD filtering antenna arrays using high-order modes with more radiating elements are investigated. This part presents the design of a narrowband IBFD filtering antenna array using TM_{610} & TM_{160} modes, the implemented Q_u value of both modes is 6566.

Fig. 4.3(a) presents the initial geometrical configuration of the proposed array prototype. Two dual-mode cavity resonators are cascaded to form a 2^{nd}-order filtering response. Each of them is shared by TM_{160} and TM_{610} modes. As is shown in Fig. 4.2(a), two orthogonal 1 × 6 arrays are located at the upper dual-mode resonator's surface, and each of them is dominated by TM_{160} and TM_{610} modes, respectively. The horizontal 1 × 6 array is distributed evenly at the maximal magnetic-field loops of TM_{610} mode, where the field intensities of TM_{160} mode are relatively weak. In contrast, the case for the vertical 1 × 6 array is vice versa. In Fig. 4.3(b), two WR-90 ports, namely H-port and V-port, are adopted to feed this structure. Similarly, the feeding port should be located at the maximal energy distribution of one mode, where the other mode is very weak. For this reason, the H-port is located at a distance of $1/3b$ along the negative y-axis, while V-port is located at a distance of $1/3a$ along the active x-axis. As is shown on the left-hand side of Fig. 4.3(b), the H-port is located at the maximal magnetic-field loop of TM_{160} to excite this mode. In contrast, the V-port is located at the symmetrical magnetic-field distribution of TM_{160}, leading to a zero-energy output due to the opposite magnetic-field directions. Similarly, as shown on the right of Fig. 4.3(b), the V-port excites the TM_{610} mode.

Considering the specification of a center frequency of 10 GHz, 10-dB bandwidth (FBW) of 0.6%, and ripple level of 0.2 dB, the formulas of external quality factors Q_e and coupling coefficients K of 2^{nd}-order Butterworth response are depicted as:

$$Q_e = \frac{g_0 g_1}{FBW} \tag{4-1a}$$

$$K_{12} = \frac{FBW}{\sqrt{g_1 g_2}} \tag{4-1b}$$

where g_0, g_1, g_2, and g_3 are the low-pass prototype element values of filter synthesis, which can be set as $g_0= g_3=1$ and $g_1=g_2=1.4142$ [28]. After substituting the chosen values, the calculated external quality factor and coupling coefficient are Q_e=1.4142, and K_{12}=K_{23}=0.007, respectively.

The values of Q_e and K of the proposed design can be obtained from the filter extraction in EM simulation. In the geometrical configuration of Fig. 4.3(a), the length l_1 and width of the coupling slot are used to control Q_e from the WR-90 port to the structure, while the parameters of slots on the radiation surface are used to control Q_e from vacuum to structure. The Q_e value can be obtained using the following calculation [29]:

$$Q_e = \frac{2\pi f_0 \tau_{s11}(f_0)}{4} \tag{4-2}$$

where $\tau_{s11}(f_0)$ represents the group delay at the resonance. Meanwhile, the slots between two high-order dual-mode resonators control the coupling coefficient K between cavity resonators. The K value can be obtained using the following equation [28]:

$$K = \frac{f_{p2}^2 - f_{p1}^2}{f_{p2}^2 + f_{p1}^2} \tag{4-3}$$

where f_{p1}, and f_{p2} represent the two resonant peaks. It is noted that the slotted array also serves as the second resonator in the filter network. The input external quality factor from the waveguide feed can be represented as Q_{ein}, which should have the same value as the radiation external quality factor, namely Q_{erad}.

Fig. 4.3(c) presents the simulated S-parameters and realized gains of the initial configuration in Fig. 4.3(a). Both channels resonate at 9.97 GHz with a 10-dB bandwidth of 60 MHz. The isolation level $|S_{21}|$ is better than 22.1 dB for both channels, while the peak gain is 13.1 dBi within the frequency range. The E- and H-plane normalized radiation patterns for TM_{160} mode channel at 9.97 GHz, as shown in Figs. 4.3(d)-(e), identical to that of the TM_{610} mode channel. It can be seen that the 3-dB beamwidths are 17.6 degrees at E-plane and 79.1 degrees at H-plane, respectively. The cross-polarization level is -24.1 dB for both E-plane and H-plane.

To further integrate with more radiating elements for a higher realized gain and a narrower H-plane 3-dB beamwidth, the improved geometry of the proposed IBFD filtering antenna array is presented in Fig. 4.4(a). Compared with the initial geometry with 1 × 6 arrays for both channels in Fig. 4.3(a), the proposed design can implement 5 × 6 arrays in each channel without an increased circuit size. To realize this array, the distributed array elements dominated by one mode should have little effect on the other mode in a dual-mode resonator. TM_{160} mode is taken as an example in Fig. 4.4(b). As

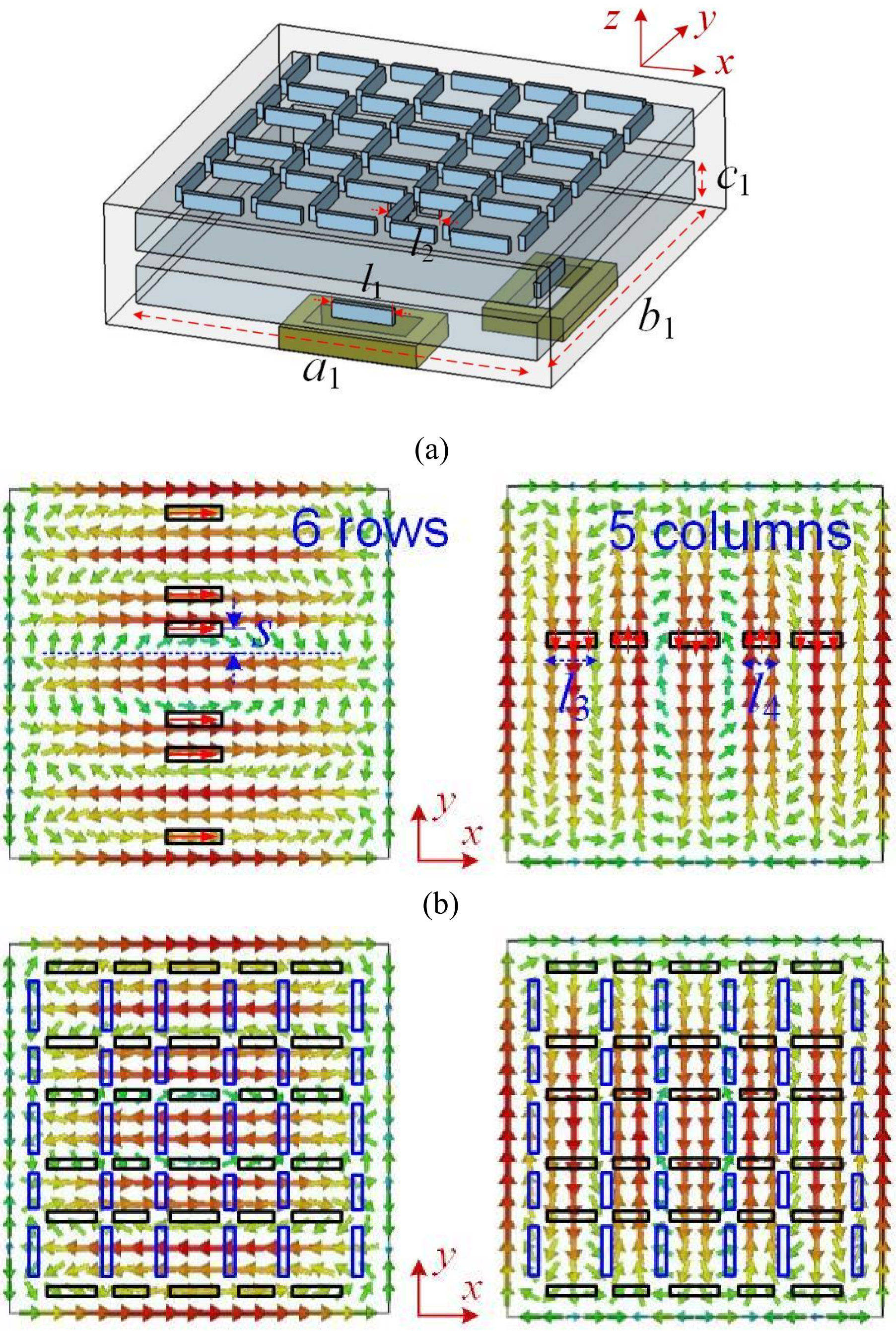

(a)

(b)

(c) (d)

Fig. 4.4. 2nd-order IBFD filtering antenna array using TM_{160} & TM_{610} modes cavity resonator: (a) Final geometrical configuration, (b) Simple slot distributions for TM_{160} mode, (c) Slot distributions based on TM_{160} mode, (d) Slot distributions based on TM_{610} mode.

discussed above, a 1 × 6 array (6 rows) can be implemented based on TM_{160} mode as depicted on the left-hand side of Fig. 4.4(b). In terms of column number, the added array elements should be located where the magnetic field energy of TM_{160} is zero.

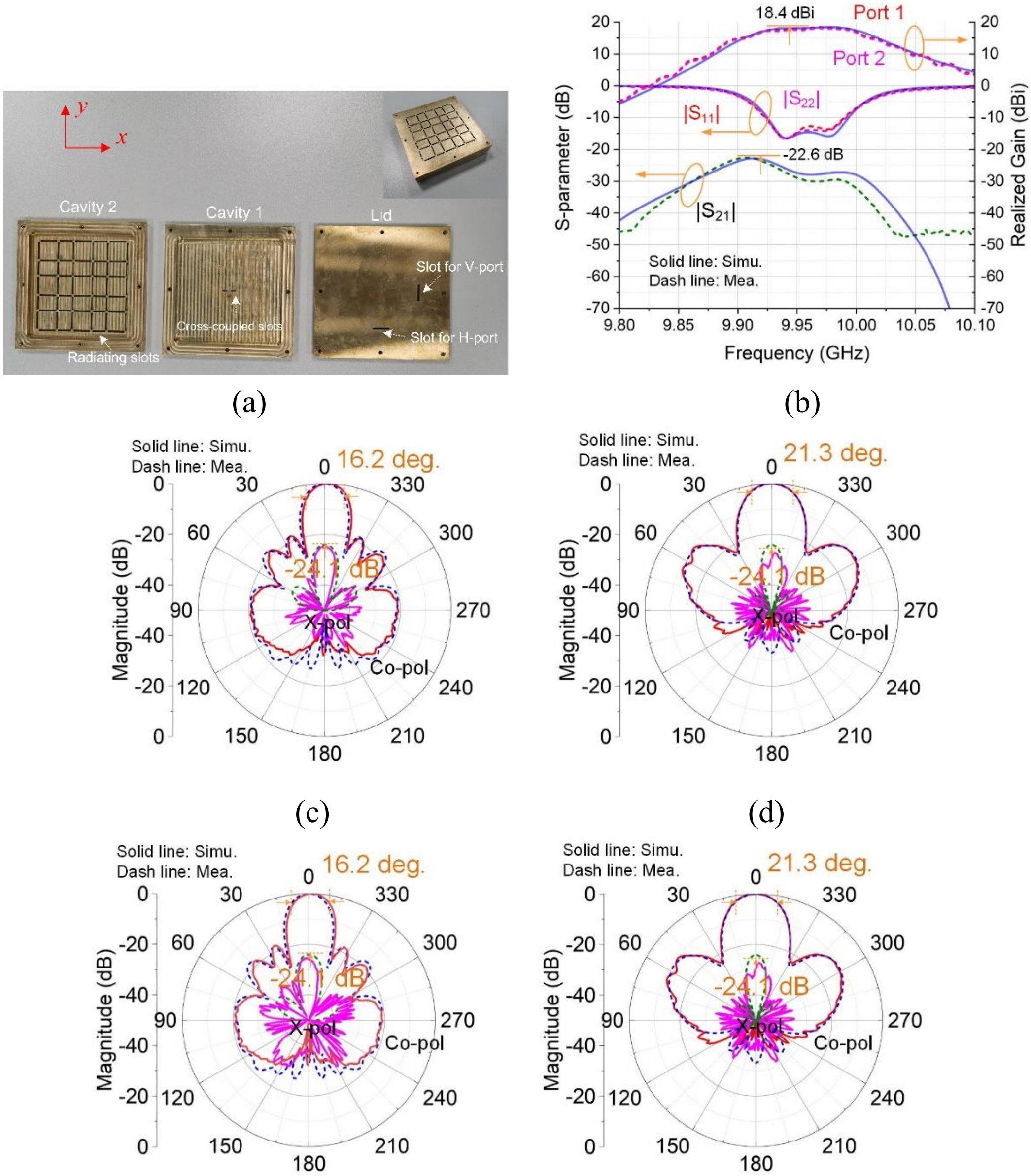

(a) (b)

(c) (d)

(e) (f)

Fig. 4.5. 2nd-order narrow-band IBFD filtering antenna array using TM_{160} & TM_{610} modes cavity resonator: (a) Photos of fabricated prototype, (b) S-parameters and realized gains, (c)-(d) E- and H-plane normalized radiation patterns at 9.97 GHz for V-port, (e)-(f) E- and H-plane normalized radiation patterns at 9.97 GHz for H-port.

Therefore, 5 columns satisfy this condition, as depicted on the right in Fig. 4.4(b). The lengths of the first, third, and fifth slot columns are denoted as l_3, while the lengths of the second and fourth slot columns are denoted as l_4. In other words, 5 × 6 arrays can be implemented to radiate the EM energy of TM_{160} mode while they have little effect on that of TM_{610} mode.

A 5 × 6 array for TM_{160} mode band and a 6 × 5 array for TM_{610} mode band can be implemented simultaneously on the surface of the last resonator order in the proposed design. Figs. 4.5(c)-(d) show the radiating slot distributions on the magnetic-field loop of TM_{160} mode and TM_{610} mode, respectively. These slot elements do not interfere with each other, which guarantees the isolation level between channels.

The physical model in [24] is used to extract Q_e and K of each channel of the proposed full-duplex array. The length l_1, width, and thickness of the slot between WR-90 and resonator are adopted to control Q_{ein} of the channels, while the lengths l_3, l_4, and offset s of the radiating slot elements are adopted to control Q_{erad} of the channels. The length l_2, width, and thickness of the slot between resonators are adopted to control K of the channels. The parameter values are appropriately allocated to meet the filtering response for each channel, which are tabulated in Table 4.1. To achieve the identical resonant frequencies for both high-order degenerate modes, the length a is equal to the width b. The width and thickness of the slots are set as 1.5 mm and 3 mm, respectively.

Fig. 4.5(a) shows a photograph of the fabricated full-duplex array prototype using three brass layers assembled together. The measured S-parameters and the realized gains of the prototype are shown in Fig. 4.5(b), along with the corresponding simulation. It has two transmission poles with a return loss level of 15 dB, indicating a 2nd-order filtering response. Both channels resonate at 9.97 GHz with a 10-dB bandwidth of 60 MHz. The isolation $|S_{21}|$ between channels is better than 22.6 dB, while the realized gain has been enhanced to 18.4 dBi with an increment of 5.3 dB, compared with 13.1 dBi in Fig. 4.3(c). The achieved total efficiency is 90% within the band. The E- and H-plane radiation patterns for TM_{160} mode channel at 9.97 GHz are shown in Figs. 4.5(c)-(d), which are quite similar to those of TM_{610} mode at 9.97 GHz in Fig. 4.5(e)-(f). It can be seen that the 3-dB beamwidth is slightly reduced to 16.2 degrees at E-plane, compared with 17.6 degrees in Fig. 4.3(d), while the 3-dB beamwidth is significantly reduced to 21.3 degrees at H-plane, compared with 79.1 degrees in Fig. 4.3(e). The cross-polarization levels are better than 24.1 dB at E- and H-plane, respectively.

TABLE 4.1
PHYSICAL DIMENSIONS OF THE PROPOSED IBFD FILTERING ANTENNA ARRAY (UNIT: MM)

$a_1 = 90$	$b_1 = 90$	$c_1 = 5$	$l_1 = 13.7$
$l_2 = 11.4$	$l_3 = 14.3$	$l_4 = 11$	$s = 1$

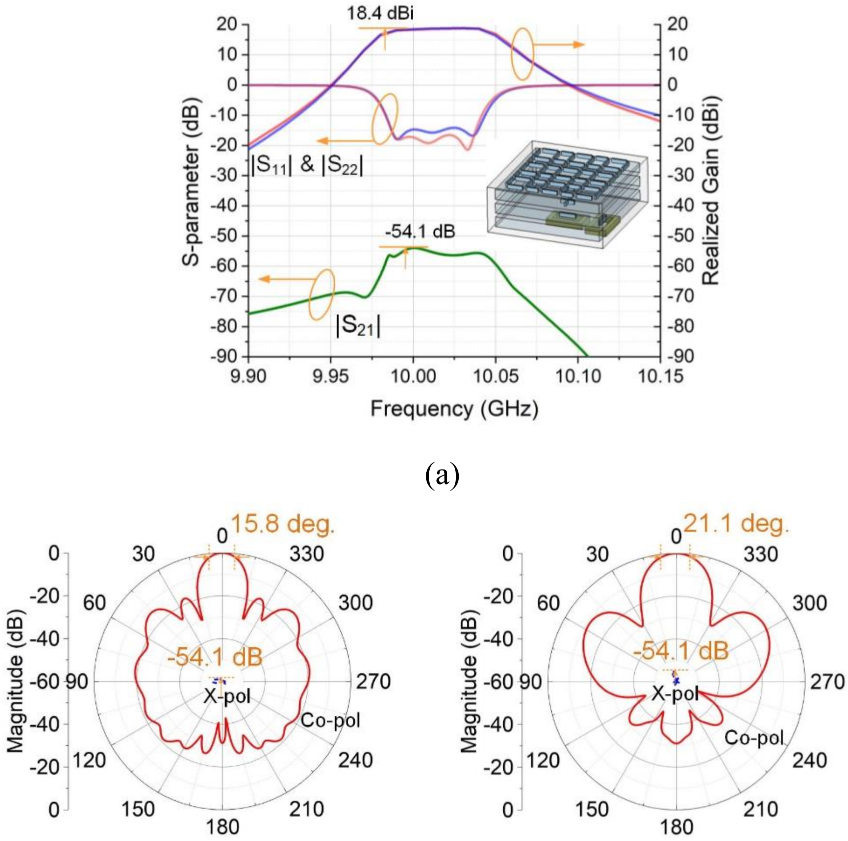

(a)

(b) (c)

Fig. 4.6. 3rd-order narrow-band IBFD filtering antenna array using TM160 & TM610 modes cavity resonator: (a) S-parameters and realized gains, (b) E- and (c) H-plane normalized radiation patterns at 10.03 GHz.

A 3rd-order IBFD filtering antenna array prototype is presented in the inset of Fig. 4.6(a) for higher-order filtering response verification and further isolation improvement. Compared with the 2nd-order prototype in Fig. 4.4(a), one more cavity resonator is cascaded, and the H-port is shifted to the center of the resonator surface.

The simulated S-parameters and realized gains are shown in Fig. 4.6(a). Both channels resonate at 10.03 GHz with a 10-dB bandwidth of 60 MHz, and they have three transmission poles with a return loss level of 15 dB, indicating a 3rd-order filtering response. $|S_{11}|$ and $|S_{22}|$ are slightly different due to the offsetting of H-port, but they are mostly overlapped. The realized gain of the channels achieves 18.4 dBi with better selectivity. However, the isolation between channels $|S_{21}|$ is significantly reduced to -54.1dB, compared with -22.6 dB in Fig. 4.5(b). The E- and H-plane radiation patterns for TM_{160} mode channel at 10.03 GHz are shown in Fig. 4.6(b)-(c), thus indicating the

3-dB beamwidth of 15.8 degrees at E-plane and 21.1 degrees at H-plane, respectively, which are quite similar to those in Fig. 4.5(c)-(f). However, the cross-polarization level is significantly reduced to -54.4 dB at E-plane and -54.1 dB at H-plane, respectively, compared with 24.1 dB at E- and H-plane in Figs. 4.5(c)-(f).

4.4. Wide-Band IBFD Filtering Antenna Array Using TM_{140} And TM_{410} Modes

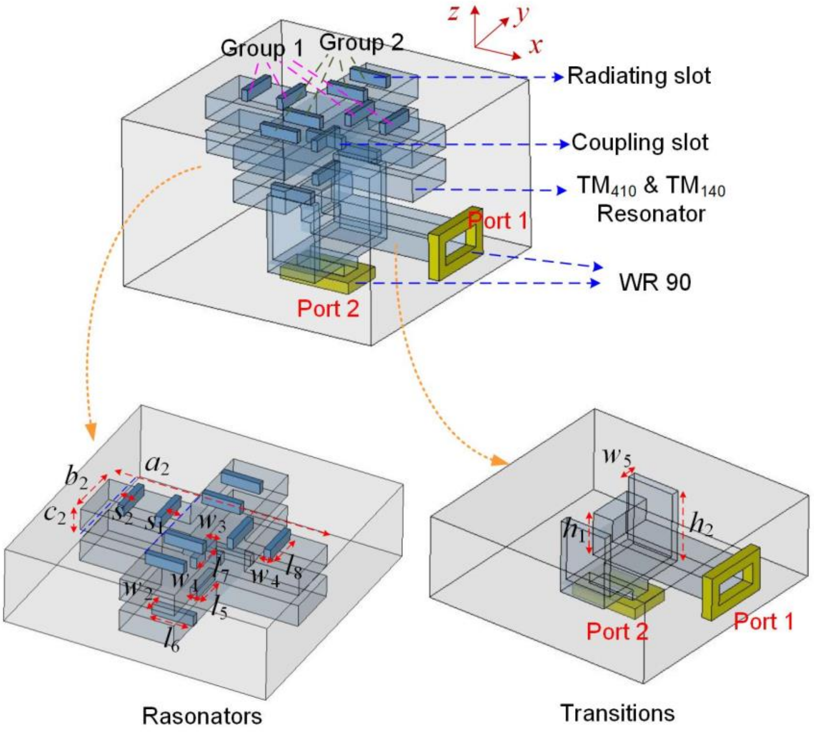

Fig. 4.7. 3-D view of 5^{th}-order wide-band IBFD filtering antenna array using TM_{410} and TM_{140} modes with resonator part and transition part.

In [30], a novel high-mode resonator is investigated to provide wideband performance. Two TM_{410} mode resonators and three $TM_{410\text{-like}}$ modes are placed in parallel to form a transversal quintuplet topology with two transmission zeroes (TZs). Therefore, a pair of degenerate modes TM_{410} and TM_{140}, with their respective $TM_{410\text{-like}}$ and $TM_{140\text{-like}}$ modes, are suitable for wideband IBFD filtering antenna array design.

Fig. 4.7 shows the 3-D view of the proposed wideband full-duplex array configuration. It can be regarded as a combination of the resonator part and transition part. The resonator part consists of two cross-shaped resonators, eight radiating slots,

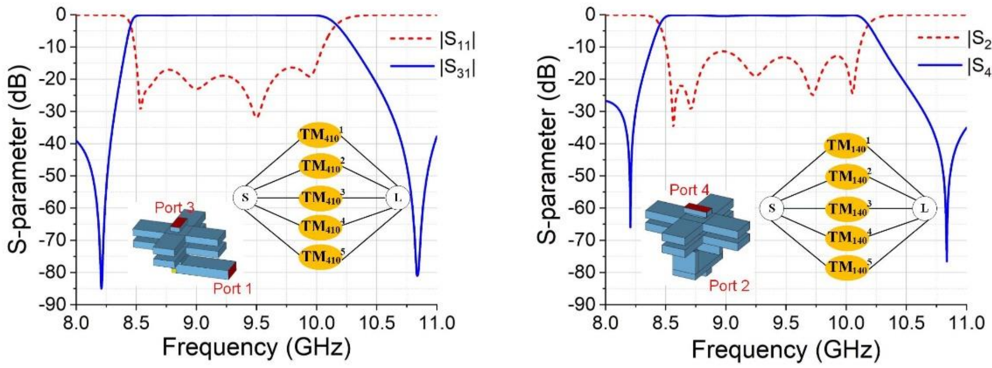

(a) (b)

Fig. 4.8. Simulated S-parameters for: (a) Port 1 to virtual port 3, (b) Port 2 to virtual port 4.

and five coupling slots. The long-edge of the cross-shaped resonators with its direction parallel to the *x*-axis produces the resonances of TM_{410} and $\mathrm{TM}_{410\text{-like}}$ modes. The coupling slot is placed in the center and matched to port 1 through the transition. Four radiating slots are placed in a line along the *x*-axis. Similarly, the long edge of the resonators parallel to the *y*-axis produces the resonances of TM_{140} and $\mathrm{TM}_{140\text{-like}}$ modes. One coupling slot is placed in the center between two cross-shaped resonators, while the other two coupling slots are placed symmetrically and finally combined into port 2 through the transition. Four radiating slots are placed in a line along the *y*-axis.

As shown in Fig. 4.7, there are two groups of radiating slots, namely group 1 for four radiating slots along the *x*-axis and group 2 for four radiating slots along the *y*-axis. To verify the filtering capacity at two orthogonal ports, when port 1 works, the radiating slots in group 1 are represented by the virtual port 3 as shown in the inset of Fig. 4.8(a). There are five resonating modes, namely $\mathrm{TM}_{410}{}^{1}$, $\mathrm{TM}_{410}{}^{2}$, $\mathrm{TM}_{410}{}^{3}$, $\mathrm{TM}_{410}{}^{4}$, and $\mathrm{TM}_{410}{}^{5}$. When they satisfy the conditions that: $M_{s1} = M_{1L}$, $M_{s3} = M_{3L}$, $M_{s5} = M_{5L}$ while $M_{s2} = -M_{2L}$, $M_{s4} = -M_{4L}$, 2) $M_{s2} > M_{s1}$ and $M_{s4} > M_{s5}$, a transversal quintuplet topology can be achieved with two TZs one at lower stopband while the other one is at the upper stopband. The relative coupling matrix response for the prototype in the inset of Fig. 4.8(a) is shown below:

$$M = \begin{bmatrix} 0 & 0.35 & 0.52 & 0.554 & 0.541 & 0.39 & 0 \\ 0.35 & 1.42 & 0 & 0 & 0 & 0 & 0.35 \\ 0.52 & 0 & 0.891 & 0 & 0 & 0 & -0.52 \\ 0.554 & 0 & 0 & 0.087 & 0 & 0 & 0.554 \\ 0.541 & 0 & 0 & 0 & -0.775 & 0 & -0.541 \\ 0.39 & 0 & 0 & 0 & 0 & -1.217 & 0.39 \\ 0 & 0.35 & -0.52 & 0.554 & -0.541 & 0.39 & 0 \end{bmatrix} \tag{4-4}$$

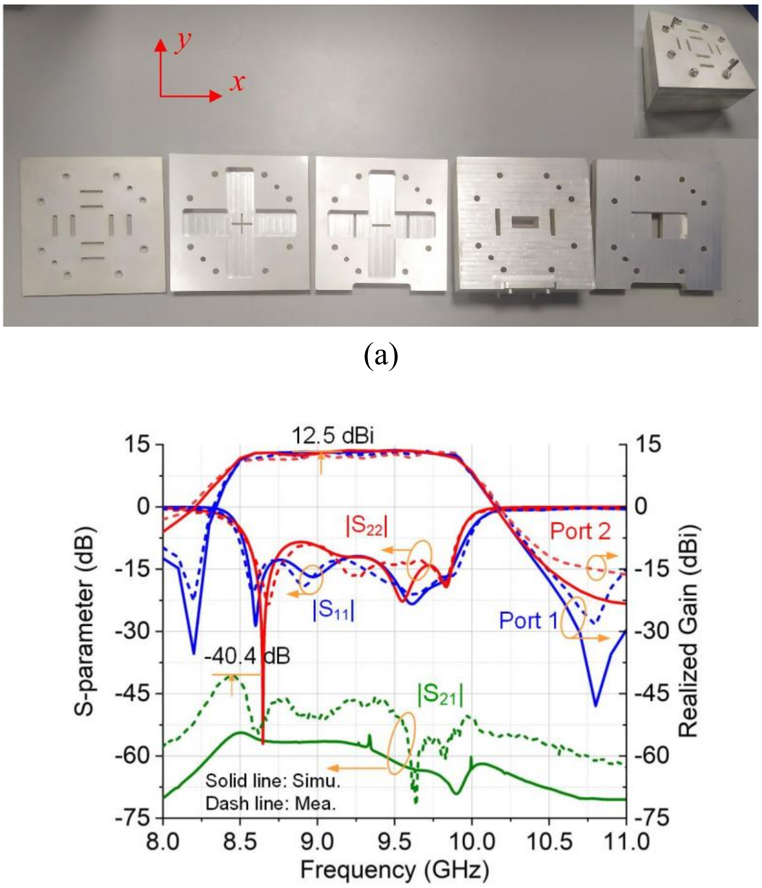

(a)

(b)

Fig. 4.9. 5th-order wide-band IBFD filtering antenna array using TM_{410} and TM_{140} modes: (a) Photos of the fabricated prototype, (b) S-parameters and realized gains.

The S-parameters in Fig. 4.8(a) show that it possesses a 1-dB fractional bandwidth of 17.2% at 9.3 GHz and two TZs with one at 8.2 GHz and the other one at 10.8 GHz, respectively. Similarly, when port 2 is excited, the radiating slots in group 2 are represented by a virtual port 4. There are as well another five resonating modes, specifically TM_{140}^{1}, TM_{140}^{2}, TM_{140}^{3}, TM_{140}^{4}, and TM_{140}^{5}. They are orthogonal to the former five modes, respectively. They also satisfy the same conditions and coupling matrix to have a similar S-parameter response. Port 2 also resonates at 9.3 GHz with a 1-dB bandwidth of 17.2% and two TZs with one at 8.2 GHz and the other one at 10.8 GHz, respectively. Therefore, when port 3 and port 4 are replaced by two groups of radiating slots, wideband performance can be also possessed at port 1 and port 2, respectively.

Fig. 4.9(a) is a photograph of the fabricated wideband full-duplex array prototype using five silver-plated brass layers which are assembled together. The measured S-

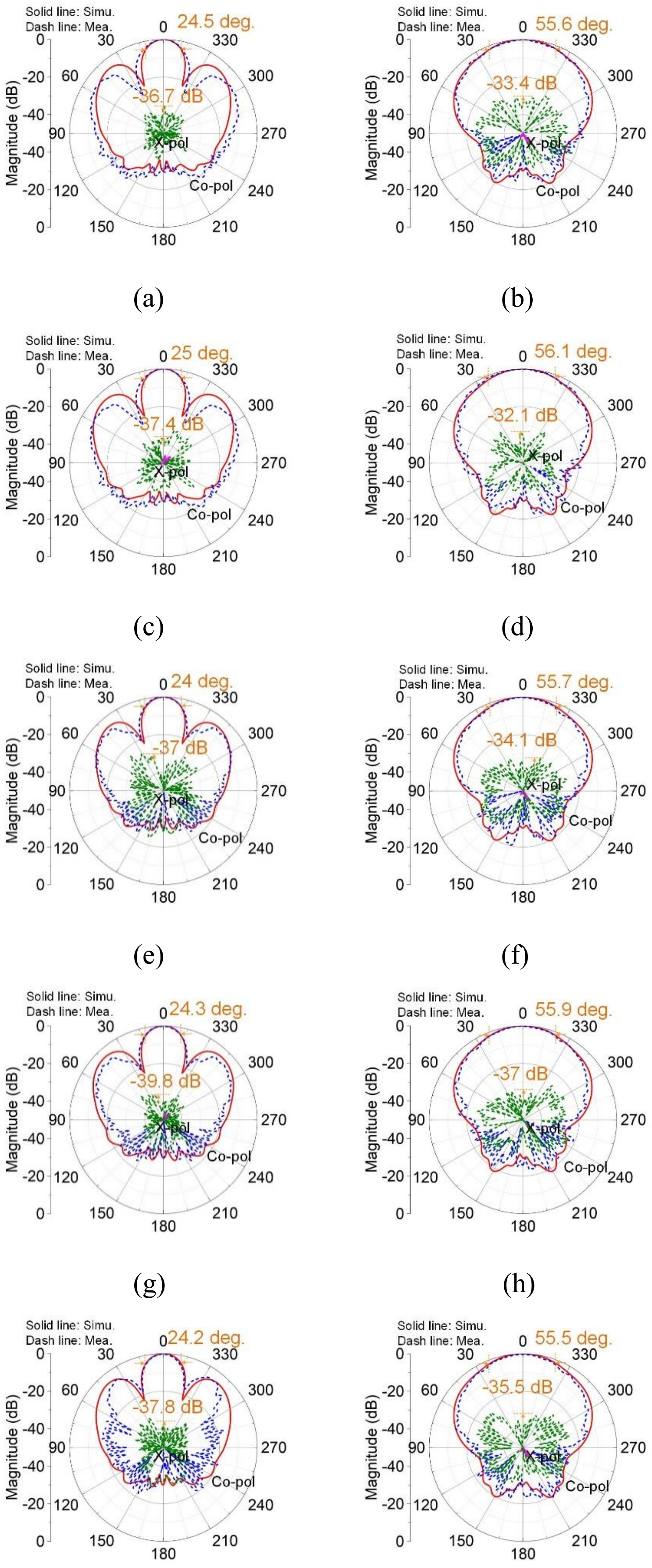
Solid line: Simu.
Dash line: Mea.
Magnitude (dB)
0
-20
-40
30
60
90
120
150
180
210
240
270
300
330
X-pol
Co-pol
24.5 deg.
-36.7 dB
55.6 deg.
-33.4 dB
25 deg.
-37.4 dB
56.1 deg.
-32.1 dB
24 deg.
-37 dB
55.7 deg.
-34.1 dB
24.3 deg.
-39.8 dB
55.9 deg.
-37 dB
24.2 deg.
-37.8 dB
55.5 deg.
-35.5 dB

(a) (b)

(c) (d)

(e) (f)

(g) (h)

(i) (j)

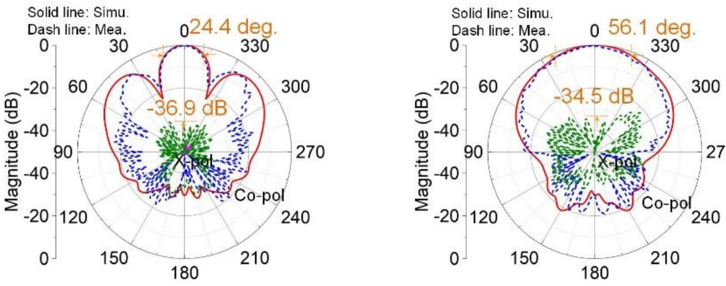

(k) (l)

Fig. 4.10. 5th-order wide-band IBFD filtering antenna array using TM_{410} and TM_{140} modes: E- and H-plane normalized radiation patterns at 8.5 GHz for (a)-(b) Port 1 and (c)-(d) Port 2. E- and H-plane normalized radiation patterns at 9.2 GHz for (e)-(f) Port 1 and (g)-(h) Port 2. E- and H-plane normalized radiation patterns at 9.9 GHz for (i)-(j) Port 1 and (k)-(l) Port 2.

parameters and the realized gains of the prototype are shown in Fig. 4.9(b), along with the corresponding simulation. Port 1 resonates at 9.23 GHz with a bandwidth from 8.51 GHz to 9.96 GHz. The realized gain is smooth and flat, with a peak gain of 12.5 dBi within the passband. Two radiation nulls also occur at 8.2 GHz and 10.8 GHz, respectively. While port 2 is excited at 9.2 GHz with a bandwidth from 8.5 GHz to 9.9 GHz. The realized gain is also flat, with a peak gain of 12.2 dBi within the passband. However, two radiation nulls are missed, which might be the function of four radiating slots that could not replace the virtual port 4. However, port 2 still possesses a high roll-off beside the passband. The measured isolation $|S_{21}|$ between channels is better than 40.4 dB, compared with 51.3 dB in simulation, the discrepancy of 10 dB may be attributed to the sensitivity of fabricated prototype. The achieved total efficiency is 90% within the band. The E- and H-plane radiation patterns at 8.5 GHz, 9.2 GHz, and 9.9 GHz, excited at port 1 and port 2, are shown in Fig. 4.10. It is evident that both E- and H-plane patterns for port 1 and port 2 remain stable within the resonant frequencies. The 3-dB beamwidth is narrower at E-plane for port 1 and port 2 because of the integration of more radiating slots. The cross-polarization levels are better than 30 dB at E- and H-plane, respectively.

The relative physical dimensions of the proposed wideband filtering full-duplex array prototype are optimized and finally presented in Table 4.2. The thickness of all the coupling slots is set as 3 mm.

TABLE 4.2

Physical Dimensions of the Proposed IBFD Filtering Antenna Array (Unit: mm)

$a_2 = 92$	$b_2 = 23$	$c_2 = 7.5$	$l_5 = 16.1$
$l_6 = 21.7$	$l_7 = 17.2$	$l_8 = 17.6$	$w_1 = 2.46$
$w_2 = 2.46$	$w_3 = 1.9$	$w_4 = 2.42$	$w_5 = 4$
$s_1 = 3.6$	$s_1 = 5.5$	$h_1 = 10$	$h_2 = 22$

The comparisons between the proposed designs with other reported ones are summarized in Table 4.3. The array element number is quite limited in [8], [10], and [12], which achieves a not very high peak gain. This paper presents a novel design method to use a series of high-order modes to design narrowband and wideband IBFD filtering antenna arrays. In the narrowband application, a 5 × 6 full-duplex array using TM_{160} & TM_{610} modes with an FBW of 1% and a realized gain of 18.4 dBi. While in the wideband application, 1 × 4 full-duplex array using TM_{140} & TM_{410} modes with an FBW of 15.6% and a realized gain of 11 dBi. [13] and [14] implemented a quite high peak gain within the passband. However, the bulky power splitter network is adopted, which occupies a quite large circuit volume and results in insertion loss. In this work, the power splitter network can be omitted due to utilizing a high-order mode resonator. Furthermore, filters are integrated into the circuit to provide the high selectivity of both channels. The fully overlapped bandwidth avoids the waste of spectrum resources. In other words, the proposed IBFD filtering antenna arrays possess the merits of high gain, high selectivity, high isolation, high efficiency, high power handling capacity, and compact circuit volume, which are suitable for wireless front-end communication systems.

TABLE 4.3

Comparisons with Reported Full-Duplex Antennas

Ref.	Freq. (GHz)	Structure	Elements	Filtering Capacity?	OBW (Fully Overlapped?)	Peak Gain (dBi)	Isolation (dB)	Need Power Splitter Network?
[8]	5.69	Patch	1 × 4	No	19.3% (No)	14.3/13.2	> 57	Yes
[10]	10	SIW	1	No	19% (No)	5.3	> 28	No
[12]	3.47	Full-metal	1 × 2	No	5.8% (No)	8.8	> 72	No

[13]	62	Full-metal	16 ×16	No	5% (No)	32.3	> 52	Yes
[14]	13.6	Full-metal	16 ×16	No	17.1% (No)	31.4	> 40	Yes
Prototype in Sec. III	**10**	**Full-metal**	**5 × 6**	**Yes**	**1% (Yes)**	**18.4**	**> 54.1**	**No**
Prototype in Sec. IV	**9.3**	**Full-metal**	**1 × 4**	**Yes**	**15.6% (Yes)**	**12.5**	**> 40.4**	**No**

OBW: Overlapping bandwidth of two ports. NG: Not given.

4.5. Conclusion

In this chapter, a series of high-order degenerate modes are summarized to implement the design of IBFD filtering antenna arrays. Discovered here is that the pairs of degenerate modes in a single cavity resonator, TM$_{1n0}$ and TM$_{n10}$ (n is even), are suitable for the full-duplex array designs due to their advantages: 1) in-phase and same amplitude for each magnetic loop, which helps to enhance the gain and reduce the sidelobe level; and 2) the modal orthogonality, which guarantees the isolation and cross-polarization level between channels. First, TM$_{160}$ & TM$_{610}$ modes are utilized to design a narrowband 5 × 6 IBFD filtering antenna array with an FBW of 1% and a realized gain of 18.4 dBi. Then, the purpose of TM$_{140}$ & TM$_{410}$ modes is to help design a wideband 1 × 4 IBFD filtering antenna array with an FBW of 15.6% and a realized peak gain of 12.5 dBi and 12.2 dBi, respectively. Both designs are fabricated and measured to verify the proposed design methodology. The advantages of proposed designs can be summarized as follows. Firstly, a very compact structure is produced. Secondly, since the filters, OMT, and antenna arrays are integrated into one circuit, this reduces design complexity. Two individual channels share the same cavity resonator without interaction. Thirdly, fully overlapping bandwidth is achieved and it significantly avoids wasting spectrum resources.

4.6 References

[1] J. Esteban and C. Camacho-Peñalosa, "Compact orthomode transducer polarizer based on a tilted-waveguide T-Junction," *IEEE Trans. Microw. Theory Techn.,* vol. 63,

no. 10, pp. 3208-3217, Oct. 2015.

[2] J. Hwang and Y. Oh, "Compact orthomode transducer using single-ridged triangular waveguides," *IEEE Microw. Wireless Compon. Lett.*, vol. 21, no. 8, pp. 412-414, Aug. 2011.

[3] D. Dousset, S. Claude and K. Wu, "A compact high-performance orthomode transducer for the atacama large millimeter array (ALMA) band 1 (31–45 GHz)," *IEEE Access*, vol. 1, pp. 480-487, 2013.

[4] G. Virone, O. A. Peverini, M. Lumia, G. Addamo and R. Tascone, "Platelet orthomode transducer for Q-band correlation polarimeter clusters," *IEEE Trans. Microw. Theory Techn.,* vol. 62, no. 7, pp. 1487-1494, Jul. 2014.

[5] J. Altman, Microwave Circuits. New York, NY, USA: VanNostrand, 1964.

[6] C. A. Leal-Sevillano, K. B. Cooper, J. A. Ruiz-Cruz, J. R. Montejo-Garai and J. M. Rebollar, "A 225 GHz circular polarization waveguide duplexer based on a septum orthomode transducer polarizer," *IEEE Trans. on Terahertz Science and Technology*, vol. 3, no. 5, pp. 574-583, Sept. 2013.

[7] K. B. Cooper, N. Llombart, G. Chattopadhyay, B. Dengler, R. E. Cofield, C. Lee, S. Filchenkov, and E. Koposova, “A grating-based circular polarization duplexer for submillimeter-wave transceivers,” *IEEE Microw. Wireless Compon. Lett.*, vol. 22, no. 3, pp. 108–110, Mar. 2012.

[8] D. Wójcik, M. Surma, A. Noga, and M. Magnuski, “High port-to-port isolation dual-polarized antenna array dedicated for full duplex base stations,” *IEEE Antennas Wireless Propag. Lett.*, vol. 14, no. 8, pp. 1–5, Aug. 2015.

[9] C. X. Mao, Y. Zhou, Y. Wu, H. Soewardiman, D. H. Werner, and J. S. Jur, “Low-profile strip-loaded textile antenna with enhanced bandwidth and isolation for full-duplex wearable applications,” *IEEE Trans. Antennas Propag.*, vol. 68, no. 9, pp. 6527-6537, Sept. 2020.

[10] H. Nawaz and I. Tekin, “Double-differential-fed, dual-polarized patch antenna with 90 dB interport RF isolation for a 2.4 GHz in-band full-duplex transceiver,” *IEEE Antennas Wireless Propag. Lett.*, vol. 17, no. 2, pp. 287–290, Feb. 2018.

[11] R. C. Paryani, P. F. Wahid, and N. Behdad, “A wideband, dual-polarized, substrate-integrated cavity-backed slot antenna,” *IEEE Antennas Wireless Propag. Lett.*, vol. 9,

pp. 645–648, Jul. 2010.

[12] R.-S. Chen *et al.*, "High-isolation in-band full-duplex cavity-backed slot antennas in a single resonant cavity," *IEEE Trans. Antennas Propag.*, vol. 69, no. 11, pp. 7092-7102, Nov. 2021.

[13] D. Kim, M. Zhang, J. Hirokawa, and M. Ando, “Design and fabrication of a dual-polarization waveguide slot array antenna with high isolation and high antenna efficiency for the 60 GHz band,” *IEEE Trans. Antennas Propag.,* vol. 62, no. 6, pp. 3019–3027, Jun. 2014.

[14] S.-G. Zhou, G.-L. Huang, T.-H. Chio, J.-J. Yang, and G. Wei, “Design of a wideband dual-polarization full-corporate waveguide feed antenna array,” *IEEE Trans. Antennas Propag.*, vol. 63, no. 11, pp. 4775–4782, Nov. 2015.

[15] W. Han, F. Yang, J. Ouyang and P. Yang, "Low-cost wideband and high-gain slotted cavity antenna using high-order modes for millimeter-wave application," *IEEE Trans. Antennas Propag.*, vol. 63, no. 11, pp. 4624-4631, Nov. 2015.

[16] Y. Wu, Z. Hao, W. Hong, and J. Hong, "A 140 GHz high-efficiency slotted waveguide antenna using a low-loss feeding network," *IEEE Antennas and Wireless Propag. Lett.*, vol. 19, no.1, pp. 94-98, Jan. 2020.

[17] Q. Yuan, Z. Hao, K. Fan and G. Q. Luo, "A compact *W*-band substrate-integrated cavity array antenna using high-order resonating modes," *IEEE Trans. Antennas Propag.*, vol. 66, no. 12, pp. 7400-7405, Dec. 2018.

[18] J.-Y. Lin, Y. Yang, S.-W. Wong, and Y. Li, “High-order modes analysis and its applications to dual-band dual-polarized filtering cavity slot arrays,” *IEEE Trans. Microw. Theory Techn.*, vol. 69, no. 6, pp. 3084-3092, Jun. 2021.

[19] R. H. Mahmud and M. J. Lancaster, "High-gain and wide-bandwidth filtering planar antenna array-based solely on resonators," *IEEE Trans. Antennas Propag.*, vol. 65, no. 5, pp. 2367-2375, May 2017.

[20] F. Chen, J. Chen, Q. Chu and M. J. Lancaster, "X-band waveguide filtering antenna array with nonuniform feed structure," *IEEE Trans. Microw. Theory Techn.*, vol. 65, no. 12, pp. 4843-4850, Dec. 2017.

[21] S.-W. Wong, J.-Y. Lin, Y. Yang, Z.-C. Guo, L. Zhu, and Q.-X. Chu, “Microwave waveguide components based on multiple-mode resonators,” *IEEE Microwave*

Magazine, vol. 22, no. 2, pp. 33-45, Feb. 2021.

[22] S.-W. Wong, J.-Y. Lin, Y. Yang, H. Zhu, R.-S. Chen, L. Zhu, and Y. He, “Cavity balanced and unbalanced diplexer based on triple-mode resonator,” *IEEE Trans. Ind. Electron.*, vol. 67, no. 6, pp. 4969-4979, June 2020.

[23] J.Y. Lin *et al.*, "Cavity filtering magic-T and its integrations into balanced-to-unbalanced power divider and duplexing power divider," *IEEE Trans. Microw. Theory Techn.*, vol. 67, no. 12, pp. 4995-5004, Dec. 2019.

[24] J.Y. Lin, S.W. Wong, L. Zhu and Q.X. Chu, "Design of miniaturized triplexers via sharing a single triple-mode cavity resonator," *IEEE Trans. Microw. Theory Techn.*, vol. 65, no. 10, pp. 3877-3884, Oct. 2017.

[25] J.Y. Lin, S.W. Wong, Y.M. Wu, Y. Yang, L. Zhu and Y. He, "Three-way multiple-mode cavity filtering crossover for narrowband and broadband applications," *IEEE Trans. Microw. Theory Techn.*, vol. 67, no. 3, pp. 896-905, Mar. 2019.

[26] J.-Y. Lin, S.-W. Wong and Y. Yang, "Filtering in-band full-duplex slot antenna based on TM_{120} and TM_{210} dual-mode resonators," *2021 IEEE MTT-S International Microwave Filter Workshop (IMFW)*, Perugia, Italy, 2021, pp. 249-251.

[27] S. Bastioli, C. Tomassoni and R. Sorrentino, "A new class of waveguide dual-mode filters using TM and nonresonating modes," *IEEE Trans. Microw. Theory Techn.*, vol. 58, no. 12, pp. 3909-3917, Dec. 2010.

[28] G. L. Matthaei, L. E. O. Young, and E. M. T. Jones, *Microwave Filters, and Coupling Structures*. NJ, USA: Artech House, 1985.

[29] J.-S. Hong and M. J. Lancaster, Microstrip Filters for RF/Microwave Applications. New York: Wiley, 2001.

[30] Y. Wu, Z. Hao, R. Lu and J. Hong, "A High-Selectivity D-Band Mixed-Mode Filter Based on the Coupled Overmode Cavities," *IEEE Trans. Microw. Theory Techn.*, vol. 68, no. 6, pp. 2331-2342, Jun. 2020.

Chapter 5 Two-Way Waveguide Diplexer and Its Application to Diplexing In-Band Full-Duplex Antenna

5.1 Introduction

Microwave transmission links usually reuse frequencies using polarization diversity. In particular, an in-band full-duplex (IBFD) communication system possesses the capacity of simultaneously transmitting/receiving dual-polarized signals. One of the best alternatives for this system includes a dual-polarized antenna, along with an orthomode transducer (OMT) [1]-[5]. The latter provides the required combination or separation of the orthogonally polarized signals [1]. The most common OMT structure consists of four branch ports and one common port with a square [2], [3], or a circular cross-section [4], [5].

Generally, IBFD systems require high isolation between two duplexing channels [6]-[11]. 16 × 16 dual-polarized antenna arrays are achieved in [8] and [9] with a realized gain of 32.3, 31.4 dBi and channel isolation of better than 52 dB, 40 dB, respectively. OMT-fed horn antenna in [11] achieves a peak gain of 11.7 dBi and an isolation of better than 45 dB throughout the operating band. Multiple-mode resonator (MMR) technology is an excellent candidate for designing high-isolation components [12]-[16] taking advantage of the modal orthogonality among different resonating modes. For example, two pairs of harmonic modes (HEE11 and HEH11) are used for two-way crossovers [12], the fundamental modes (TE_{011}, TM_{110} and TE_{101}) for triplexers [13], three-way crossovers [14], [15], and quadruple modes for four-way waveguide crossovers [16].

Furthermore, diplexing IBFD systems [17] require two more diplexers to comply with the interface of the OMT part. Conventionally, a waveguide twist is attached between the OMT and diplexer so that the whole structure is bulky and fabricating it is complicated. In [18], [19] for dual-polarized diplexer design, a Turnstile junction is implemented to achieve the impedance matching between the dual-polarized antenna and both diplexers, which serves to eliminate the OMT and twist parts. This miniaturizes the circuit size and avoids the complicated assembling process. However, there is no published literature on the diplexing IBFD frontend system, to the best of the author's knowledge.

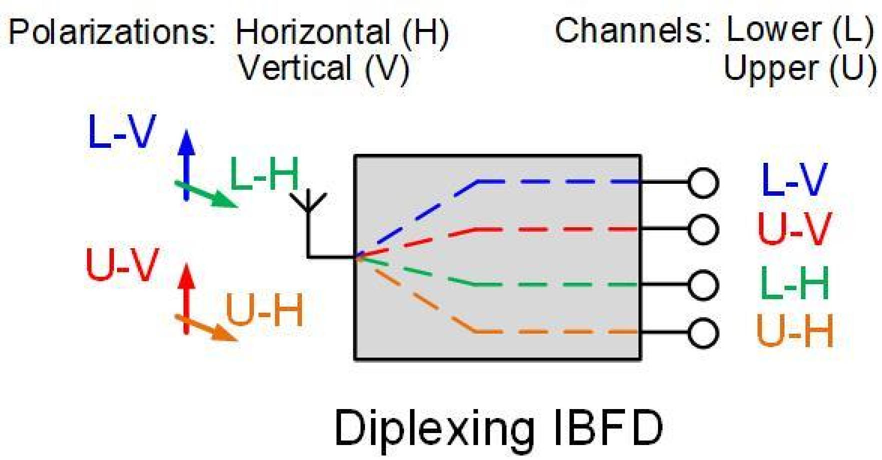

Fig. 5.1. Diagram of the proposed diplexing IBFD system.

To directly integrate multiple functions in a single element in the diplexing IBFD system, a diplexing IBFD antenna based on quadruple-mode resonators (QMRs) is presented in this paper. A diagram for this concept is shown in Fig. 5.1. Recent advances in the MMR technique confirm that it provides more design freedom to integrate multiple functions, as summarized in [20]. Using quadruple-mode resonator as a fundamental element, the proposed circuit integrates filtering, diplexing, orthomode transducing, and radiating functions. Firstly, a two-way waveguide diplexer integration is presented where two identical waveguide diplexers are integrated into a single circuit with negligible mutual interference. Each diplexer channel is dominated by four modes (TE_{011} and TE_{101} – fundamental modes, and TM_{210} and TM_{120} – high-order modes). Secondly, the proposed two-way diplexer does not require a matching network such as OMT or twist for the inputs and outputs since the channels of each diplexer share a common quadruple-mode resonator.

Furthermore, two diplexers share the same quadruple-mode resonators without interaction due to the modal orthogonality characteristic among the four modes in a quadruple-mode resonator. A 2nd-order diplexing IBFD antenna using a turnstile junction is proposed, fabricated, and tested based on this two-way waveguide diplexer. Two input ports of the two-way diplexer are combined into one radiating element. This element possesses two dual-polarized signals, horizontally (H^1 and H^2) and vertically (V^1 and V^2). Each signal can be dominated by the quadruple modes in the proposed quadruple-mode resonator.

5.2 Concept of Resonant Modes

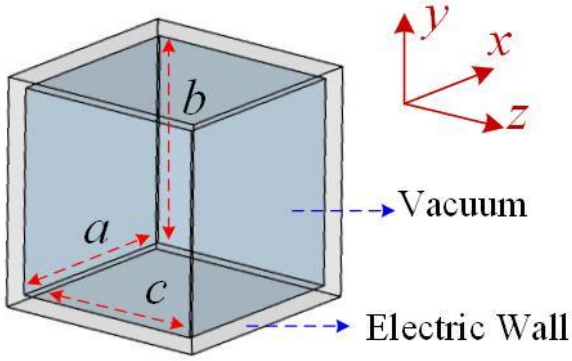

Fig. 5.2. Model of the multi-mode resonator in a single rectangular cavity.

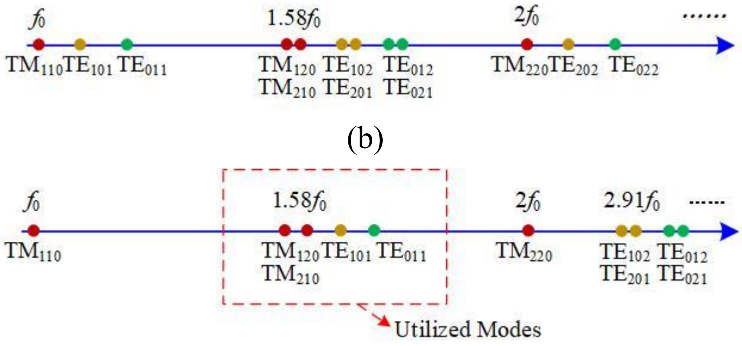

(b)

(c)

Fig. 5.3. Frequency sequence of fundamental, first- and second-order high-order modes. (a) Case of $a \approx b \approx c$, (b) Case of $c \approx 1/2b \approx 1/2a$.

Fig. 5.2 shows a rectangular waveguide cavity, of which the dimensions are represented by a, b and c. The resonant frequencies of the proposed rectangular waveguide modes can be expressed as:

$$\omega_{m,n,l}{}^{2}=\frac{v^2}{\varepsilon_r u_r}\left[\left(\frac{m\pi}{a}\right)^2+\left(\frac{n\pi}{b}\right)^2+\left(\frac{l\pi}{c}\right)^2\right] \tag{5-1}$$

When the values of length a, width b, and height c are close to each other, $a \approx b \approx c$, the sequence of the resonant modes can be shown as demonstrated in Fig. 3(a). Setting the resonant frequency of the first fundamental mode TE_{011} as f_0, the resonant frequencies of its first-order and second-order harmonic modes would be $1.58f_0$ and $2f_0$, respectively. Therefore, there are three fundamental modes TE_{011}, TE_{101} and TM_{110} at around frequency f_0, six first-order high-order modes TE_{012}, TE_{021}, TE_{102}, TE_{201}, TM_{120}

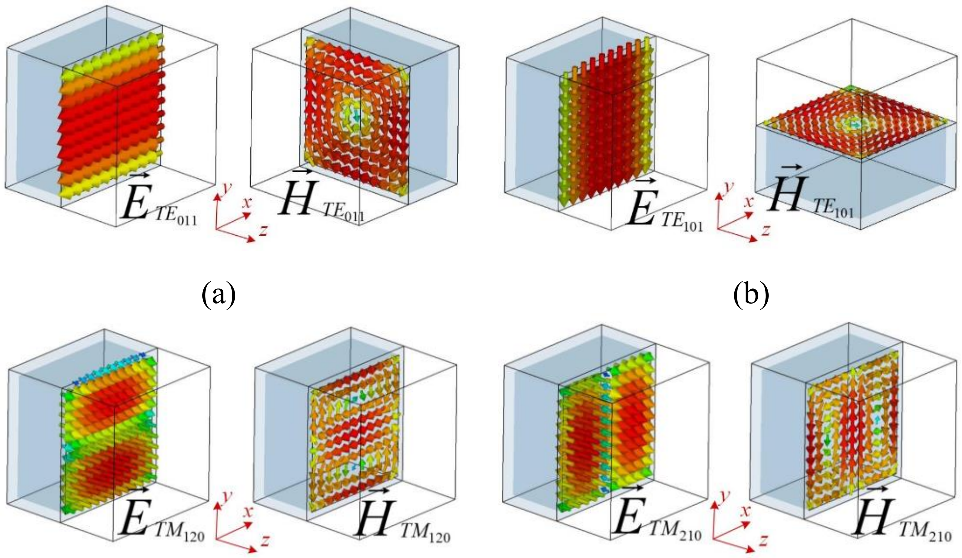

(a) (b)

(c) (d)

Fig. 5.4. The electromagnetic field distributions of quadruple modes in a cavity resonator. (a) TE_{011}, (b) TE_{101}, (c) TM_{120}, (d) TM_{210}.

and TM_{210} at around frequency $1.58f_0$, while three second-order high-order modes TE_{022}, TE_{202} and TM_{220} appear at around frequency $2f_0$. The higher-order harmonic modes are at a higher frequency range, which is not shown in Fig. 5.3.

When the value of height c is decreased, the resonant frequencies of TE_{101} and TE_{011} and their harmonic modes, determined by c, will move to a higher frequency range. As shown in Fig. 5.3(b), when it satisfies the condition that $c \approx 1/2b \approx 1/2a$, the resonator shows unchanged frequency points of TM_{110} and its harmonic modes, while the frequencies of TE_{101} and TE_{011} are shifted to around frequency $1.58f_0$, and their first-order high-order modes will locate at around frequency $2.91f_0$. Therefore, a pair of first-order high-order modes (TM_{120} and TM_{210}) and a pair of fundamental modes (TE_{011} and TE_{101}) are located around frequency $1.58f_0$, which can be independently controlled and placed within a frequency range [21], [22].

Fig. 5.4 presents the electromagnetic (EM) field distributions of the proposed quadruple modes in a single cavity resonator. By properly setting the location and orientation of the coupling slots, simultaneous or independent excitation and coupling of the resonant modes can be achieved in a single quadruple-mode resonator. The achieved Q_u values of quadruple modes TE_{011}, TE_{101}, TM_{120}, and TM_{210} are 7344, 7344, 7087, 7087, respectively.

5.3 2nd-Order Two-Way Waveguide Diplexer

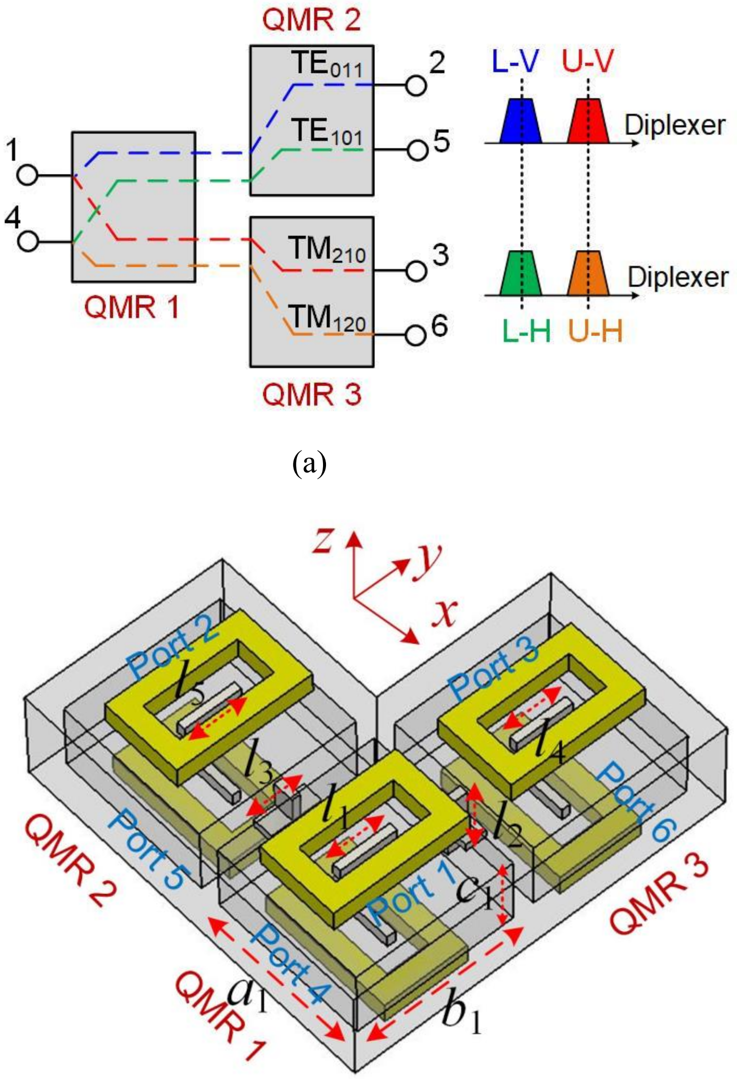

(a)

(b)

Fig. 5.5. A 2nd-order two-way waveguide diplexer prototype with: (a) Schematic, (b) Geometrical configuration.

A two-way waveguide diplexer is designed based on fundamental modes TE_{011}, TE_{101}, and a pair of first-order high-order modes TM_{120}, TM_{210} in a single quadruple-mode resonator. It can be regarded as the integration of two identical diplexers with one vertical diplexer and the other horizontal diplexer, as shown in the schematic depicted in Fig. 5.5(a). In the vertical diplexer, Port 1 excites TE_{011} and TM_{210} modes simultaneously. It excites TE_{011} mode resonated at the lower-band frequency L-V to port 2 while exciting TM_{210} mode at upper-band frequency U-V to port 3. In the

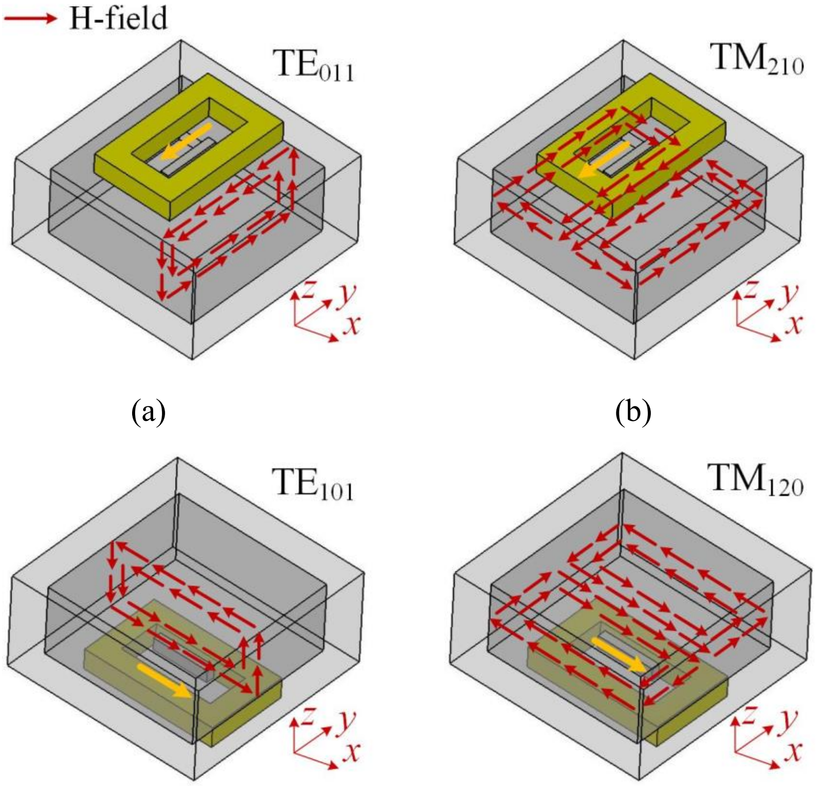

(a) (b)

(c) (d)

Fig. 5.6. H-field distributions of the four modes and the WR-90 arrangement in a single cavity. (a) TE$_{011}$, (b) TM$_{210}$, (c) TE$_{101}$, and (d) TM$_{120}$.

horizontal diplexer, Port 4 excites TE$_{101}$ and TM$_{120}$ modes simultaneously. It transmits TE$_{101}$ mode at lower-band frequency L-H to port 5, which has the same frequency as TE$_{011}$ mode, while it also transmits TM$_{120}$ mode at upper-band frequency U-H at the same frequency as TM$_{210}$ mode to port 6. Due to the modal orthogonality, high isolations among the output ports 2, 3, 5, and 6 are achieved.

A 2nd-order waveguide two-way diplexer prototype is shown in Fig. 5.5(b), which is composed of three quadruple-mode resonators and six WR-90 ports. Port 1, port 2 and port 3 are placed at the top center surface of each quadruple-mode resonator on the *xoy* plane with their long-edge orientations to the *y*-axis, while port 4, port 5 and port 6 are placed at the bottom center surface of each quadruple-mode resonator with their long-edge parallel to the *x*-axis, respectively. As depicted in Figs. 5.6(a)-(b), the WR-90 port (with the long edge parallel to the y-axis) generates TE$_{011}$ and TM$_{210}$ modes simultaneously since the H-field distribution corresponds with that of TE$_{011}$ and TM$_{210}$ modes. Similarly, the WR-90 port (long-edge parallel to the *x*-axis) can generate TE$_{101}$ and TM$_{120}$ modes due to H-field orientations. Therefore in Fig. 5.5(b), port 1, port 2,

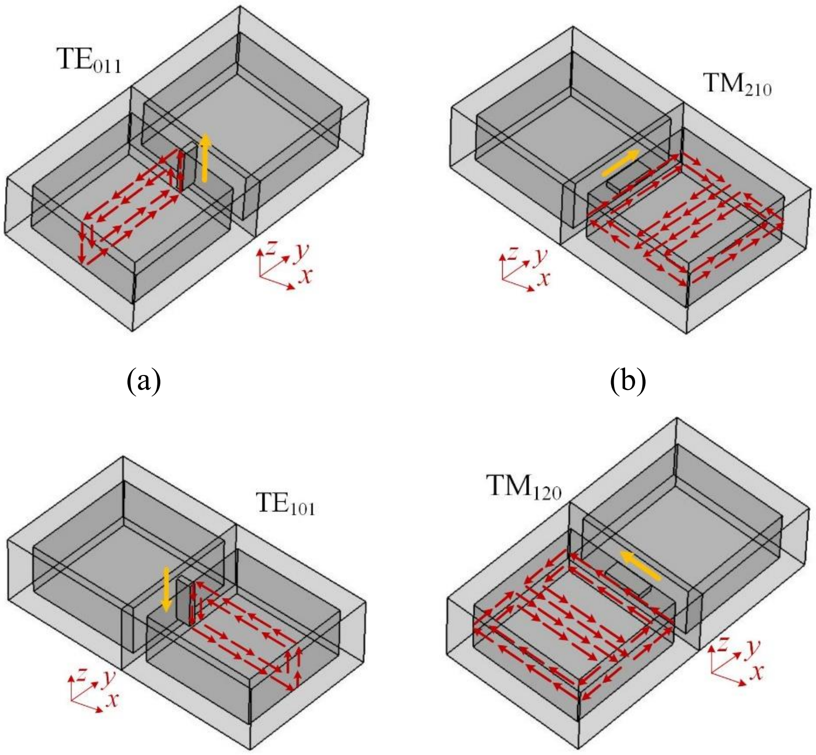

(a) (b)

(c) (d)

Fig. 5.7. H-field distributions of the four modes and the arrangement of a coupling slot between the two quadruple-mode resonators. (a) TE_{011}, (b) TM_{210}, (c) TE_{101}, (d) TM_{120}.

and port 3 can produce both TE_{011} and TM_{210} modes, while port 4, port 5 and port 6 can produce both TE_{101} and TM_{120} modes in their respective quadruple-mode resonators, respectively. To implement the schematic in Fig. 5.5(a), TM_{210} mode is prohibited from propagating between port 1 and port 2, while the TE_{011} mode is prohibited from propagating between port 1 and port 3. Similarly, TM_{120} mode is prohibited from propagating between port 4 and port 5, while TE_{101} mode is prohibited from propagating between port 4 and port 6. Therefore, in Fig. 5.7, the varied orientations of the coupling slots between quadruple-mode resonators control the transmission of the designated resonating modes.

It can be seen in Fig. 5.7(a) that a coupling slot is placed on the *xoz* plane with its long-edge parallel to the *z*-axis, so that the H-field orientation of this slot is corresponding only with that of TE_{011} mode; so it couples the EM energy of TE_{011} mode while prohibiting the signal transmission of the other three modes. Similarly, a coupling slot (long-edge parallel to the y-axis) is applied to couple TM_{210} mode in Fig. 5.7(b). In contrast, two coupling slots (long-edge parallel to the z-axis and x-axis, respectively) are applied to couple TE_{101} mode in Fig. 5.7(c), and TM_{120} mode in Fig. 5.7(d), respectively. Finally, as shown in Fig. 5.5(b), two cross-coupled slots are placed between the two quadruple-mode resonators to control the coupling coefficient (K) of both channels at L-V and U-V. In contrast, two cross-coupled slots are placed between quadruple-mode resonators 1 and 3 to control K of both channels at L-H and U-H.

Since both diplexers in the proposed prototype are completely identical without coupling in between, each one's frequency responses are identical. We take the diplexer with port 4, port 5, and port 6 as an example for discussion. Setting the center frequencies of f_1=8.61 GHz and f_2=9.43 GHz, 3-dB fractional bandwidths (FBWs) of 0.9% and 1.1%, and a ripple level of better than 0.2 dB, the external quality factors Q_e and K of a 2nd-order Butterworth response can be expressed as:

$$Q_e = \frac{g_0 g_1}{FBW} \tag{5-2a}$$

$$K_{12} = \frac{FBW}{\sqrt{g_1 g_2}} \tag{5-2b}$$

where g_0= g_3=1 and g_1=g_2=1.4142 [23], based on which we can obtain Q_e=141.42 and K_{12}=0.007.

In the inset of Fig. 5.8(a), the length l_1 and the width w_1 of the slot between a quadruple-mode resonator and the WR-90 port are used to control Q_e of both TE_{101} and TM_{120} modes from the feeding port to the structure. Q_e is expressed as [24]:

$$Q_e = \frac{2\pi f_0 \tau_{s11}(f_0)}{4} \tag{5-3}$$

where $\tau_{s11}(f_0)$ is the group delay at f_0. It can be deduced in Fig. 5.8(a) that both length l_1 and width w_1 have similar effects on Q_e values of the TE_{101} and TM_{120} modes. When l_1 and w_1 are bigger, Q_e values of TE_{101} and TM_{120} will be smaller.

Meanwhile, K of the TE_{101} mode is controlled by the length l_2 and the width w_2 of the slot between two quadruple-mode resonators as shown in the inset of Fig. 5.8(b). K is expressed as [24]:

$$K = \frac{f_{p2}^2 - f_{p1}^2}{f_{p2}^2 + f_{p1}^2} \tag{5-4}$$

where f_{p1}, and f_{p2} are the two resonant peaks. It can be deduced from what is shown in

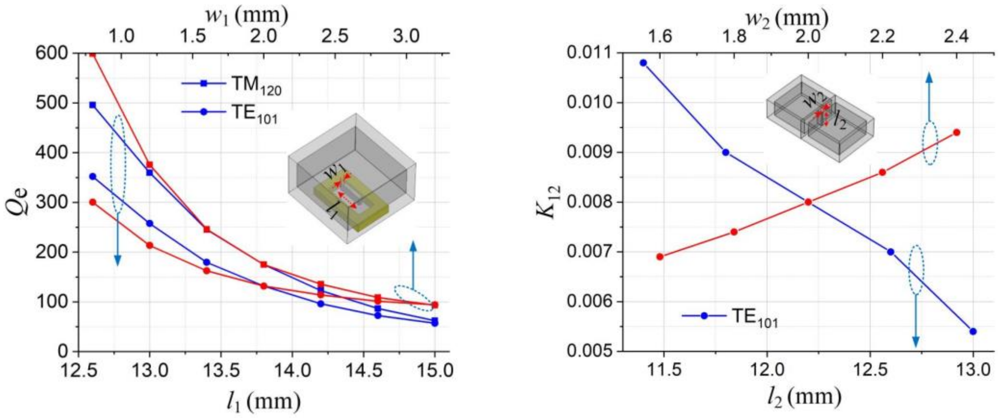

(a) (b)

Fig. 5.8. Variation of (a) Q_e value versus length l_1 and width w_1, (b) K value versus length l_2 and width w_2.

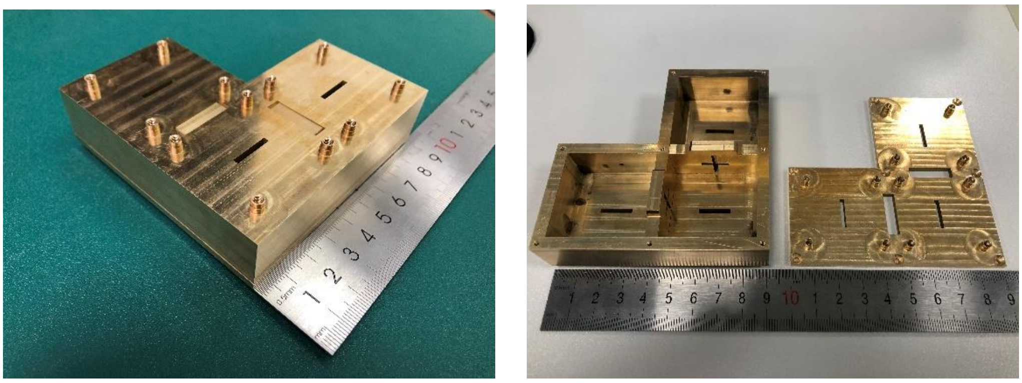

(a) (b)

Fig. 5.9. Photographs of the manufactured 2nd-order two-way diplexer prototype: (a) External view, (b) Internal view.

Fig. 8(b) that the smaller length l_2 or bigger w_2 will result in a bigger K of TE$_{101}$ mode.

Figs. 5.9(a)-(b) illustrate the external and internal view of the proposed manufactured model. It is made of brass using Computer Numerical Control (CNC) technology.

Since the two implemented diplexing functions of the proposed two-way diplexer prototype are completely identical, the S-parameters for port 1 will be the same as port 4. Therefore, the S-parameters for the first diplexer, port 1, port 2 and port 3, are shown in Fig. 5.10. The downlink channel resonates at 8.61 GHz with a measured insertion loss of 0.8 dB and an 80 MHz 3-dB bandwidth. The uplink channel resonates at 9.43 GHz with a measured insertion loss of 0.5 dB and a 100 MHz 3-dB bandwidth. It can be seen in Fig. 5.10(b) that port 1 is isolated from port 4, port 5, and port 6. The minimum isolation (from 8.4 GHz to 9.8 GHz) for $|S_{41}|$, $|S_{51}|$, and $|S_{61}|$ can reach -25 dB, -25 dB, and -33 dB, respectively. Fig. 5.10(c) and (d) show the S-parameters at port

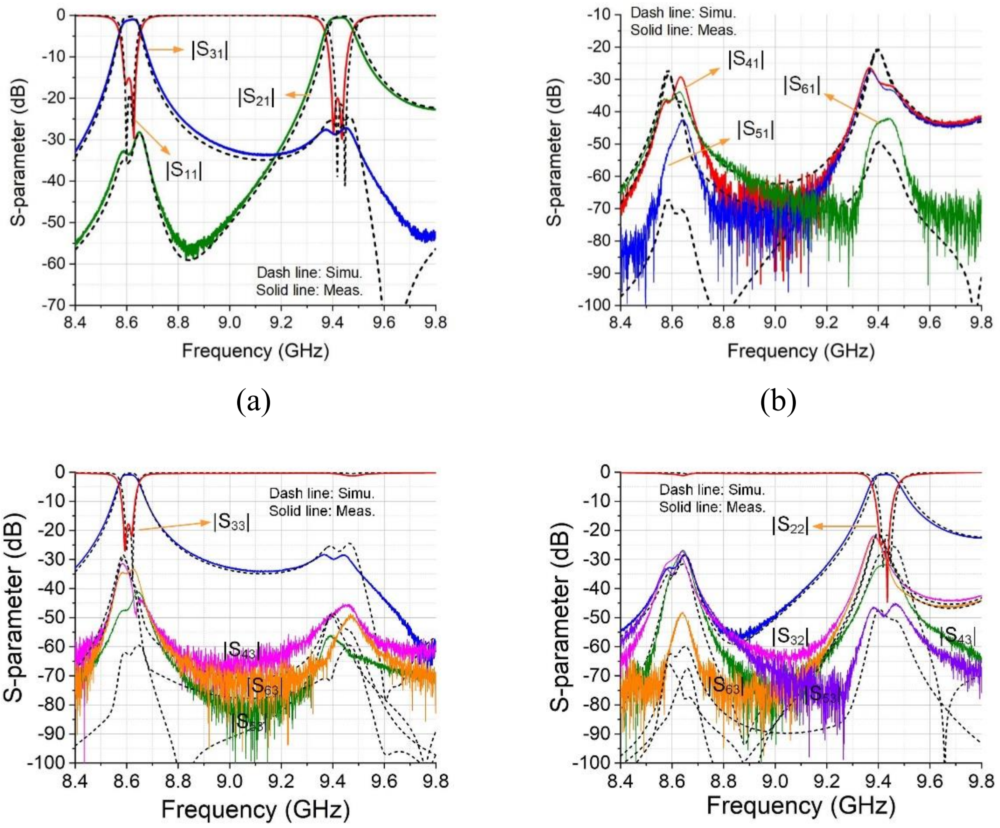

(a) (b)

(c) (d)

Fig. 5.10. Comparison between the simulated and measured S-parameters of the 2nd-order two-way diplexer prototype for: (a)-(b) port 1, (c) port 3, (d) port 2.

3 and port 2, respectively. The isolation level to other ports, i.e., $|S_{32}|$, $|S_{42}|$, $|S_{52}|$, $|S_{62}|$, $|S_{43}|$, $|S_{53}|$ and $|S_{63}|$, are all better than 22 dB, respectively. In each diplexer, the isolation level between two channels can be improved by expanding the two channels' frequency ratio.

The physical dimensions are elaborately optimized, as shown in Table 5.1. All widths and thicknesses of the slots are set to 2 mm and 3 mm, respectively.

TABLE 5.1

PHYSICAL DIMENSIONS OF PROPOSED TWO-WAY WAVEGUIDE DIPLEXER (UNIT: MM)

$a_1 = 38$	$b_1 = 38$	$c_1 = 17$	$l_1 = 13.8$
$l_2 = 14.8$	$l_3 = 12.2$	$l_4 = 13.8$	$l_5 = 13.8$

5.4. 2nd-Order Diplexing IBFD Antenna

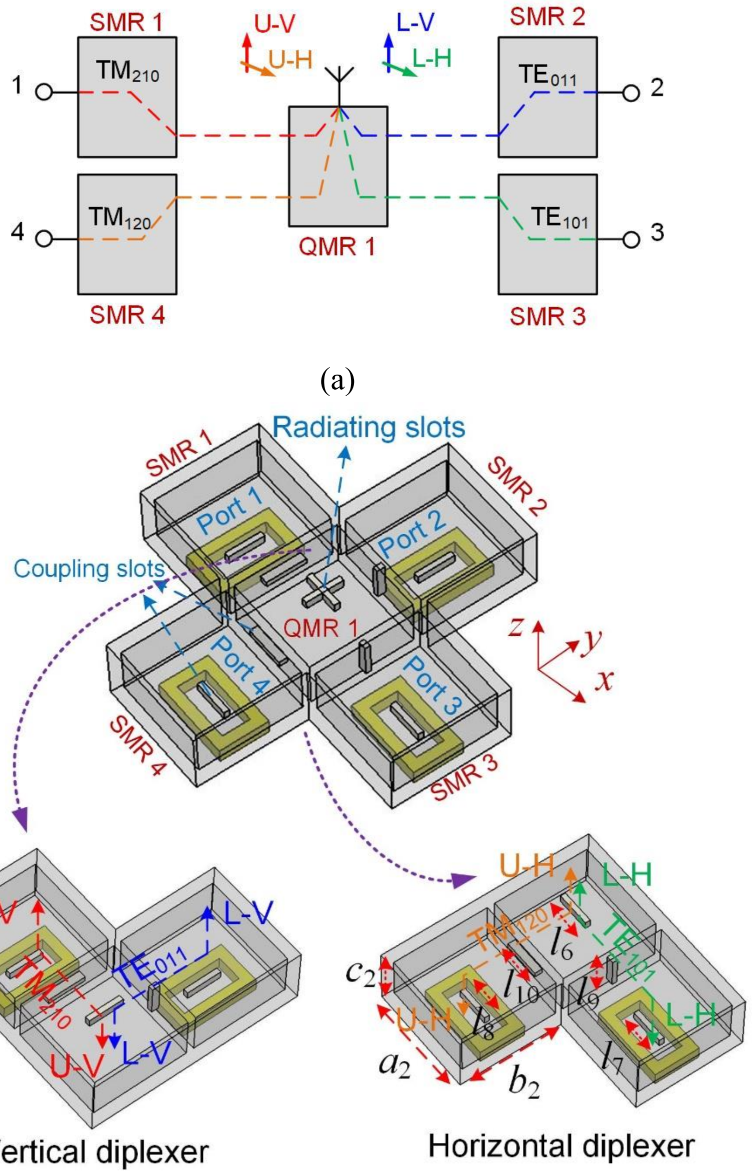

(a)

(b)

Fig. 5.11. A 2nd-order diplexing IBFD antenna prototype with: (a) Schematic, (b) Geometrical configuration with vertical diplexer part and horizontal diplexer part.

This section presents a 2nd-order duplexing IBFD slot antenna based on the two-way waveguide diplexer, as shown in Fig. 5.11(a). Two common input ports 1 and 4 are combined into a common radiating element compared with a two-way waveguide diplexer. It can possess two pairs of dual-polarized signals, horizontally (H^1 and H^2) and vertically (V^1 and V^2). Each signal can be dominated by the quadruple modes in the proposed quadruple-mode resonator, respectively. Therefore, the proposed two-way

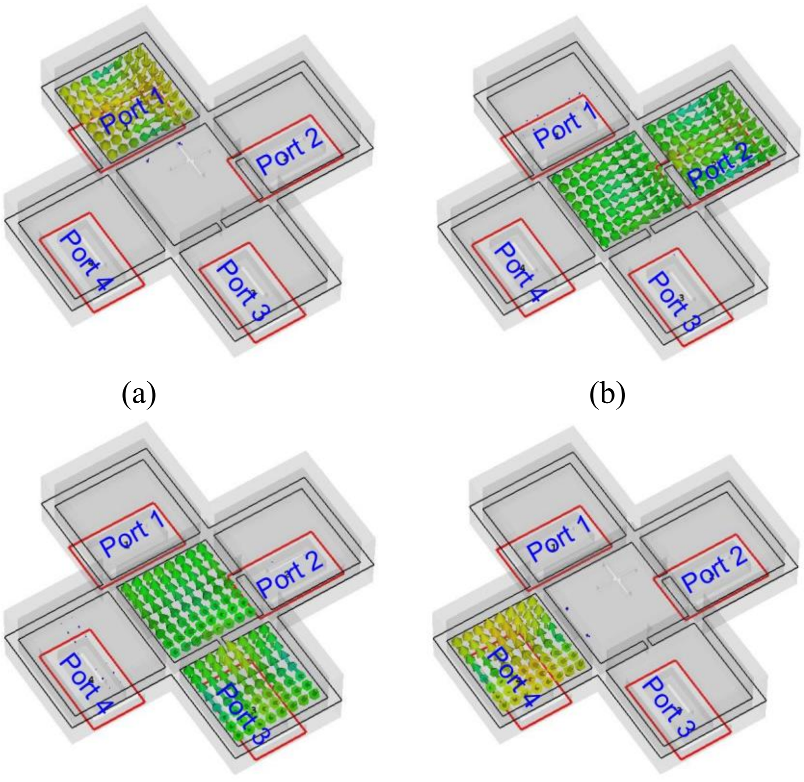

(a) (b) (c) (d)

Fig. 5.12. H-field distributions of proposed design at 8.6 GHz with: (a) port 1 excitation, (b) port 2 excitation, (c) port 3 excitation, (d) port 4 excitation.

waveguide diplexer is converted into a vertical one and a horizontal one, respectively. The downlink channels of both diplexers have the same frequency with orthogonal signals L-V and L-H, while the uplink channels of both diplexers resonate with orthogonal signals U-V and U-H.

The geometry of the 2nd-order diplexing IBFD antenna prototype is shown in Fig. 5.11(b). It consists of one quadruple-mode resonator, four single-mode-resonator (SMR) cavities, and four WR-90 ports. Four quadruple-mode resonators surround the quadruple-mode resonator by using a turnstile junction. A pair of cross-coupled radiating slots implements the single radiating element. It can be regarded as a combination of two identical diplexing antennas. Referring to the vertical diplexing antenna, the radiating slot with its long-edge parallel to the *y*-axis is used to simultaneously transmit/receive the L-V and U-V signals. The U-V signal is dominated by the TM_{210} mode and transmitted between the radiating slot and port 1.

In contrast, the L-V signal is dominated by the TE_{011} mode and transmitted between the radiating slot and port 2. Similarly, in the horizontal diplexing antenna, the radiating slot with its long-edge parallel to the *x*-axis controls V-H and U-H signals. The U-H

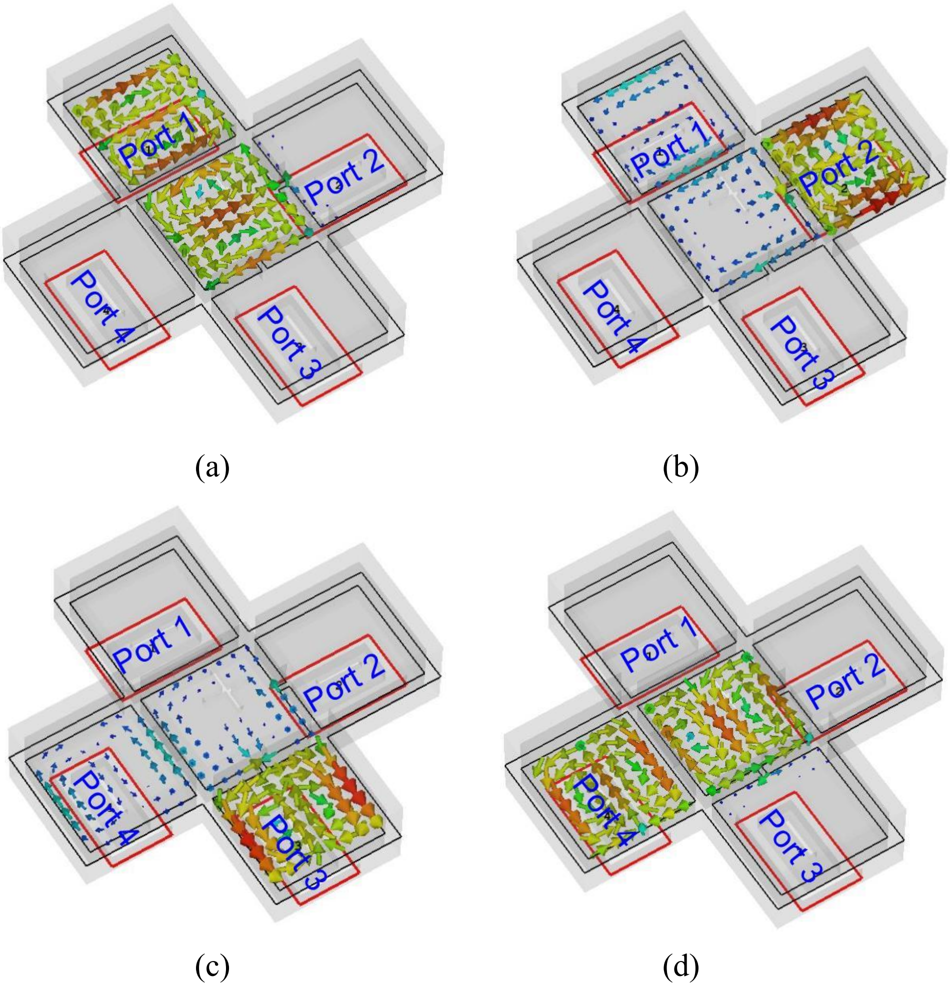

(a) (b)

(c) (d)

Fig. 5.13. H-field distributions of proposed design at 9.4 GHz with: (a) port 1 excitation, (b) port 2 excitation, (c) port 3 excitation, (d) port 4 excitation.

signal is dominated by the TM_{120} mode at port 4, while the TE_{101} mode at port 3 dominates the L-H signal.

Figs. 5.12(a)-(d) present the H-field distributions for all the ports at the 8.6 GHz downlink channel. As can be observed in Figs. 5.12(a) and (d), the EM energies excited at port 1 and port 4 are trapped in SMR cavities 1 and 4, respectively. They cannot propagate through the radiating slot due to the orientation of the coupling slot between quadruple-mode resonator and single-mode resonator. In Figs. 5.12(b)-(c), EM energies at port 2 and port 3 can be propagated into the radiating slot to form L-V and L-H signals, respectively. Similarly, at 9.4 GHz uplink channel, as shown in Figs. 5.13(b)-(c), most EM energies excited at port 2 and port 3 are trapped in SMR cavities 2 and 3, respectively. Consequently, minimal energy can be coupled into the radiating slot. Meanwhile in Figs. 5.13(a) and 5.13(d), EM energy at port 1 and port 4 can be coupled into the radiating slot to form U-V and U-H signals. It is evident that each of the two

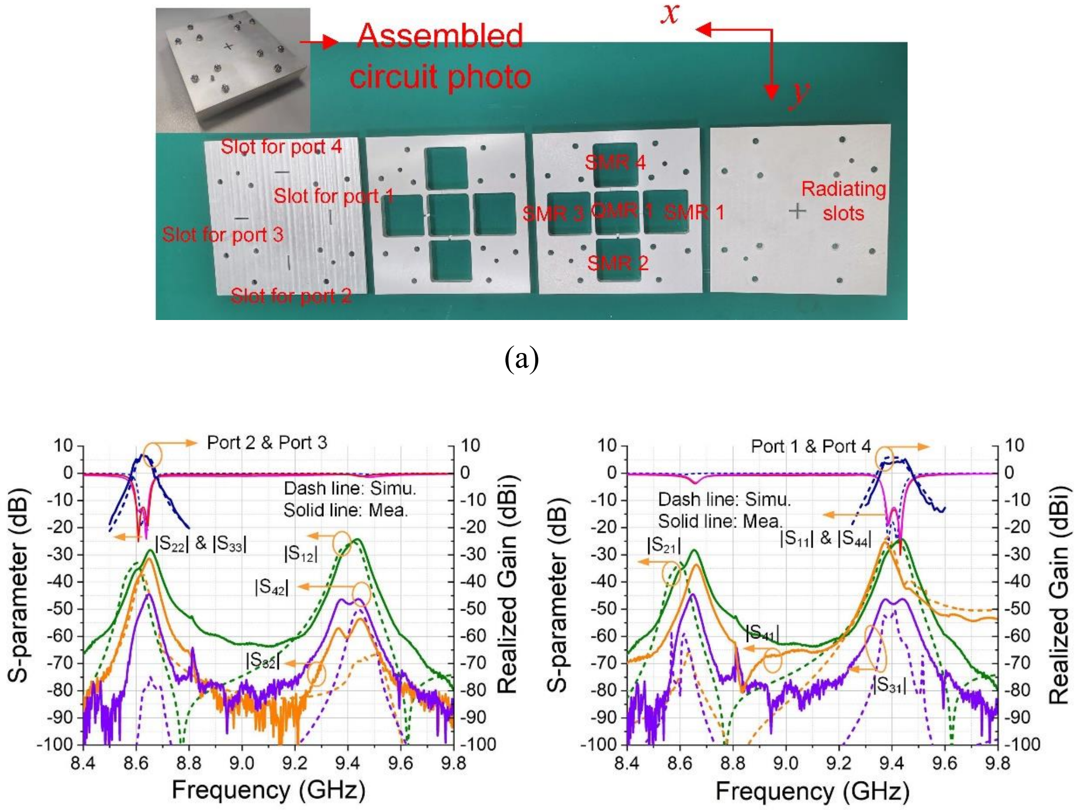

(a)

(b) (c)

Fig. 5.14. Diplexing IBFD antenna with: (a) Photos of the fabricated prototype, realized gains and S-parameters in simulation and measurement at (b) port 2 and (c) port 1.

pairs of dual-polarized signals is independently controlled by each of the quadruple modes in the proposed quadruple-mode resonator.

Figs. 5.14(a) presents a photo of the diplexing IBFD antenna prototype with four assembled silver-plated brass layers. Figs. 5.14(b)-(c) show the realized gains and measured S-parameters at port 2 and port 1, along with the corresponding simulation. $|S_{22}|$ dominated by TE_{011} mode and $|S_{33}|$ dominated by TE_{101} mode resonate at the same frequency of 8.62 GHz with a 70 MHz 10-dB bandwidth. In contrast, $|S_{11}|$ dominated by TM_{210} mode and $|S_{44}|$ dominated by TM_{120} mode resonate at the same frequency of 9.4 GHz with a 100 MHz 10-dB bandwidth. The measured realized gains for port 2 and port 3 are flat within the passband with the achieved peak gain of 6.5 dBi, while the measured peak gains for port 1 and port 4 are 4.5 dBi. For each diplexing function, the isolation level between output ports $|S_{12}|$ and $|S_{43}|$ are the same. The isolation is better than 22.5 dB within the 8.4 GHz to 9.8 GHz frequency range. The downlink channel isolation $|S_{32}|$ is better than 30 dB for each OMT function, while the uplink channel

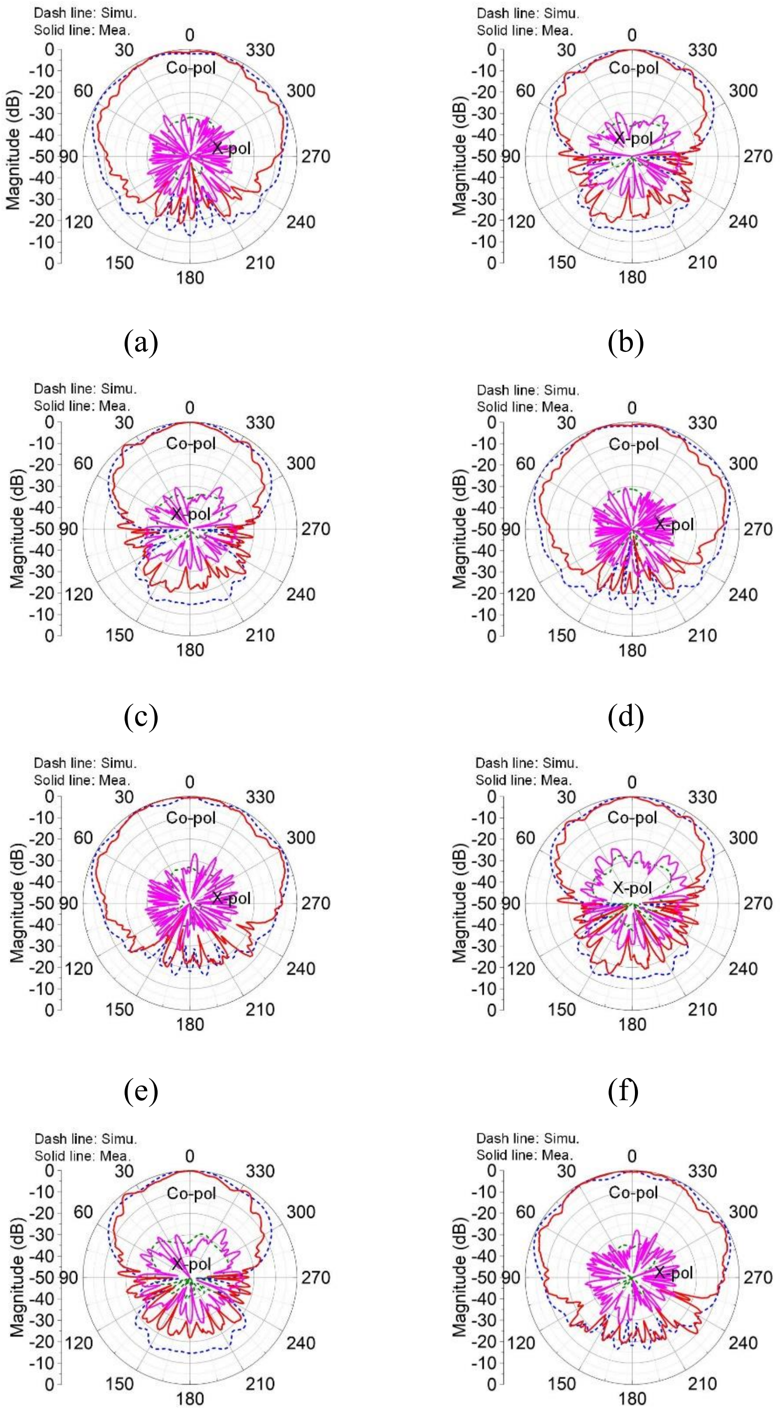

(a) (b)

(c) (d)

(e) (f)

(g) (h)

Fig. 5.15. Simulated and measured radiation patterns at 8.6 GHz: (a) Port 2 at *xoz* plane, (b) Port 2 at *yoz* plane, (c) Port 3 at *xoz* plane, (d) Port 3 at *yoz* plane, and at 9.4 GHz: (e) Port 1 at *xoz* plane, (f) Port 1 at *yoz* plane, (g) Port 4 at *xoz* plane, (h) Port 4 at *yoz* plane.

isolation $|S_{41}|$ is superior to 26 dB. The isolation level $|S_{31}|$ and $|S_{42}|$ are the same, better than 45 dB. Figs. 5.15(a)-(h) show the simulated and measured radiation patterns at 8.6 GHz (port 2 and port 3), and 9.4 GHz (port 1 and port 4), respectively. Since port 2 and port 3 form a dual-polarized function at the downlink channel, the radiation pattern at *xoz* plane for port 2 is similar to that at *yoz* plane for port 3 with the measured cross-polarization of 27 dB. The radiation pattern at *yoz* plane for port 2 is similar to that at *xoz* plane for port 3 with the measured cross-polarization of 25 dB. Similarly, we can obtain the same radiation patterns at port 1 and port 4. They achieve the cross-polarization of 26 dB and 25 dB, respectively.

Table 5.2 shows the dimensions of the proposed duplexing IBFD antennas. The slots widths and thickness are all set to 2 mm and 3 mm, respectively.

TABLE 5.2
PHYSICAL DIMENSIONS OF PROPOSED DIPLEXING IBFD ANTENNAS (UNIT: MM)

$a_2 = 38$	$b_2 = 38$	$c_2 = 17$	$l_6 = 13.8$
$l_7 = 13.8$	$l_8 = 13.8$	$l_9 = 13.8$	$l_{10} = 10.4$

5.5. Conclusion

In this chapter, the characteristics and EM properties of quadruple modes, namely TE_{011}, TE_{101}, TM_{120}, and TM_{210}, in a quadruple-mode resonator cavity are investigated and summarized. Based on the proposed quadruple-mode resonator, a two-way waveguide diplexer and a diplexing IBFD antenna are designed, fabricated, and tested. The isolation level among the channels can be achieved using the modal orthogonality of quadruple modes. In the diplexing IBFD antenna design, the two common input ports in the two-way diplexer are combined with cross-shaped radiating slots, acting as the horizontal port (H-port) and the vertical port (V-port) in the OMT function, while each port dominates both channels in the diplexer function. The proposed designs integrate multiple diplexing channels into a single device, significantly reducing the transceiver hardware volume and simplifying the design methodology. Revealed here are potential applications in the waveguide dual-band dual-polarized wireless communication systems.

5.6 References

[1] K. Tomiyasu, "Mitigation of rain and ice particle cross polarization at RF for dual circularly polarized waves," *IEEE Trans. Antennas Propag.*, vol. 46, no. 9, pp. 1379-1385, Sep. 1998.

[2] J. Esteban and C. Camacho-Peñalosa, "Compact orthomode transducer polarizer based on a tilted-waveguide T-junction," *IEEE Trans. Microw. Theory Techn.,* vol. 63, no. 10, pp. 3208-3217, Oct. 2015.

[3] M. Esquius-Morote, M. Mattes and J. R. Mosig, "Orthomode transducer and dual-polarized horn antenna in substrate integrated technology," *IEEE Trans. Antennas Propag.*, vol. 62, no. 10, pp. 4935-4944, Oct. 2014.

[4] D. Dousset, S. Claude and K. Wu, "A compact high-performance orthomode transducer for the Atacama large millimeter array (ALMA) band 1 (31–45 GHz)," *IEEE Access*, vol. 1, pp. 480-487, 2013.

[5] J. Shen and D. S. Ricketts, "Compact W-band “Swan Neck” turnstile junction orthomode transducer implemented by 3-D printing," *IEEE Trans. Microw. Theory Techn.,* vol. 68, no. 8, pp. 3408-3417, Aug. 2020.

[6] H. Nawaz and I. Tekin, “Double-differential-fed, dual-polarized patch antenna with 90 dB interport RF isolation for a 2.4 GHz in-band full-duplex transceiver,” *IEEE Antennas Wireless Propag. Lett.*, vol. 17, no. 2, pp. 287–290, Feb. 2018.

[7] R.-S. Chen *et al.*, "High-isolation in-band full-duplex cavity-backed slot antennas in a single resonant cavity," *IEEE Trans. Antennas Propag.*, vol. 69, no. 11, pp. 7092-7102, Nov. 2021.

[8] D. Kim, M. Zhang, J. Hirokawa, and M. Ando, “Design and fabrication of a dual-polarization waveguide slot array antenna with high isolation and high antenna efficiency for the 60 GHz band,” *IEEE Trans. Antennas Propag.,* vol. 62, no. 6, pp. 3019–3027, Jun. 2014.

[9] S.-G. Zhou, G.-L. Huang, T.-H. Chio, J.-J. Yang, and G. Wei, “Design of a wideband dual-polarization full-corporate waveguide feed antenna array,” *IEEE Trans. Antennas Propag.*, vol. 63, no. 11, pp. 4775–4782, Nov. 2015.

[10] D. Cao, Y. Li, J. Wang, F. Sun and L. Ge, "Millimeter-wave three-dimensional substrate-integrated OMT-fed horn antenna using vertical and planar groove gap waveguides," *IEEE Trans. Microw. Theory Techn.,* vol. 69, no. 10, pp. 4448-4459, Oct. 2021.

[11] F. Sun *et al.*, "A Millimeter-wave wideband dual-polarized antenna array with 3D-printed air-filled differential feeding cavities," in press on *IEEE Trans. Antennas Propag.*, 2022.

[12] J. Xu and X. Y. Zhang, "Dual-channel dielectric resonator filter and its application to doherty power amplifier for 5G massive MIMO system," *IEEE Trans. Microw. Theory Techn.*, vol. 66, no. 7, pp. 3297-3305, Jul. 2018.

[13] J.-Y. Lin, S.W. Wong, L. Zhu and Q.X. Chu, "Design of miniaturized triplexers via sharing a single triple-mode cavity resonator," *IEEE Trans. Microw. Theory Techn.*, vol. 65, no. 10, pp. 3877-3884, Oct. 2017.

[14] J.Y. Lin, S.W. Wong, Y.M. Wu, Y. Yang, L. Zhu and Y. He, "Three-way multiple-mode cavity filtering crossover for narrowband and broadband applications," *IEEE Trans. Microw. Theory Techn.*, vol. 67, no. 3, pp. 896-905, Mar. 2019.

[15] J. Xu, X. Y. Zhang, H. Li, Y. Yang, E. Dutkiewicz and Q. Xue, "Ultracompact multichannel bandpass filter based on trimode dielectric-loaded cavities," *IEEE Trans. Microw. Theory Techn.*, vol. 68, no. 5, pp. 1668-1677, May 2020.

[16] J. Y. Lin, Y. Yang, and S. W. Wong, "Four-way filtering crossover based on quadruple-mode cavity resontor," *2021 IEEE MTT-S International Microwave Symposium (IMS)*, Atlanta, GA, 2021, pp. 1-3.

[17] R. Garcia, F. Mayol, J. M. Montero and A. Culebras, "Circular polarization feed with dual-frequency OMT-based turnstile junction," *IEEE Antennas and Propag. Magazine*, vol. 53, no. 1, pp. 226-236, Feb. 2011.

[18] J. R. Montejo-Garai *et al.*, "Modelling of dual-polarisation diplexers based on enhanced multiport turnstile junctions," *IET Microw., Antennas Propag.*, vol. 7, no. 7, pp. 485-492, 2013.

[19] Q. Wu, F. Yang, Y. Yang and X. Shi, "Dual-polarized diplexer using turnstile junction," *IEEE Trans. Microw. Theory Techn.*, vol. 69, no. 8, pp. 3804-3810, Aug. 2021.

[20] S.-W. Wong, J.-Y. Lin, Y. Yang, Z.-C. Guo, L. Zhu, and Q.-X. Chu, “Microwave waveguide components based on multiple-mode resonators,” *IEEE Microwave Magazine*, vol. 22, no. 2, pp. 33-45, Feb. 2021.

[21] C. Tomassoni, S. Bastioli and R. Sorrentino, "Generalized TM dual-mode cavity filters," *IEEE Trans. Microw. Theory Techn.*, vol. 59, no. 12, pp. 3338-3346, Dec. 2011.

[22] G. Basavarajappa and R. R. Mansour, "A high-*Q* quadruple-mode rectangular waveguide resonator," *IEEE Microw. Wireless Compon. Lett.*, vol. 29, no. 5, pp. 324-326, May 2019.

[23] G. L. Matthaei, L. E. O. Young, and E. M. T. Jones, *Microwave Filters, and Coupling Structures*. NJ, USA: Artech House, 1985.

[24] J.-S. Hong and M. J. Lancaster, Microstrip Filters for RF/Microwave Applications. New York: Wiley, 2001.

Chapter 6 Inline Waveguide Bandpass Filter Using Bandstop Resonator Pairs

6.1 Introduction

Recently, the terahertz (THz) frequency region has attracted much attention due to its broadband spectrum, high spatial, and temporal resolution. As an essential component of the front-ends in the THz systems, the bandpass filter (BPF) [1]-[8] with high selectivity and low insertion loss is highly desirable. To achieve very sharp rejection skirts, transmission zeroes (TZs) are usually generated beside the passband. There are several well-established techniques to realize the generation of TZs, i.e., the cross-coupling between nonadjacent resonators [9]-[12], transversal topology based on multiple-mode resonators (MMRs) [13]-[16], cascaded singlets [17]-[20], and the extracted pole technique [21]-[25]. For the cross-coupling technique, the generated TZs are very sensitive and not easy to control, which will degrade the electrical performance. For the MMR technique, it is hard to excite multiple modes simultaneously in a single cavity, and the coupling between MMRs is very complex and still a challenge for designers to solve. Cascaded singlets and extracted pole filters can successfully generate TZs by using bypass coupling or dangling the resonators, and each TZ can be controlled independently since it is uniquely linked to the frequency of the resonator. However, the whole circuit layout would become large when oversized H-plane resonators are used.

Another candidate is a dual-band bandstop filter (DBBSF) having reciprocal frequency characteristics of a BPF. Generally, a bandstop filter (BSF) [26]-[29] has lower transmission loss and group-delay variation than a BPF since the resonators in the BSF resonate at the rejection band, but not at the passband. The DBBSF concept is originally from [30], and there are mainly two approaches to synthesize the DBBSF. One method is to apply the frequency-variable transformations to a low-pass filter [30]-[32]. The other one is based on the cul-de-sac configuration and the coupling matrix [33], [34]. They are all based on high unloaded quality factor (Q_u) bandstop resonators, which results in narrow bandwidths of dual stopbands. Meanwhile, the order number of DBBSF cannot produce the same number of reflection zeroes (RZs) in the passband. For this reason, they are not suitable for the BPF design because of the limited out-of-band rejection and different synthesis procedure. Recently, an E-plane BPF [35] was designed by introducing transmission zero resonator pair, a 2nd-order BPF at 33 GHz with 6% fractional bandwidth (FBW) and four TZs is measured. However, inserting a microstrip into the waveguide will degrade the Q_u of the waveguide and introduce the conductor and dielectric loss.

In this paper, a very compact waveguide BPF resonating at 250 GHz is designed based on two pairs of BSF elements to determine the lower and upper stopbands, respectively. They are based on E-plane stubs to miniaturize the whole circuit volume. Compared with the conventional dual-band BSF designs [30]-[34], two pairs of BSF elements are coupled in parallel to source and load, so they can be independently controlled and apply to LPF to single-band BSF transformation, respectively. Since the Q_u of E-plane stubs can be varied for a wide range, the narrowband and wideband performance of the proposed BPF are also presented. Finally, a 5th-order BPF with 10.9% FBW is fabricated and measured. The advantages of the proposed waveguide BPF are as follows. Firstly, there is a very compact size with the utilization of E-plane stubs. Secondly, simplified design procedure, easy fabrication, and flexible bandwidth are achievable. Dual stopbands can be controlled independently, and they follow the filtering function with lowpass filter (LPF) to BSF transformation, respectively. Narrow-band or wideband performance can be realized employing different resonant modes in the E-plane stubs. Thirdly, insertion loss is reduced since the resonators in the design resonate at the rejection band instead of the passband. Fourthly, multiple TZ generation is possible. Up to $2N$ TZs can be generated beside the passband in the Nth-order filter design.

6.2 Circuit Analysis of Proposed Bandpass Filter

The proposed BPF equivalent circuit is shown in Fig. 6.1, where two groups of BSF elements are connected in parallel and terminated by input and output admittance. Since there is no coupling between two groups of BSF elements, they can be independently controlled and each of them follows the frequency-variable transformation to the LPF to conduct the lower stopband and upper stopband, respectively. When the order number n of proposed BPF is set, unlike the previous DBBSF designs [30]-[34] which require $2n$ order number, a nth-order lower-band single-band BSF and a nth-order upper-band single-band BSF are required in the proposed synthesis.

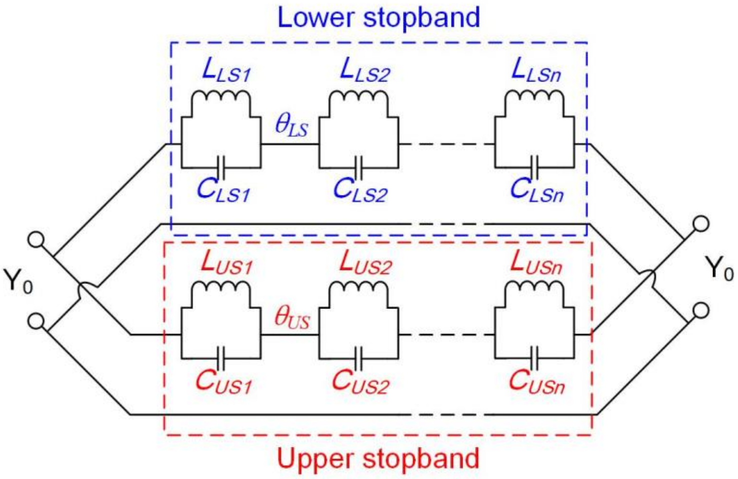

Fig. 6.1. Proposed BPF equivalent circuit. (*n* equals the order number of BPF.)

The circuit synthesis for a single-band BSF is conducted taking an example of the lower stopband BSF in Fig. 6.1. By applying frequency-variable transformation to the LPF,

$$\omega \to -\Delta_{LS}\left(\frac{\omega}{\omega_{LS}} - \frac{\omega_{LS}}{\omega}\right)^{-1}, \quad \Delta_{LS} = \frac{\omega_{LS2} - \omega_{LS1}}{\omega_{LS}} \tag{6-1}$$

Where ω_{LS}, ω_{LS1} and ω_{LS2} represent center frequency, left edge, and right edge of the stopband. $\omega_{LS} = \sqrt{\omega_{LS1}\omega_{LS2}}$ is chosen for equation simplification.

When inductive input low-pass prototype filter is adopted, the series inductors of the low-pass prototype are converted to parallel *LC* circuits having element values given by:

$$L_{LSi} = \frac{\Delta_{LS} g_{LSi}}{Y_0 \omega_{LS}} \tag{6-2a}$$

$$C_{LSi} = \frac{Y_0}{\omega_{LS} \Delta_{LS} g_{LSi}} \tag{6-2b}$$

Where g_{LSi} denotes the *i*th-order element value of the prototype filter, and Y_0 stands for the input and output admittance.

In the proposed BPF with a center frequency of ω_0, left edge and right edge frequencies of the 3-dB bandwidth ω_1 and ω_2, center frequencies of lower stopband ω_{LS} and upper stopband ω_{US}, the 3-dB bandwidths of the lower and upper stopbands can be conducted using the following equations:

$$\Delta_{LS}=\frac{\omega_1-\frac{\omega_{LS}^2}{\omega_1}}{\omega_{LS}} \tag{6-3a}$$

$$\Delta_{US}=\frac{\frac{\omega_{US}^2}{\omega_2}-\omega_2}{\omega_{US}} \tag{6-3b}$$

By applying 3(a) and 3(b) to their respective low-pass prototype circuits, the element values of proposed BPF in Fig. 6.1 are given by the following formulas:

$$L_{LSi}=\frac{g_{LSi}\left(\omega_1-\frac{\omega_{LS}^2}{\omega_1}\right)}{Y_0\omega_{LS}^2} \tag{6-4a}$$

$$C_{LSi}=\frac{Y_0}{\left(\omega_1-\frac{\omega_{LS}^2}{\omega_1}\right)g_{LSi}} \tag{6-4b}$$

$$L_{USi}=\frac{g_{USi}\left(\frac{\omega_{US}^2}{\omega_2}-\omega_2\right)}{Y_0\omega_{US}^2} \tag{6-4c}$$

$$C_{USi}=\frac{Y_0}{\left(\frac{\omega_{US}^2}{\omega_2}-\omega_2\right)g_{USi}} \tag{6-4d}$$

When the order number *n* of the lower stopband is equal to that of the upper stopband, it has $g_{LSi}=g_{USi}=g_i$, which is the *i*th-order element value of the low-pass prototype filter. The transmission line lengths θ_{LS} and θ_{US} can be calculated by the formulas:

$$\theta_{LS}=(2m+1)\frac{c}{4\omega_{LS}},m=0,1,2\cdots\cdots \tag{6-5a}$$

$$\theta_{US}=(2m+1)\frac{c}{4\omega_{US}},m=0,1,2\cdots\cdots \tag{6-5b}$$

Where *c* stands for the speed of light in the vacuum.

6.3 Bandstop Resonator Analysis

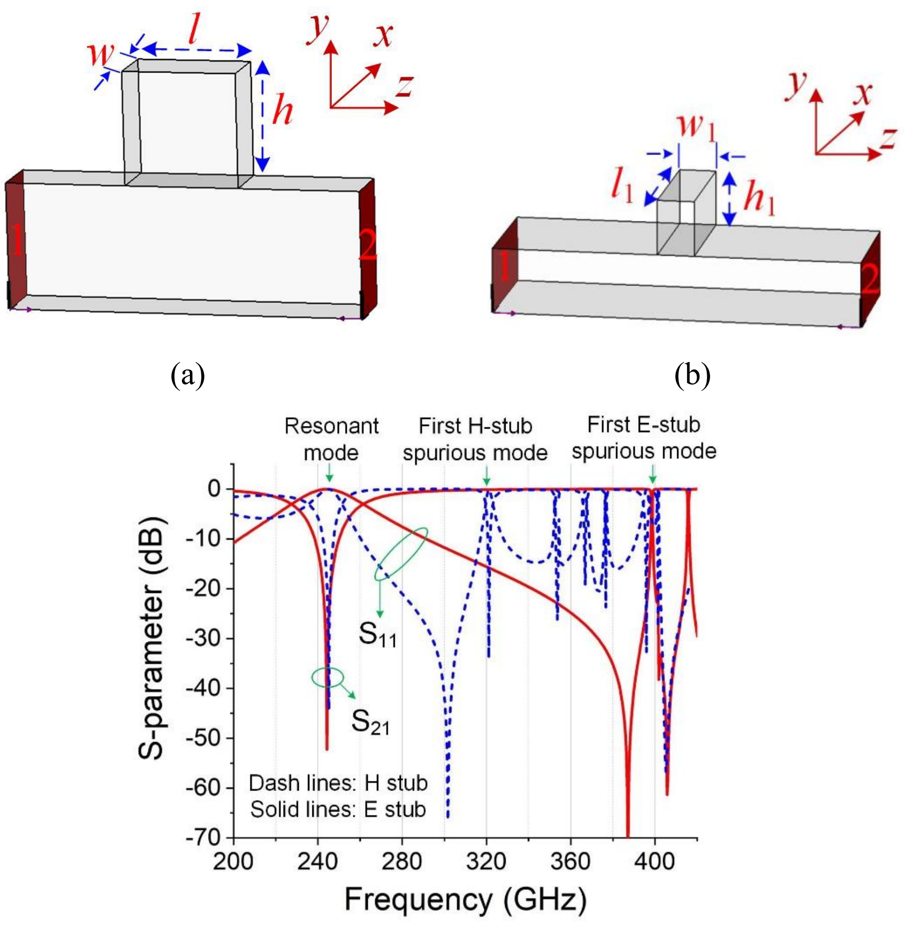

(a) (b)

(c)

Fig. 6.2. The geometries of (a) H-plane stub, (b) E-plane stub, and (c) S-parameter responses of both models.

The E-plane stubs and H-plane stubs are usually used to function as the resonators for BSF design or the dangling resonators for the extracted pole BPF design. In this section a detailed characteristics analysis for both resonators are presented. Here WR-3 is adopted to feed the structure.

The resonant frequencies of the E-plane and H-plane waveguide modes in Figs. 6.2(a)-(b) can be expressed as:

$$\omega_{E(0,m,n)}{}^{2}=\frac{v^{2}}{\varepsilon_{r}\mu_{r}}\left[\left(\frac{m\pi}{h}\right)^{2}+\left(\frac{n\pi}{l}\right)^{2}\right] \tag{6-6a}$$

$$\omega_{H(m,n,0)}{}^{2}=\frac{v^{2}}{\varepsilon_{r}\mu_{r}}\left[\left(\frac{m\pi}{l_{1}}\right)^{2}+\left(\frac{n\pi}{h_{1}}\right)^{2}\right] \tag{6-6b}$$

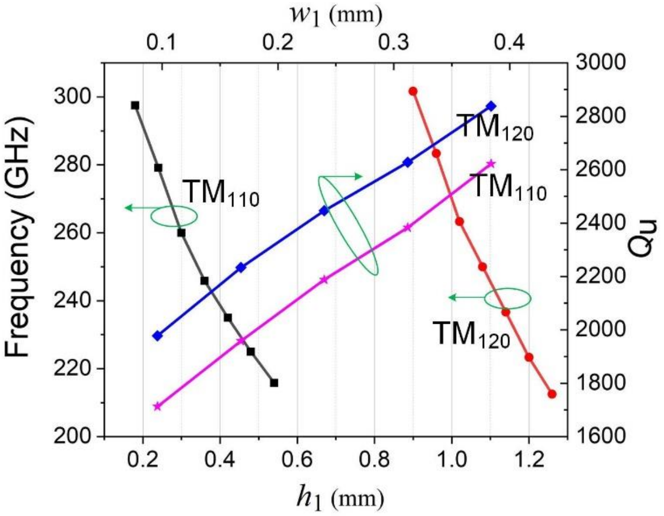

Fig. 6.3. Frequency and Q_u values versus variations of h_1 and w_1 in the E-plane stub model.

where $\omega_{E(0,m,n)}$ and $\omega_{H(m,n,0)}$ stand for the resonant angular frequencies of E-plane and H-plane modes, while v stands for the speed of light in the vacuum. ε_r and μ_r are the permittivity and permeability of the air of the waveguide, respectively. For both models, the length and height of the stub are used to control the resonant frequencies while the width is adopted to vary the unloaded quality factor (Q_u) of the stub. When m=1 and n=1, to set the fundamental modes TE$_{011}$ of H-plane and TM$_{110}$ of E-plane at the same frequency of 243 GHz as can be seen in Fig. 6.2(c), the first spurious mode of H-plane stub is located at 320 GHz, while that of E-plane stub is located at 395 GHz with a frequency ratio of 1.62. It is obvious that E-plane stub has wider spurious range than H-plane stub. Furthermore, it requires a smaller size than H-plane stub when resonating at the same frequency. Therefore, E-plane stub is a better candidate for our design. The length l_1 is usually equal to the long side of the waveguide port, thus the height is used to control the resonant frequency while width serves to vary the Q_u of the stub, respectively.

Fig. 6.3 shows the parameter analysis of the first two resonant modes TM$_{110}$ and TM$_{120}$ in the E-plane stub model. It can be seen that both modes have a similar frequency and Q_u curves when height h_1 and width w_1 change. When h_1 increases, TM$_{110}$ and TM$_{120}$ modes shift to the lower frequencies. TM$_{120}$ mode always requires a bigger h_1 value than TM$_{110}$ mode when resonating at the same frequency. When w_1 increases, both modes have a bigger Q_u value and TM$_{120}$ mode always has a bigger Q_u value than that of TM$_{110}$ mode when w_1 is fixed. It can be concluded that miniaturization and

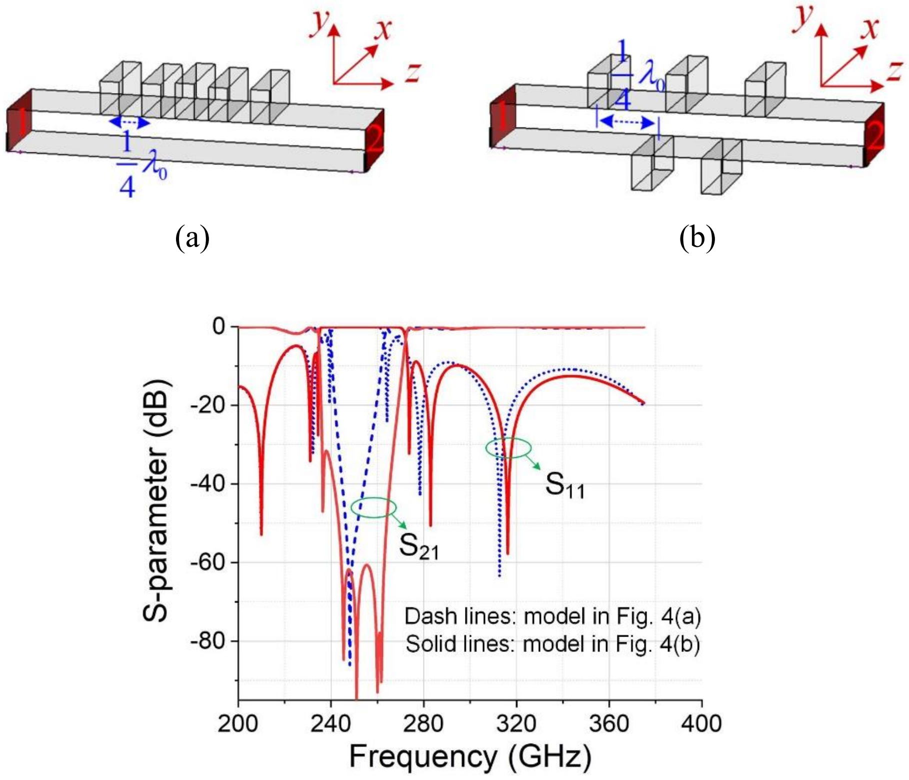

(a) (b)

(c)

Fig. 6.4. 5th-order BSF with: (a) All stubs are on the same side, (b) Stubs are on the opposite side, (c) S-parameters.

wideband performance can be implemented by using TM110 mode, while narrowband performance can be achieved by using TM120 mode or higher.

Fig. 6.4 presents 5th-order waveguide BSF prototype using E-plane stubs. In Fig. 6.4(a), five stubs are all placed on the same side of the waveguide with a distance of $1/4\,\lambda_0$ between them, and λ_0 is the wavelength of the center frequency. Meanwhile in Fig. 6.4(b), the first, third, and fifth stubs are still on the same side, and the second and fourth stubs are placed on the opposite side of the waveguide. The distance between the adjacent stubs is still $1/4\,\lambda_0$. S-parameters in Fig. 6.4(c) show that the prototype in Fig. 6.4(b) has a wider BSF bandwidth than what is shown in Fig. 6.4(a), which means there is a wider spurious bandwidth in the BPF design. For this reason the comb-type E-plane prototype will be adopted in the following designs.

6.4. Proposed Inline Waveguide Bandpass Filter Design

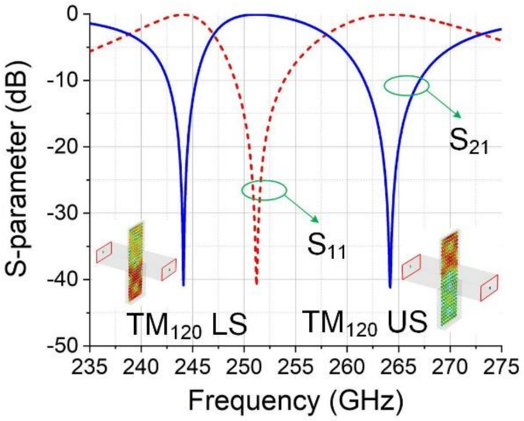

Fig. 6.5. S-parameters of 1st-order narrow-band BPF (LS: lower stopband, US: upper stopband).

The bandwidth of the proposed filter design synthesis is flexible, which can be applied in the narrowband and wideband range. Two 5th-order BPFs with different bandwidths will be discussed separately in the following section. They are constructed and simulated using CST studio suite and based on brass material with a conductivity of 2.74×10^7 S/m. The inner length and width of WR-3 are 0.8636 mm and 0.4318 mm, respectively.

Narrowband performance requires the utilization of high Q_u resonators. TM_{120} E-plane stub is adopted as 1st-order BPF prototype shown in the inset of Fig. 6.5. Two TM_{120} E-plane stubs are centered on the opposite sides of the waveguide. One is used to generate a transmission zero (TZ) at the lower stopband while the other is to generate a TZ at the upper stopband. One reflection zero (RZ) will be generated between these two TZs as plotted in Fig. 6.5.

A specification for the narrow-band BPF is set: center frequency: 247 GHz, fractional bandwidth: 2.2%, out-of-band rejection: better than 25 dB. A 5th-order narrowband BPF is designed with its geometry presented in Fig. 6.6(a). A total of ten TM_{120} mode E-plane stubs are adopted with five dominating at the lower stopband while the other five dominate at the upper stopband. They follow the arrangement discussed in Section 6.3 that a cross-finger BPF prototype is formed. These two groups of the bandstop elements are geometrically parallel and can be independently controlled.

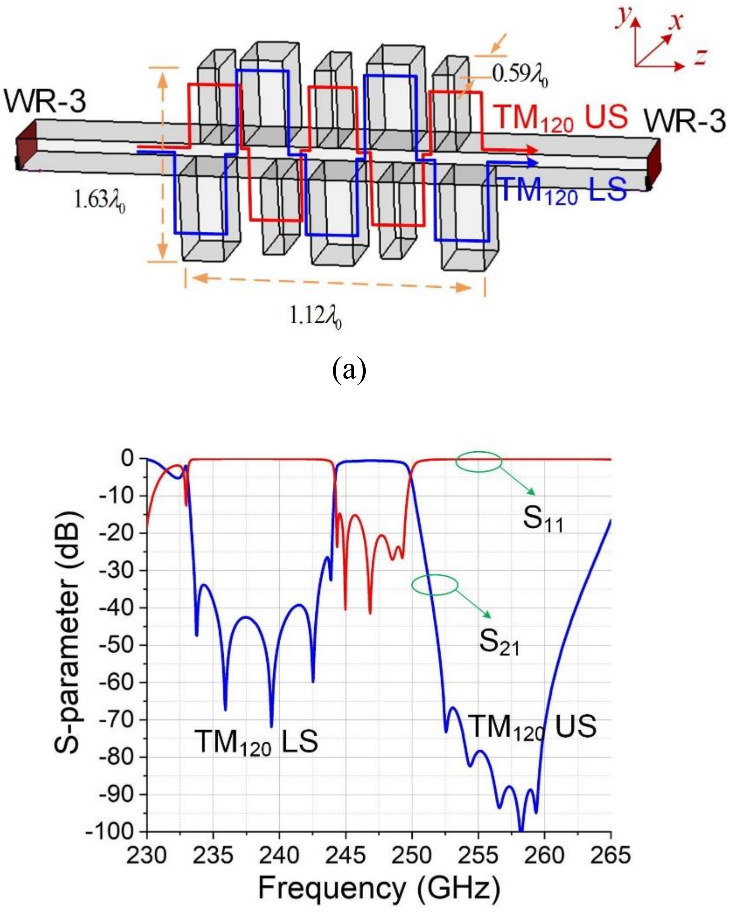

(a)

(c)

Fig. 6.6. 5th-order narrow-band BPF with: (a) Geometry, (b) S-parameters.

The widths of lower stopband stubs and upper stopband stubs are denoted as w_2 and w_3, respectively. They are used to control the Q_u values of stub elements. The lengths of all the stubs are equal to that of the waveguide. For 5th-order BPF case, in the lower stopband, the height of middle stub, first adjacent symmetrical stubs and second adjacent symmetrical stubs are denoted as h_2, h_3, and h_4, respectively. The distance between the middle stub and first adjacent stubs are s_1, middle stub and second adjacent stubs are s_2. Meanwhile in the upper stopband, they are denoted as h_5, h_6, and h_7, and the distance between the middle stub and first adjacent stubs is s_3. For the middle stub and second adjacent stubs the distance is s_4.

Fig. 6.6(b) shows the S-parameters of the designed 5th-order BSF. It resonates at 247 GHz and 3-dB simulated insertion loss frequency range is from 244.5 GHz to 250 GHz with 5.5 GHz 3-dB bandwidth and a minimum insertion loss of 0.7 dB. It has five RZs and the return loss is better than 15 dB within the whole passband. It also has ten TZs with five at lower stopband and five at upper stopband. 11 GHz spurious-free range at

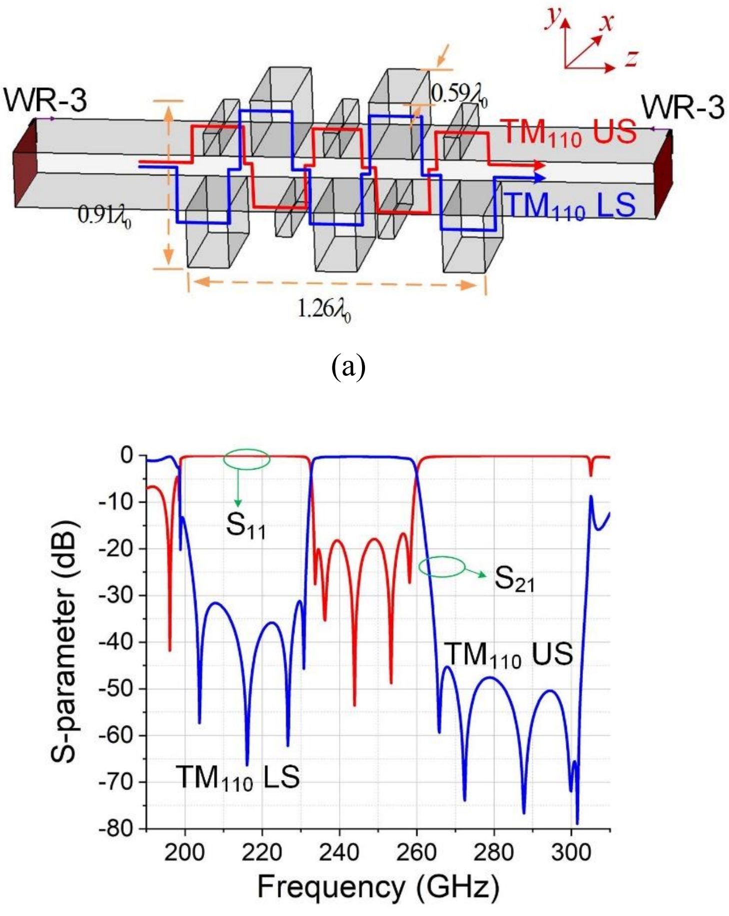

(a)

(c)

Fig. 6.7. 5th-order moderate-band BPF with: (a) Geometry, (b) S-parameters.

the lower stopband where S21 is lower than 20 dB is achieved, while at the upper stopband it can achieve 14 GHz spurious-free range. The whole structure is very compact with an inner circuit size of $1.12\lambda_0 \times 1.63\lambda_0 \times 0.59\lambda_0$. The implemented physical dimensions of the proposed 5th-order BPF are listed in Table 6.1.

TABLE 6.1

PHYSICAL DIMENSIONS OF PROPOSED 5TH-ORDER NARROW-BAND BPF (UNIT: MM)

$w_2 = 0.2$	$w_3 = 0.07$	$h_2 = 1.055$	$h_3 = 1.04$
$h_4 = 1.06$	$h_5 = 0.99$	$h_6 = 0.98$	$h_7 = 0.97$
$s_1 = 0.38$	$s_2 = 0.77$	$s_3 = 0.36$	$s_4 = 0.72$

Unlike the narrowband BPF design which uses TM$_{120}$ mode E-plane stubs as the resonant elements, TM$_{110}$ mode stubs are chosen to design the moderate-band BPF due to its relevant lower Q_u value.

We set the specification of designed moderate-band BPF as: center frequency: 247

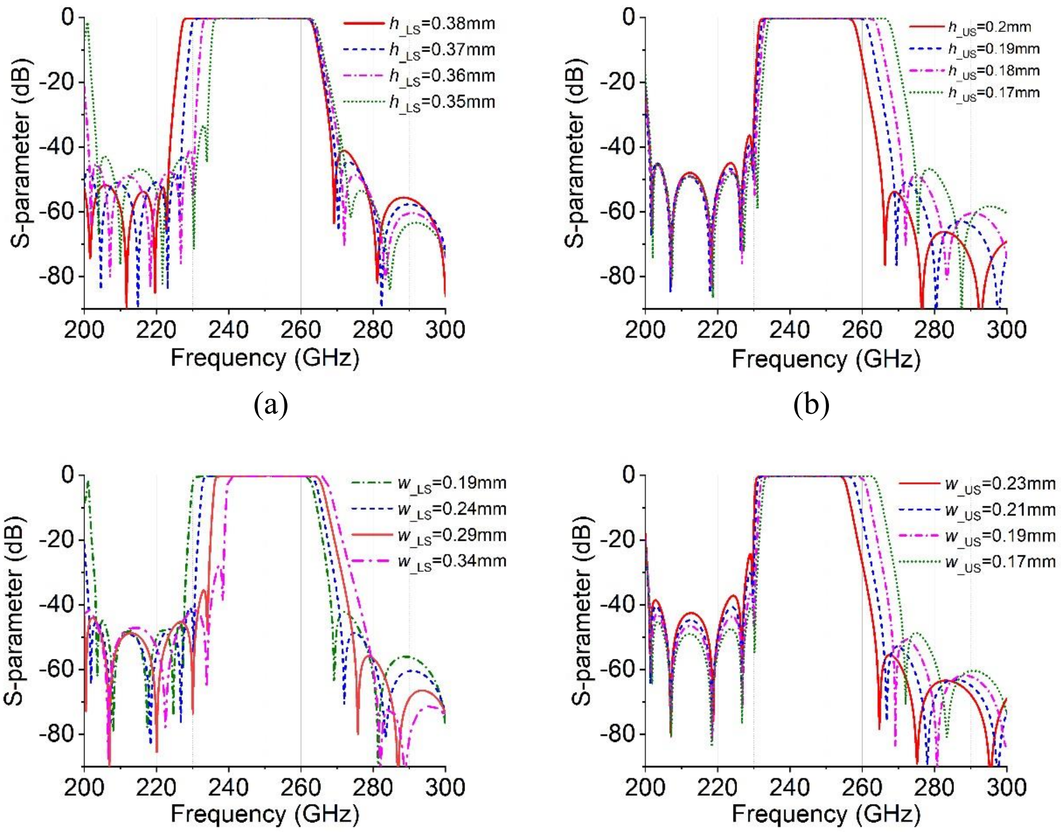

(a) (b)

(c) (d)

Fig. 6.8. S-parameters of the 5th-order moderate-band BPF versus varied parameters: (a) $h_{\_\mathrm{LS}}$, (b) $h_{\_\mathrm{US}}$, (c) $w_{\_\mathrm{LS}}$, (d) $w_{\_\mathrm{US}}$.

GHz, fractional bandwidth: 11%, out-of-band rejection: better than 30 dB. The 5th-order moderate-band BPF prototype is presented in Fig. 6.7(a). Although it includes ten E-plane stubs, they are all dominated by TM_{110} mode which has shorter stub length compared with TM_{120} mode. The implemented widths of stubs at the lower and upper stopbands will be wider than those in the narrowband design, which can enlarge the bandwidth of the passband.

Fig. 6.7(b) presents the simulated S-parameters of the designed 5th-order moderate-band BPF. It resonates at 247 GHz and 3-dB simulated insertion loss frequency range is from 233 GHz to 260 GHz with 27 GHz 3-dB bandwidth. The minimum insertion loss is 0.15 dB within the passband. It also has ten TZs with five at lower stopband and five at upper stopband. 31 GHz spurious-free range at the lower stopband where S21 is lower than 20 dB is achieved, while at the upper stopband it can achieve 41 GHz spurious-free range.

To directly reflect the parameter effects on the S-parameter changes, the width $w_{\_\mathrm{LS}}$

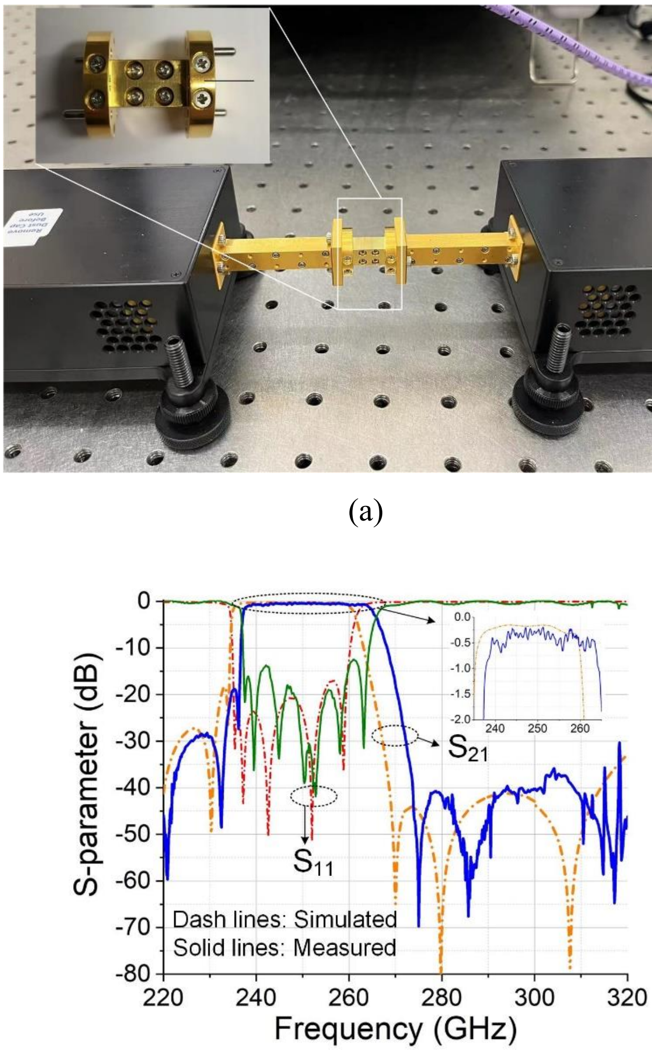

(a)

(c)

Fig. 6.9. The proposed 5th-order BPF with: (a) Photograph of the fabricated model, (b) Simulated and measured S-parameters.

$= w_2$ and length $h\_\mathrm{LS} = h_2 = h_3 = h_4$ of lower stopband stubs, and the width $w\_\mathrm{US} = w_3$ and length $h\_\mathrm{US} = h_5 = h_6 = h_7$ of the upper stopband stubs are adopted and plotted in Fig. 6.8. As discussed in Section 6.3, then stub length is used to control the resonant frequency of the bandstop resonator, while the width helps to adjust the Q_u values of the resonator. Therefore as shown in Fig. 6.8(a), when h_LS decreases, the lower stopband shifts to the higher frequency with constant fractional stopband bandwidth, while the upper stopband remains unchanged. Similarly in Fig. 6.8(b), the smaller h_US values, the higher upper stopband frequencies. When w_LS increases, the achieved lower stopband bandwidth is becoming narrower, and it will slightly affect the upper stopband performance. When w_US increases, the upper stopband bandwidth is also narrower, and the lower stopband performance remains unchanged. Basically, these four parameters can individually determine the resonant frequencies and bandwidth of both stopbands. The distances between the resonators for both stopbands, $s_{\_\mathrm{LS}}$ and $s_{\_\mathrm{US}}$, can be used to slightly adjust the impedance matching within the passband.

Finally, the 6th-order moderate-band BPF is fabricated and tested. Fig. 6.9(b) presents the simulated and measured S-parameters comparison of the 5th-order BPF prototype. The measured results show that it resonates at a center frequency of 250 GHz, a frequency offset of 3 GHz from the simulated center frequency of 247 GHz. The minimum measured insertion loss is 0.2 dB, and the average insertion loss is 0.35 dB. The measured 1-dB bandwidth is from 238 GHz to 265 GHz. The attenuation level is better than 18 dB in the lower stopband and 30 dB in the upper stopband. Due to the operating frequency range of WR-3, here we show the test range from 220 GHz to 320 GHz. Three TZs in the lower stopband and three TZs in the upper stopband are achieved in this range, which shows a good agreement compared with the simulated results.

The whole internal circuit volume is $1.36\lambda_0 \times 0.8\lambda_0 \times 0.9\lambda_0$. The implemented physical dimensions of the proposed 5th-order BPF are listed in Table 6.2.

TABLE 6.2

Physical Dimensions of Proposed 5th-order Moderate-Band BPF (Unit: mm)

$w_2 = 0.24$	$w_3 = 0.2$	$h_2 = 0.348$	$h_3 = 0.348$
$h_4 = 0.348$	$h_5 = 0.185$	$h_6 = 0.185$	$h_7 = 0.185$
$s_1 = 0.37$	$s_2 = 0.765$	$s_3 = 0.395$	$s_4 = 0.66$

Comparing the proposed BPF based on the BSR pair and other reported THz BPFs is summarized in Table 6.3. The conventional BPFs have more insertion loss since their elements resonate at the passband. Meanwhile, the generation of TZs using traditional topologies, i.e., extracted pole resonator, singlets, and high order mode resonator, have complicated structures with limited TZs. The design complexity can be a challenging issue when achieving a higher-order response. The proposed BPF design approach is very flexible; it can be applied to achieve both narrowband and wideband designs. Because of the utilization of BSF elements that resonate in the stopband, it has less insertion loss than the conventional BPFs. A 5th-order moderate-band BPF designed at 250 GHz has an FBW of 11% and minimum measured insertion loss of 0.2 dB. Furthermore, the proposed design can produce a maximum of $2N$ TZs in the Nth filter response, which improves the rectangle coefficient and out-of-band rejection. This 5th-order BPF generates 10 TZs with a square factor of 1.22.

TABLE 6.3

COMPARISON WITH REPORTED THZ BANDPASS FILTERS

Ref.	Frequency (GHz)	FBW (%)	IL (dB)	Filtering Order	No. of TZs	$\frac{BW_{25\text{dB}}}{BW_{3\text{dB}}}$	Comments
[1]	140	14.3	2.44	4	0	1.75	LTCC
[2]	300	8	1	5	0	1.67	Chebyshev
[3]	286.6	5.58	0.41	3	2	N.G.	Extracted pole resonator
[4]	258	8.8	0.7	4	2	1.54	High order mode cavity
[5]	140	9.29	0.52	5	2	1.29	Singlets
[6]	141.9	10.22	0.61	5	0	1.68	Chebyshev
[7]	102	5	1.2	4	2	N.G.	Extracted pole resonator
[8]	140	17.18	0.33	8	2	1.18	High order mode cavity
This work	**250**	**11**	**0.2**	**5**	**10**	**1.22**	**DBBSF**

* FBW: 3-dB Fractional Bandwidth, IL: Minimum Insertion Loss, No. of TZs: Number of Transmission zeroes, BW_{25dB}/BW_{3dB}: ratio of 25-dB bandwidth to 3-dB bandwidth

λ_0: waveguide wavelength of the center frequency in the vacuum, NG: Not Given.

6.5. Conclusion

In this chapter, we present a novel BPF design methodology based on BSR pair. They are topologically in parallel with little mutual interference and follow the frequency-variable transformation to the LPF to conduct the lower stopband and upper stopband, respectively. A passband is created with controllable bandwidth and filtering order. Finally, a 5th-order BPF with 10 TZs are designed, fabricated, and tested. The proposed method is very simple and flexible and parameters in the design are not very sensitive, the circuit values can be realized by different types of physical model resonators. It can be easily applied to higher frequencies, including millimeter wave and terahertz wave communication systems.

6.6 References

[1] K. Wang, S.-W. Wong, G.-H. Sun, Z. N. Chen, L. Zhu and Q.-X. Chu, "Synthesis method for substrate-integrated waveguide bandpass filter with even-order Chebyshev

response," *IEEE Trans. Compon., Packag. and Manuf. Techn.*, vol. 6, no. 1, pp. 126-135, Jan. 2016.

[2] X. Shang, M. Ke, Y. Wang and M. J. Lancaster, "WR-3 band waveguides and filters fabricated using SU8 photoresist micromachining technology," *IEEE Trans. THz Sci. Technol.*, vol. 2, no. 6, pp. 629-637, Nov. 2012.

[3] H. Yang *et al.*, "WR-3 waveguide bandpass filters fabricated using high precision CNC machining and SU-8 photoresist technology," *IEEE Trans. THz Sci. Technol.*, vol. 8, no. 1, pp. 100-107, Jan. 2018.

[4] J.-Q. Ding, S.-C. Shi, K. Zhou, Y. Zhao, D. Liu and W. Wu, "WR-3 band quasi-elliptical waveguide filters using higher order mode resonances," *IEEE Trans. THz Sci. Technol.*, vol. 7, no. 3, pp. 302-309, May 2017.

[5] Y. Xiao, P. Shan, K. Zhu, H. Sun and F. Yang, "Analysis of a novel singlet and its application in THz bandpass filter design," *IEEE Trans. THz Sci. Technol.*, vol. 8, no. 3, pp. 312-320, May 2018.

[6] X. H. Zhao *et al.*, "D-band micromachined silicon rectangular waveguide filter," *IEEE Microw. Wireless Compon. Lett.*, vol. 22, no. 5, pp. 230-232, May 2012.

[7] C. A. Leal-Sevillano, J. R. Montejo-Garai, M. Ke, M. J. Lancaster, J. A. Ruiz-Cruz and J. M. Rebollar, "A pseudo-elliptical response filter at W-band fabricated with thick SU-8 photo-resist technology," *IEEE Microw. Wireless Compon. Lett.*, vol. 22, no. 3, pp. 105-107, March 2012.

[8] Y.-W. Wu, Z.-C. Hao, R. Lu and J.-S. Hong, "A high-selectivity D-band mixed-mode filter based on the coupled overmode cavities," *IEEE Trans. Microw. Theory Techn.*, vol. 68, no. 6, pp. 2331-2342, Jun. 2020.

[9] R. J. Cameron, "General coupling matrix synthesis methods for Chebyshev filtering functions," *IEEE Trans. Microw. Theory Techn.*, vol. 47, no. 4, pp. 433-442, April 1999.

[10] X. Chen and K. Wu, "Substrate integrated waveguide cross-coupled filter with negative coupling structure," *IEEE Trans. Microw. Theory Techn.*, vol. 56, no. 1, pp. 142-149, Jan. 2008.

[11] Y. Wang and M. Yu, "True inline cross-coupled coaxial cavity filters," *IEEE Trans. Microw. Theory Techn.*, vol. 57, no. 12, pp. 2958-2965, Dec. 2009.

[12] N. Mohottige, O. Glubokov, U. Jankovic and D. Budimir, "Ultra compact inline E -plane waveguide bandpass filters using cross coupling," *IEEE Trans. Microw. Theory Techn.*, vol. 64, no. 8, pp. 2561-2571, Aug. 2016.

[13] S. Amari and U. Rosenberg, “New in-line dual- and triple-mode cavity filters with nonresonating nodes,” *IEEE Trans. Microw. Theory Techn.*, vol. 53, no. 4, pp. 1272–1279, Apr. 2005.

[14] C. Tomassoni, S. Bastioli, and R. Sorrentino, “Generalized TM dual-mode cavity filters,” *IEEE Trans. Microw. Theory Techn.*, vol. 59, no. 12, pp. 3338–3346, Dec. 2011.

[15] S. W. Wong, Z. C. Guo, J. Y. Lin, L. Zhu, and Q. Zhang, “Triplemode and triple-band cavity bandpass filter on triplet topology with controllable transmission zeros,” *IEEE Access*, vol. 6, pp. 29,452–29,459, May 2018.

[16] Y.-W. Wu, Z.-C. Hao, R. Lu and J.-S. Hong, "A High-Selectivity D-Band Mixed-Mode Filter Based on the Coupled Overmode Cavities," *IEEE Trans. Microw. Theory Techn.*, vol. 68, no. 6, pp. 2331-2342, June 2020.

[17] S. Amari, U. Rosenberg and J. Bornemann, "Singlets, cascaded singlets, and the nonresonating node model for advanced modular design of elliptic filters," *IEEE Microw. Wireless Compon. Lett.*, vol. 14, no. 5, pp. 237-239, May 2004.

[18] S. Amari and U. Rosenberg, "Characteristics of cross (bypass) coupling through higher/lower order modes and their applications in elliptic filter design," *IEEE Trans. Microw. Theory Techn.*, vol. 53, no. 10, pp. 3135-3141, Oct. 2005.

[19] C. Tomassoni, S. Bastioli and R. V. Snyder, "Propagating waveguide filters using dielectric resonators," *IEEE Trans. Microw. Theory Techn.*, vol. 63, no. 12, pp. 4366-4375, Dec. 2015.

[20] G. Macchiarella, G. G. Gentili, C. Tomassoni, S. Bastioli and R. V. Snyder, "Design of waveguide filters with cascaded singlets through a synthesis-based approach," *IEEE Trans. Microw. Theory Techn.*, vol. 68, no. 6, pp. 2308-2319, June 2020.

[21] J. D. Rhodes and R. J. Cameron, "General extracted pole synthesis technique with applications to low-loss TE/sub011/ mode filters," *IEEE Trans. Microw. Theory Techn.*, vol. 28, no. 9, pp. 1018-1028, Sep. 1980.

[22] J. R. Montejo-Garai, J. A. Ruiz-Cruz, J. M. Rebollar, M. J. Padilla-Cruz, A. Onoro-Navarro and I. Hidalgo-Carpintero, "Synthesis and design of in-line N-order filters with N real transmission zeros by means of extracted poles implemented in low-cost rectangular H-plane waveguide," *IEEE Trans. Microw. Theory Techn.*, vol. 53, no. 5, pp. 1636-1642, May 2005.

[23] R. J. Cameron, C. M. Kudsia, and R. R. Mansour, *Microwave Filters for Comunication Systems.* New York, NY, USA: Wiley, 2007.

[24] Y. Yang, M. Yu and Q. Wu, "Advanced synthesis technique for unified extracted pole filters," *IEEE Trans. Microw. Theory Techn.*, vol. 64, no. 12, pp. 4463-4472, Dec. 2016.

[25] Y. Yang, M. Yu, Q. Wu, X. Yin and J. Yang, "A fully integrated multiplexer using unified extracted pole technique," *IEEE Trans. Microw. Theory Techn.*, vol. 68, no. 8, pp. 3439-3447, Aug. 2020.

[26] Jing-Ren Qian and Wei-Chen Zhuang, "New Narrow-Band Dual-Mode Bandstop Waveguide Filters," *IEEE Trans. Microw. Theory Techn.*, vol. 31, no. 12, pp. 1045-1050, Dec. 1983.

[27] A. A. Kirilenko, L. A. Rud and S. L. Senkevich, "Spectral approach to the synthesis of bandstop filters," *IEEE Trans. Microw. Theory Techn.*, vol. 42, no. 7, pp. 1387-1392, July 1994.

[28] S. Amari, U. Rosenberg and R. Wu, "In-line pseudoelliptic band-reject filters with nonresonating nodes and/or phase shifts," *IEEE Trans. Microw. Theory Techn.*, vol. 54, no. 1, pp. 428-436, Jan. 2006.

[29] J. R. Montejo-Garai, J. A. Ruiz-Cruz, J. M. Rebollar and T. Estrada, "In-Line Pure E-Plane Waveguide Band-Stop Filter With Wide Spurious-Free Response," *IEEE Microw. Wireless Compon. Lett.*, vol. 21, no. 4, pp. 209-211, Apr. 2011.

[30] H. Uchida *et al.*, "Dual-band-rejection filter for distortion reduction in RF transmitters," *IEEE Trans. Microw. Theory Techn.*, vol. 52, no. 11, pp. 2550-2556, Nov. 2004.

[31] Mahbubeh Esmaeili, Jens Bornemann, "Substrate integrated waveguide dual-

stopband filter," *Microwave and Optical Technology Letters*, vol. 56, pp. 1561, 2014.
[32] F. Cheng, X.-T. Li, P. Lu, and K. Huang, "Synthesis and design of SIW dual-band narrowband bandstop filter, " *Electromagnetics*, vol. 40, no. 5, pp. 303-312, Jun. 2020.
[33] R. J. Cameron, Ming Yu and Ying Wang, "Direct-coupled microwave filters with single and dual stopbands," *IEEE Trans. Microw. Theory Techn.*, vol. 53, no. 11, pp. 3288-3297, Nov. 2005.
[34] N. He, X. L. Wang, S. H. Han, T. Lin, Z. Liu, "The synthesis and design for new classic dual-band waveguide band-stop filters," *Journal of Electromagnetic Waves and Applications*, vol. 22, pp. 119, 2008.
[35] Q. Xue and J. Y. Jin, "Bandpass filters designed by transmission zero resonator pairs with proximity coupling," *IEEE Trans. Microw. Theory Techn.*, vol. 65, no. 11, pp. 4103-4110, Nov. 2017.

Chapter 7 Conclusion and Future Work

7.1 Conclusion

Historically, cavity-based narrowband filters and multiplexers have been explored and designed for base stations or satellite applications. Compared with single-mode resonators (SMRs), the implementation of MMRs in waveguide structures is a promising solution to dramatically reduce circuit volume and improve frequency selectivity. Taking advantage of MMR techniques, a variety of innovative waveguide structures have been proposed for a wide range of application scenarios. The thesis first summarized the state-of-the-art MMR-based works in Chapter 1, including filters, multiplexers, crossovers, and balun circuits.

Chapter 2 explores the modal orthogonality and out-of-phase performance of three fundamental modes. It presents the designs of waveguide filtering magic-Ts. Furthermore, it can integrate more functions in a single circuit, i.e., balun and balanced functions, diplexing function are demonstrated in this chapter. The first design is a balanced-to-unbalanced filtering magic-T, it integrates baluns, filters and magic-T in one structure. The second design is a duplexing filtering power divider, it integrates duplexer, filters and power dividers in one structure. The related content entitled "Cavity Filtering Magic-T and Its Integrations Into Balanced-to-Unbalanced Power Divider and Duplexing Power Divider" has been published in **IEEE Transactions on Microwave Theory and Techniques.**

Chapter 3 focuses on investigating the characteristics of high-order mode resonators. Each magnetic loop of the utilized high-order modes is in-phase with the same amplitude, which is a good candidate for filtering antenna array designs. It significantly reduces the design methodology of filtering antenna array, and also reduces the interconnection loss and eliminates the power splitting network. The related content entitled "High-Order Modes Analysis and Its Applications to Dual-Band Dual-Polarized Filtering Cavity Slot Arrays" has been published on **IEEE Transactions on Microwave Theory and Techniques**.

Chapter 4 proposes in-band full-duplex filtering antenna arrays based on a pair of degenerate high-order mode resonators. Narrow-band and wide-band performance are designed at the same time for different application scenarios. Firstly, a very compact structure is produced. Secondly, since the filters, OMT, and antenna arrays are integrated into one circuit, this reduces design complexity. Two individual channels share the same cavity resonator without interaction. Thirdly, fully overlapping bandwidth is achieved and it significantly avoids wasting spectrum resources. The related content entitled “Filtering Full-Duplex Waveguide Slot Arrays Using High-Order Mode Cavity Resonators” has been published on **IEEE Transactions on Microwave Theory and Techniques**.

Chapter 5 proposes diplexing in-band full-duplex antennas based on quadruple-mode resonators. A two-way waveguide diplexer is implemented by using a pair of degenerate fundamental modes and a pair of high-order modes. Then a diplexing IBFD antenna with a turnstile junction is designed by replacing the inputs with a cross-coupled radiating slot. The proposed designs integrate multiple diplexing channels into a single device, significantly reducing the transceiver hardware volume and simplifying the design methodology. The related content entitled “Two-Way Waveguide Diplexer and Its Application to Diplexing In-Band Full-Duplex Antenna” has been published on **IEEE Transactions on Microwave Theory and Techniques**.

Chapter 6 focuses on 250 GHz inline waveguide bandpass filter designs. They are implemented by E-plane stubs and resonated at the lower and upper stopbands of the designed BPF, respectively, to provide sharp roll-off and out-of-band rejection. Both stopbands can be controlled independently and cascaded in parallel from source to load without mutual interference**.** Finally, a 5th-order BPF with 10 TZs are designed, fabricated, and tested. The related content entitled “Inline Waveguide Bandpass Filter Using Bandstop Resonator Pairs” has been submitted to **2023 IEEE MTT-S International Microwave Symposium (IMS)**.

In addition, Chapters 2-5 implement a variety of multi-functional filtering designs using multi-mode resonators, the design methodology and mechanism are discussed in detailed. These circuits would be very challenging to achieve using planar structure in PCB technology. They have the potential applications in wireless systems that handle high power or imaging/sensing systems that require high efficiency, i.e., gateway feeder links for high-throughput satellites and the point-to-point or backhaul links for terrestrial networks.

7.2 Future work

The millimeter-wave and terahertz frequency regions will be my next topic. The use of

3-D metal printing and high precision CNC fabrication will be the key points. The following three issues will be focused on:

1. Inline Bandpass Filters Based on Bandpass-Bandstop Resonator Section. A novel and generic modular section to contain both bandpass resonator and bandstop resonator, namely composite bandpass-bandstop resonator (CBPBSR) section, will be investigated in the next step. The CBPBSR section is a general resonator expression form, which covers the single-mode and multiple-mode BPRs and BSRs, respectively. The BPRs are placed in parallel between the J inverters while the BSRs are dangled on the BPRs. BPFs with arbitrary RZs and TZs can be synthesized using different BPBSR sections. For a given specification, this equivalent model can systematically identify the scaling properties of the structures. This leads to completely new filter structures that can be designed in a more convenient and modular fashion. This novel concept of composite resonator sections will provide a new paradigm for the otherwise established art of filter design.

2. Tunable mm-wave and THz devices. Tunable or reconfigurable devices have a wider range of applications, but switches commonly used in the microwave region, such as pin diodes, cannot be used in the millimeter-wave and terahertz regions. Therefore, exploring phase-change materials such as graphene to dynamically control the state of the device may be a good approach and individual control of each band based on multi-mode resonators, which deserves research attention.

3. Investigation of 3-D metal printing for mm-wave and THz waveguide fabrication. 3-D metal printing technology offers a new manufacture solution where waveguide structures with complex geometry may be produced monolithically or using a reduced number of separate pieces with reduced need for assembly. The free-forming capability of the 3D printing will also be utilised to implement more intricate resonator structures that are difficult or impossible for traditional CNC machining. This will allow to realise the full potential of the composite BPBSR structures (of either a simple or intricate geometry structure) and demonstrate demanding transfer functions such as multiple-band filters.

Publications

[1] **Jing-Yu Lin**, Y. Yang, Sai-Wai Wong, and Y. Li, "High-order modes analysis and its applications to dual-band dual-polarized filtering cavity slot arrays," ***IEEE Transactions on Microwave Theory and Techniques***, vol. 69, no. 6, pp. 3084-3092, Jun. 2021.

[2] **Jing-Yu Lin**, Y. Yang, Sai-Wai Wong, R.-S. Chen, Y. Li, L. Zhang, Y. He, and L. Zhu, "Cavity filtering magic-T and its integrations into balanced-to-unbalanced power divider and duplexing power divider," ***IEEE Transactions on Microwave Theory and Techniques***, vol. 67, no. 12, pp. 4995-5004, Dec. 2019.

[3] **Jing-Yu Lin**, Sai-Wai Wong, Y.-M. Wu, Y. Yang, L. Zhu, and Y. He, "Three-way multiple-mode cavity filtering crossover for narrow- and broad-band applications," ***IEEE Transactions on Microwave Theory and Techniques***, vol. 67, no. 3, Mar. 2019.

[4] **Jing-Yu Lin**, Sai-Wai Wong, Y.-M. Wu, L. Zhu, Y. Yang, and Y. He, "A new concept and approach for integration of three-state cavity diplexer based on triple-mode resonators," ***IEEE Transactions on Microwave Theory and Techniques***, vol. 66, no. 12, Dec. 2018.

[5] **Jing-Yu Lin**, Sai-Wai Wong, Lei Zhu, Yang Yang, Xi Zhu, Z.-M. Xie, and Ye-Jun He; "A Dual-Functional Triple-Mode Cavity Resonator with the Integration of Filters and Antennas," ***IEEE Transactions on Antenna Propagation***, vol. 66, no. 5, May 2018.

[6] **Jing-Yu Lin**, S.W. Wong, L. Zhu, and Q.X. Chu, "Design of Miniaturized Triplexers via Sharing a Single Triple-Mode Cavity Resonator," ***IEEE Transactions on Microwave Theory and Techniques***, vol. 65, no. 10, pp. 3877-3884, Oct. 2017.

[7] **J.-Y. Lin**, S.-W. Wong, Y. Yang, and R.–S. Chen, "In-Band Full-Duplex Filtering Antenna Arrays Using High-Order Mode Cavity Resonators," ***IEEE Transactions on Microwave Theory and Techniques***, early access, 2022.

[8] **J.-Y. Lin**, Y. Yang, S.-W. Wong, X. Li, L. Wang, and E. Dutkiewicz, "Two-Way Waveguide Diplexer and Its Application to Diplexing In-Band Full-Duplex Antenna," ***IEEE Transactions on Microwave Theory and Techniques***, early access, 2022.

[9] S.-W. Wong, **Jing-Yu Lin (corresponding author)**, Y. Yang, Z.-C. Guo, and L. Zhu, "Microwave waveguide components based on multiple-mode resonators," ***IEEE***

Microwave Magazine, 2021.

[10] S.-W. Wong, **Jing-Yu Lin (corresponding author)**, Y. Yang, H. Zhu, R. Chen, L. Zhu, and Y. He, “Cavity balanced and unbalanced diplexer based on triple-mode resonator,” ***IEEE Transactions on Industrial Electronics***, vol. 67, no. 6, pp. 4969-4979, Jun. 2019.

[11] H. Zhu, **Jing-Yu Lin**, and Y. J. Guo, "Filtering Balanced-to-Single-Ended Power Dividers With Wide Range and High Level of Common-Mode Suppression," ***IEEE Transactions on Microwave Theory and Techniques***, vol. 67, no. 12, pp. 5038-5048, Dec. 2019.

[12] S. Zhou, **Jing-Yu Lin**, S.-W. Wong, F. Deng, L. Zhu, Y. Yang, Y. He, and Z.-H. Tu, “Spoof surface plasmon polaritons power divider with large isolation,” ***Scientific Reports***, 8, 5947, Apr. 2018.

[13] Z.-C. Zhang, S.-W. Wong, **Jing-Yu Lin,** H. Liu, L. Zhu, and Y. He, “Design of multistate diplexers on uniform- and stepped-impedance stub-loaded resonators,” ***IEEE Transactions on Microwave Theory and Techniques***, vol. 67, no. 4, Apr. 2019.

[14] S.-W. Wong, B.-L. Zheng, **Jing-Yu Lin,** Z.-C. Zhang, Y. Yang, L. Zhu, and Y. He, “Design of three-state diplexer using a planar triple-mode resonator,” ***IEEE Transactions on Microwave Theory and Techniques***, vol. 66, no. 9, pp. 4040-4046, Sep. 2018.

Conference papers：

[1] **Jing-Yu Lin**, Y. Yang and S.-W. Wong, "Four-Way Filtering Crossover Based on Quadruple-Mode Cavity Resonator," *2021 IEEE MTT-S International Microwave Symposium (IMS)*, 2021.

[2] **Jing-Yu Lin**, S.W. Wong, Y. Yang, and L. Zhu, “Cavity balanced-to-unbalanced magic-T with filtering response,” *2019 IEEE MTT-S International Microwave Symposium (IMS)*,2019.

[3] **Jing-Yu Lin**, S.W. Wong, and L. Zhu, “High-Isolation Diplexer on Triple-Mode Cavity Filters,” *2017 IEEE MTT-S International Microwave Symposium (IMS)*, 2017.

[4] **Jing-Yu Lin** and Y. Yang, "3D Sub-Terahertz Dual-Mode Cavity Resonator and Its Application to Dual-Polarized Frequency Selective Surface," 2021 IEEE Asia-Pacific Microwave Conference (APMC), 2021, pp. 494-496.

[5] **Jing-Yu Lin**, S.-W. Wong and Y. Yang, "Filtering In-Band Full-Duplex Slot Antenna Based on TM120 and TM210 Dual-Mode Resonators," 2021 IEEE MTT-S International Microwave Filter Workshop (IMFW), 2021, pp. 249-251.

[6] **Jing-Yu Lin**, M. Li, S.-W. Wong, Y. Yang, and X. Zhu, "A cavity triple-mode filter with excitation of L-shape model," Microwave Symposium (AMS), 2018 Australian.

Under review:

[3] **J.-Y. Lin**, Y. Yang, T. Zhang, S.-W. Wong, and J. Du, "Inline Waveguide Bandpass Filter Using Bandstop Resonator Pairs," submitted to ***2023 IEEE MTT-S International Microwave Symposium (IMS)***.